DISSERTATION

GLYME-SYNTHESIZED NANOMATERIALS

Submitted by

James Armstrong

Department of Chemistry

In partial fulfillment of the requirements

For the Degree of Doctor of Philosophy

Colorado State University

Fort Collins, Colorado

Spring 2021

Doctoral Committee:

Advisor: Christopher J. Ackerson

Alan Kennan
Amy Prieto
Randall Basaraba

ABSTRACT

GLYME-SYNTHESIZED NANOMATERIALS

Nanomaterials include materials with at least one dimension in the nanometer range. These materials include nanoparticles, quantum dots, thin films, self-assembled materials, supramolecular materials and more. Nanoscience is an intriguing field for cutting edge research for energy, biology, medicine, optical and other applications. Coinage-metal (Au, Ag, Cu) nanomaterials are particularly of interest for the stability of nanoparticles synthesized with these metals. These metals can also be utilized to produce supramolecular assemblies, e.g. Hydrogels. In particular, this dissertation will cover four projects involving coinage metal nanomaterials. Chapter 2 discusses the ligand-exchange of a gold-thiolate nanocluster synthesized in diglyme, while chapters 3-5 investigate a unique supramolecular assembly of coinage-metal thiolates using glymes as antisolvent. Chapter 3 explores the underlying makeup of these amorphous assemblies, while chapters 4 and 5 investigate the application of this supramolecular assembly for additive manufacturing applications and antimicrobial applications, respectively. All of these products are linked through the synthesis and characterization of nanomaterials, which require the use of glymes (1,2-dme, diglyme, triglyme, etc) as a necessary synthetic solvent or antisolvent.

Nanoclusters are small, atomically precise nanoparticles with a metal core and a passivating layer of organic ligands. Coinage metal nanoclusters are studied for their stability, especially gold nanoclusters, allowing for long-term studies of properties and applications, as well as post-synthetic modifications. Precise control over ligand shell composition, particularly of mixed ligand layers is desired for control over nanocluster functionality.

Supramolecular materials build bulk properties through noncovalent interactions. Self-assembled supramolecular materials utilize small molecules which assemble into larger secondary and tertiary structures. These materials are of interest for a broad range of applications like additive manufacturing and biological applications.

The motivation behind this work was to explore nanomaterials which results from a glyme based synthesis. Gold nanocluster synthesis in diglyme is found to produce a stable gold-thiolate nanocluster with a single glyme ligand. The precision of a single-unique ligand could lead to further enhancements in nanocluster functionality in the future. Addition of glyme to a coinage-metal thiolate solution results in the rapid precipitation of a rigid supramolecular assembly. The resultant metallogel exhibits properties unique from similar materials without the use of glyme in synthesis. The metallogel is composed of oligomers reminiscent of nanoparticle precursors; as such, metallogel-nanoparticle composites are readily synthesized.

TABLE OF CONTENTS

ABSTRACT ii
CHAPTER 1: AN INTRODUCTION TO THIOLATE-PROTECTED GOLD NANOCLUSTERS AND SUPRAMOLECULAR MATERIALS 1
1.1 Gold Nanoclusters 1
1.2 Supramolecular Metallogels 8
REFERENCES 13
CHAPTER 2: THE $Au_{25}PMBA_{17}$DIGLYME NANOCLUSTER 23
2.1 Synopsis 23
2.2 Introduction 23
2.3 Results and Discussion 24
2.4 Conclusions 31
2.5 Experimental 31
REFERENCES 33
CHAPTER 3: RIGID METALLOGELS THROUGH DISRUPTED SELF-ASSEMBLY 36
3.1 Synopsis 36
3.2 Introduction 37
3.3 Results and Discussion 38
3.4 Conclusion 58
3.5 Methods and materials 59
REFERENCES 65
CHAPTER 4: MATERIAL PROPERTY ANALYSIS OF COINAGE-METAL THIOLATE ASSEMBLIES FOR FUTURE APPLICATIONS IN DIRECT-INK WRITING 68
4.1 Synopsis 68
4.2 Introduction 69
4.3 Results and Discussion 72
4.4 Conclusions 80
4.5 Experimental 81
REFERENCES 84
CHAPTER 5: INVESTIGATION OF THE ANTIMICROBIAL PROPERTIES OF A NOVEL SILVER METALLOGEL 87

5.1 Synopsis 87
5.2 Introduction 87
5.3 Results and Discussion 90
5.4 Conclusion 97
5.5 Experimental 97
REFERENCES 100
APPENDIX A: SUPPLEMENTAL FIGURES 102

CHAPTER 1: AN INTRODUCTION TO THIOLATE-PROTECTED GOLD NANOCLUSTERS AND SUPRAMOLECULAR MATERIALS

1.1 Gold Nanoclusters

Metal nanoparticles are of interest for their optical, electronic, and imaging properties.[1–3] Metal nanoparticle properties depend on the metal, ligand, size and shape.[4–6] Gold nanoparticles are of specific interest due to their stability.[7] The stability of gold nanoparticles is thought to be due to aurophilic bonding.[8]

Nanoparticles are typically created in the 10-100nm size range and are defined by their relative size and shape. Gold nanoclusters are small, atomically precise nanoparticles.[9] For example, $Au_{25}pMBA_{18}$ is a gold nanocluster with 25 gold atoms and 18 pMBA ligands. This exact size nanocluster can be made readily and repeatedly. This differs from larger nanoparticles, where the exact atomic structure of the particles is unknown, rather being characterized by size.

The first reported bottom-up synthesis of thiol-protected gold nanoparticles was the Brust-Schiffrin method, in 1994.[10] The Brust-Schiffrin method uses sodium borohydride to reduce gold salts in the presence of thiols to make gold nanoparticles. This marked the beginning of gold nanoclusters (AuNC) research. Gold nanoclusters are small gold nanoparticles, <2nm in diameter which exhibit properties different from those of larger nanoparticles, such as a HOMO-LUMO gap, discrete orbitals, and an exact atom count.[11,12] Due to the strong nature of gold-thiol bonds, thiolates are typically used as passivating ligands for AuNCs.[13] Control over the thiolate ligand layer is of interest to import functionality to gold nanoclusters for potential applications.[14,15]

Today, thiolate gold nanocluster syntheses resemble modified versions of the Brust-Schiffrin method. Thiolate gold nanocluster synthesis is typically done in two steps, polymerization and reduction, presented below in Figure 1.1.

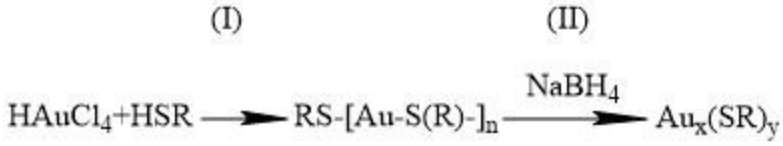

Figure 1.1: Reaction scheme for synthesis of a typical thiolate gold nanoclusters (I) Reduction of Au(III) salt by thiol results in formation of $Au_x(SR)_y$ polymerization. (II) Further reduction by addition of sodium borohydride results in formation of thiolate gold nanoclusters.

Reduction of Au(III) salt to Au(I) by thiols gives rise to the formation of -SR-[Au(I)-SR-]$_X$ polymers. Addition of sodium borohydride further reduces Au(I) to Au(0), which nucleate to form a core, which becomes passivated by residual polymeric precursors. Synthesis and characterization of a large number of gold nanoclusters has been reported, with a series of highly-stable nanoclusters ($Au_{25}(SR)_{18}$, $Au_{38}(SR)_{24}$, $Au_{102}(SR)_{44}$,…) standing out.[8,9,16] This series of stable nanocluster has been referred to as the "magic number" series.

The stability of "magic number" nanoclusters is well supported by superatom theory.[11,17–19] Superatom theory was originally used to describe the stability of small ligand-free metal clusters in the gas phase.[20] Superatom theory has since been used to well describe the increased stability of solution-phase gold nanoclusters. With electrons delocalized across the gold nanocluster, superatom theory assumes a spherically symmetrical square well potential, giving rise to a different ordering of orbitals than orbital theory, called superatomic orbitals (1S, 1P, 1D, 2S, 1F). The filling of these orbitals supports the stability of the "magic number" series analogous to

valence shell filling in atoms and molecules. The calculation for valence electron count for the filling of superatomic orbitals is $n^* = Nv_A - M - z$.

Where n^* is the total valence electron count, Nv_A is number of Au atoms multiplied by the number of valence electrons (the $6s^1$ electron for Au), M is the number of electron-withdrawing ligands, and z is the overall cluster charge. For example $Au_{25}(SR)_{18}^-$ is well known as a stable "magic number" nanocluster.[4] This cluster will have Nv_A=25, from the 25 gold atoms each donating the $6s^1$ electron, M=18, from the eighteen thiolate ligands, and z=-1, from the overall nanocluster charge. Using this equation, we can see the cluster will have 8 valence electrons, resulting in filling of the 1P orbital.

The first crystal structure of an AuNC was not solved until 2007, with the determination of Au_{102}[para-mercaptobenzoic acid(pMBA)]$_{44}$ structure through single-crystal x-ray diffraction.[9] Before this, gold nanocluster structure was hypothesized to consist of a metal core passivated by a monolayer of thiolate ligands.[21] The crystal structure of $Au_{102}(pMBA)_{44}$ exhibited a core of Au(0) atoms, protected by a ligand layer consisting of 19 RS-Au(I)-SR and 2 RS-(Au(I)-SR)$_2$ polymers, referred to as "staple motifs". Further crystal structures have shown the staple motif to be the primary ligand type protecting gold nanoclusters. For example, Figure 1.2 shows the structure of a $Au_{25}(SR)_{18}$ nanocluster, which has 6 RS-(Au(I)-SR)$_2$ staple motifs, protecting an icosahedral core of 13 Au(0) atoms.

Computational studies have shown staple motifs lead to a higher stability than monolayers of ligands.[23,24] This could be due to maximizing surface coverage of the ligand layer while maximizing the number of gold atoms in the metallic core, where interatomic distances are

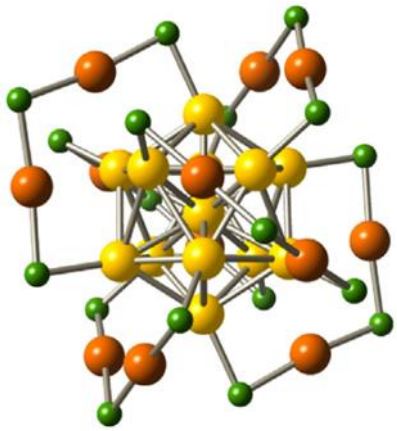

Figure 1.2: Structure of $Au_{25}(SR)_{18}$ where core Au(0) atoms are yellow, Au(I) atoms orange, and sulfur green, and -R groups omitted for clarity. The yellow core Au(0) atoms form an icosahedron around one central Au(0) atom, passivated by 6 RS-(Au(I)-SR)$_2$ staple motifs.[22]

indicative of aurophilic bonding, a key reason for the stability of gold nanoparticles and bulk gold. The structure of a gold nanocluster can now be explained as a core-shell structure, where a core is of metallic Au(0) atoms exhibiting metal-metal bonds is protected by a shell a shell of staple motif ligands.

Both the metal core, and the layer of staple motifs play a role in gold nanocluster properties. The metal core is responsible for the HOMO-LUMO gap.[25–27] The ligand layer is responsible for solubility, fluorescence, as well as importing functionality through functional groups on the ligands.[6,23,28] Synthesis is concerned with control over ligands. Control over the ligand layer will allow for control of the functionality and reactivity of gold nanoclusters. One aim of current research is to import multiple functionalities through having different ligands on the surface of a gold nanocluster.[29,30] Exact synthetic control over a mixed ligand layer gold nanocluster has not been reported.

One area of interest in the field is precise control over ligand layer composition. While synthesis of AuNCs with a single ligand is well studied, precise control over mixed ligand layers is currently prohibitive. Bound ligands can be exchanged for other thiolate ligands through a process called ligand exchange. In a typical ligand exchange reaction, an incoming thiol ligand will exchange any number of thiolate ligands on the AuNC, through an SN_2-like associative mechanism.[15,17,31] This creates a distribution of products with a mixed ligand layer. Figure 1.3 below highlights this issue with the distribution of ligand exchange products when (4-tert-butylphenyl)methanethiol is added to $Au_{24}Pd(SC_{12}H_{25})_{18}$.

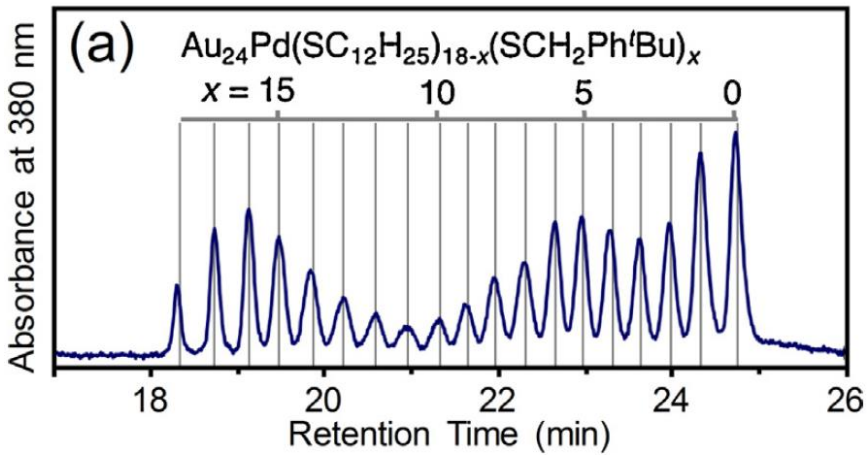

Figure 1.3: Chromatogram of a ligand exchange reaction showing the distribution of $Au_{24}Pd(SC_{12}H_{25})_{18-x}(SCH_2Ph^tBu)_x$ where (x=0-18). This highlights the current lack of control over ligand exchange reaction in gold nanocluster research.[32]

Using reverse phase high-performance liquid chromatography, Negishi et al. were able to separate the resultant gold nanoclusters based on the ligand layer conformation.[31] Although separation is possible, this exemplifies the current lack of precise control over mixed ligand layers in gold nanocluster synthesis. This produces low yields and has led to a lack of studies on mixed

ligand layers of exact conformations. Due the ligand layers effects on properties, precise control over mixed ligand layers are of interest for potential AuNC functionalization.

Gold nanoparticles are of interest for biological applications due to the biocompatibility of gold.[2,33,34] One drawback of using gold nanoparticles in vivo is the tendency for them to accumulate and aggregate in organs.[35,36] In contrast, gold nanoclusters are small enough where they can still function as biological imaging agents and be safely cleared from the body.[37] For these applications gold nanoclusters are attached to proteins, enzymes, or other biological agents.[38–40] Thiol groups on a biomolecule, such as cysteines, can be used to attach biomolecules to gold nanoclusters.[38,39] Analogous to thiolate ligand exchange mentioned above, one issue is controlling the number of biomolecules attached to a gold nanocluster, as a multitude of exchanges can occur. This leads to complications as the conjugate size can be too large to enter cells or behave natively. Current protocols involve a large excess of AuNCs so statistically only one attachment is expected. Multiple attachments can still occur. Current practices require further purification resulting in loss of AuNC products. Improving the route of biological attachment is of interest in the field, to lower potential research costs and expand the field.

Gold nanoclusters also show promising use as electrocatalysts and electron transfer agents.[27,41] For example, recently a platinum doped gold nanocluster $PtAu_{24}(SC_6H_{13})_{18}$ was reported to have higher catalytic activity for hydrogen production than other reported catalysts.[42] In this, and other studies, gold nanoclusters were shown to degrade, aggregate, or sinter over time when used as electrocatalysts. One method of improving the stability of AuNCs for electronic purposes is immobilization on surfaces.[27,42] Current practices anchor AuNCs to electrode surfaces utilizing electrostatic interactions through the ligands or incorporating a binding agent. To the best of our knowledge covalent attachment of thiolate-protected AuNCs has not been reported. This

should also increase stability as covalently bound AuNCs would be less likely to move or detach than current methods which could lead to longer life spans.

Previous research shows a diethylene glycol dimethyl ether (diglyme)-mediated Brust-Schiffrin method provides rapid synthesis of relatively monodisperse gold nanoclusters.[28] Further research showed diglyme-mediated synthesis exhibits dynamic dimerization of gold nanoclusters through a diglyme molecule, shown below in Figure 1.4[43]:

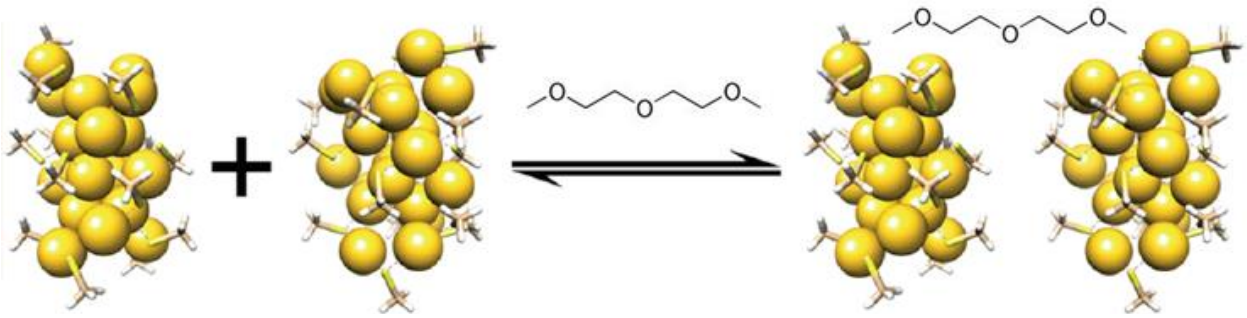

Figure 1.4: Dynamic dimerization of two Au_{20} nanoclusters with a diglyme linkage. The monomers and dimer exist in equilibrium, highlighting the weak Au-O bond between the gold nanoclusters and diglyme.[43]

The diglyme-Au bond linking the molecules was shown to be weak, with an equilibrium of monomeric and dimeric nanoclusters. Literature of larger, ~5nm, gold nanoparticles has shown diglyme to weakly passivate gold nanoparticles, and is readily exchanged with thiolate ligands for stability of nanoparticles.[44] From this it is hypothesized diglyme-for-thiolate exchange is preferable over thiolate-for-thiolate ligand exchange due to the weak gold-diglyme bond compared to the covalent gold-thiolate bond. My current research is aimed at producing a gold nanocluster product with a majority of thiolate ligands and a single diglyme ligand. Given the hypothesis of rapid diglyme-for-thiolate exchange, this could allow for control over single-ligand exchange on gold nanoclusters.

Presented here is the synthesis and characterization of a gold nanocluster consisting of 25 gold atoms with 17 thiolate ligands and one diglyme ligand. The diglyme should be readily available for exchange for thiolate ligands. This presents an opportunity to control monofunctionalization of the gold nanocluster with new thiolate ligands. This could lead to improving attachment of gold nanoclusters to biological agents for imaging. Future work will focus on attaching these clusters to surfaces using this feature, for interest in their electronic properties.

1.2 Supramolecular Metallogels

Gel materials have become common in everyday life in many forms.[45,46] These soft materials are personified by cosmetics such as hair gels, toothpaste, etc.[47] Polymeric based gels are used in current applications in medicine, materials science, and many other fields.[48] Contact lenses are typically made from polymeric gels.[49] Gels are a typically a type of soft materials known as supramolecular materials.

Supramolecular gels are an area of large recent interest.[50–54] Supramolecular assemblies are hierarchical structures wherein discrete molecular units assemble into a larger structure through noncovalent interactions.[51,55] Supramolecular materials include can include polymeric systems, low molecular weight gelators, and hydrogels, amongst other assemblies.[52–54] Supramolecular gels self-assemble through non-covalent interactions into bulk networks. These assemblies commonly form secondary structures such as sheets or fibers.[53] If these structures are large enough, physical entanglement can play a role in gelation. Typically, these gels will trap solvent molecules, making up the bulk of their weight. These soft materials are of interest for applications in biological systems, such as contacts or biological implants.

Gels can be classified by their components, medium, and the nature of their crosslinking. Organogels, hydrogels, and aerogels describe the media in which the material produces a gel network.[54] Long chain macromolecular gels, i.e. polymers, can gel through the physical interaction of fiber entanglement, or be gelled through chemical crosslinking.[54,54] Low molecular weight gelators are supramolecular assemblies wherein small molecules self-assemble material through noncovalent interactions e.g. hydrophobic interactions, hydrogen bonding, van der waals forces.[56–58] Metallogels are classified as supramolecular assemblies describing the components of the gels.[54,59,60] These supramolecular materials contain metal ions where the metal-ligand character plays a large role in the assembly process.

Self-assembly is the process by which precursor materials form bulk materials.[51] Precursor building blocks tend to be small molecules which utilize non-covalent interactions to repeatedly assemble and form larger structures. Intelligent design and choice of the underlying gelators can be utilized to tune not only the bulk properties, but the microstructure as well.[51,57,61] This process is known as hierarchical self-assembly, and is shown below in Figure 1.5.

Hierarchical self-assembly describes the assembly of bulk materials from multiple smaller structures. The base unit small molecules can create secondary structures by the formation of metal-ligand complexes, or non-covalent interactions can create a secondary assembly of these units. This secondary structure can then create larger shapes and structures through supramolecular assembly of these secondary structures with non-covalent interactions. This process can be repeated until bulk characteristics are exhibited. For example, hydrophobic groups can result in the folding of the secondary into micelles in an aqueous environment.[51,62] This graphic, Figure 1.5, visualizes the amount of control available when formulating supramolecular

assemblies. Functional group type, number, and orientation, as well as precursor size, can influence the structure and morphology of the resultant assembly.[51,57,63]

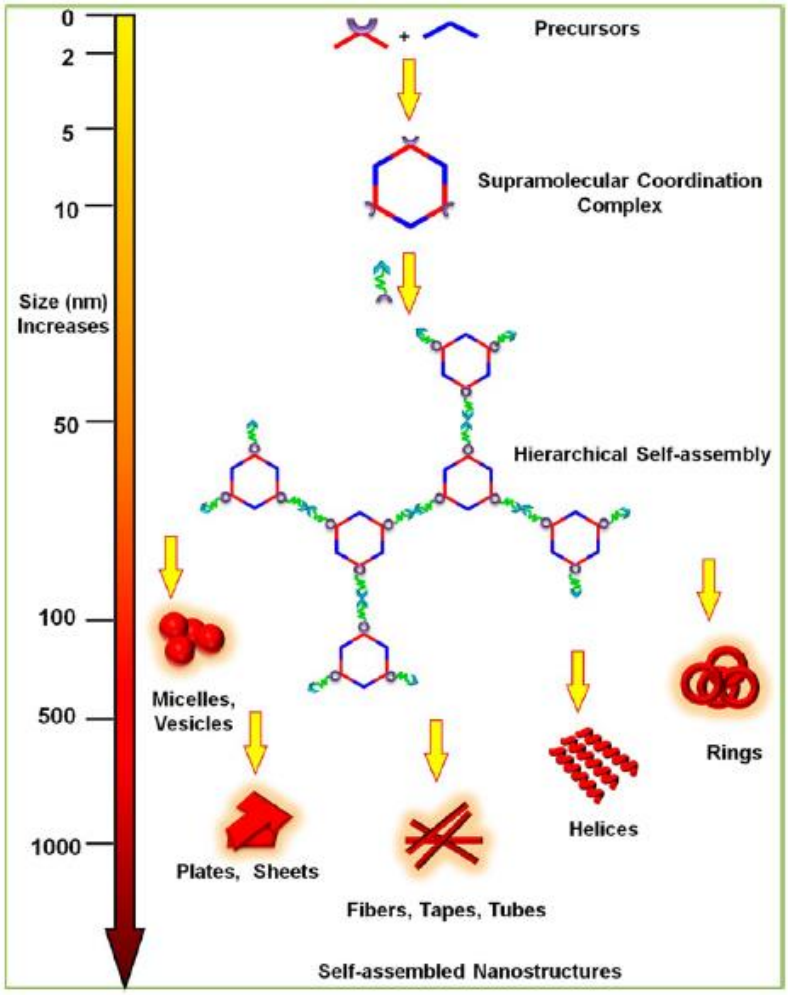

Figure 1.5: Hierarchical Self- Assembly of nanostructures.[51]

Metallogels present unique properties which are of growing interest.[50,60,64] The dynamic metal-ligand bond helps create the underlying building block for formation of metallogels. Metallogels will assemble similarly to other self-assembled supramolecular materials, but the

metal type and coordination can also play a role in the resultant structure and properties.[63] For example, changing the redox state of a metal ion can cause the material to undergo a sol-gel transition.[65] This allows for the creation of stimuli responsive materials, which are of interest for in sensing and drug delivery, as well as the formation of self-healing gels. The used of metal ions can also create conductive gel materials.[64,66]

Supramolecular gels assemble through the non-covalent interactions and have a large surface area for solvent accessibility. These dependencies allow for gels to make remarkable stimuli-responsive gels.[61,67] Stimuli responsive gels will undergo a transition when exposed to a specific condition. This can be exhibited by a rearrangement of the gel, or a change in properties such as color, fluorescence, conductivity, and more. Smart design of the underlying components of a supramolecular gel can allow to targeted measurement to specific stimuli.

As discussed in Chapter 1.1, the gold-sulfur bond is well studied for its strength, exemplified by the strength of thiolate ligands on gold nanoparticles.[13] Gold-thiolate coordinate oligomers are formed as a precursor in nanoparticle synthesis.[68,69] The stability of the gold-sulfur bond is used to coordination polymers to form gold-thiolate supramolecular systems.[70,71] These oligomers were shown to assemble into 2D sheets, with ligands perpendicular to the sheet.[72,73] With the correct thiol ligand, these sheets could stack through hydrogen bonding in aqueous solution, forming supramolecular hydrogels.[72,73] This process could be used to gelate some small-molecule drugs, presenting the potential application of drug delivery.[74] This idea was expanded upon with the use of dithiol polymers, which created a self-healing hydrogel.[75,76]

One issue with these coinage-metal thiolate assemblies, and largely supramolecular gels in general, is their mechanical strength.[77] These materials tend to be weak to mechanical forces, which limits the applications, or necessitates the use of additives to increase their strength.

Supramolecular gels are of interest for a broad range of applications. One application at the forefront of modern technology is additive manufacturing.[78] Additive manufacturing, or 3D printing, allows for the formation of highly customizable products with specific geometries, built layer by layer for specific properties and applications.[79] The dynamic nature of supramolecular materials makes them an advantageous material for future additive manufacturing purposes. This includes customizable cellular scaffolding and biomedical implants, as well as the printing of metallosupramolecular assemblies, which can be post-processed to form metallic parts.[78,80]

The dynamic nature of supramolecular assemblies has led to interest in numerous biomedical applications. For example, stimuli responsive materials can be utilized for the controlled release of drugs.[62,74] Silver-containing supramolecular materials have gained large recent interest due to silvers long history of as an antimicrobial.[81,82] The use of silver nanoparticles impregnated into hydrogels, or metallogels formulated with silver ions or nanoparticles have been studied for use against a variety of microbes and bacteria.[83,84] These materials have promising results against antibacterial-resistant bacteria.[85,86]

Presented in this dissertation is the study of a coinage-metal thiolate system with greatly increased mechanical strength in relation to comparable materials. The structure of these materials is investigated, as well as an initial look at future applications in additive manufacturing and antimicrobial materials.

REFERENCES

1. Qian, H. *et al.* Monoplatinum Doping of Gold Nanoclusters and Catalytic Application. *J. Am. Chem. Soc.* **134**, 16159–16162 (2012).

2. Zheng, Y., Lai, L., Liu, W., Jiang, H. & Wang, X. Recent advances in biomedical applications of fluorescent gold nanoclusters. *Adv. Colloid Interface Sci.* **242**, 1–16 (2017).

3. Ghosh, P., Han, G., De, M., Kim, C. & Rotello, V. Gold nanoparticles in delivery applications☆. *Adv. Drug Deliv. Rev.* **60**, 1307–1315 (2008).

4. Chithrani, B. D., Ghazani, A. A. & Chan, W. C. W. Determining the Size and Shape Dependence of Gold Nanoparticle Uptake into Mammalian Cells. *Nano Lett.* **6**, 662–668 (2006).

5. Plascencia-Villa, G. *et al.* Analytical Characterization of Size-Dependent Properties of Larger Aqueous Gold Nanoclusters. *J. Phys. Chem. C* **120**, 8950–8958 (2016).

6. Wu, Z. & Jin, R. On the Ligand's Role in the Fluorescence of Gold Nanoclusters. *Nano Lett.* **10**, 2568–2573 (2010).

7. Zhou, J., Ralston, J., Sedev, R. & Beattie, D. A. Functionalized gold nanoparticles: Synthesis, structure and colloid stability. *J. Colloid Interface Sci.* **331**, 251–262 (2009).

8. Heaven, M. W., Dass, A., White, P. S., Holt, K. M. & Murray, R. W. Crystal Structure of the Gold Nanoparticle [N(C_8H_{17})$_4$][Au_{25}(SCH_2CH_2Ph)$_{18}$]. *J. Am. Chem. Soc.* **130**, 3754–3755 (2008).

9. Jadzinsky, P. D., Calero, G., Ackerson, C. J., Bushnell, D. A. & Kornberg, R. D. Structure of a Thiol Monolayer-Protected Gold Nanoparticle at 1.1 A Resolution. *Science* **318**, 430–433 (2007).

10. Brust, M., Walker, M., Bethell, D., Schiffrin, D. J. & Whyman, R. Synthesis of thiol-derivatised gold nanoparticles in a two-phase Liquid–Liquid system. *J Chem Soc Chem Commun* **0**, 801–802 (1994).

11. Tofanelli, M. A. & Ackerson, C. J. Superatom Electron Configuration Predicts Thermal Stability of $Au_{25}(SR)_{18}$ Nanoclusters. *J. Am. Chem. Soc.* **134**, 16937–16940 (2012).

12. Gao, Y., Shao, N. & Zeng, X. C. *Ab Initio* Study of Thiolate-Protected Au_{102} Nanocluster. *ACS Nano* **2**, 1497–1503 (2008).

13. Häkkinen, H. The gold–sulfur interface at the nanoscale. *Nat. Chem.* **4**, 443–455 (2012).

14. Guo, R., Song, Y., Wang, G. & Murray, R. W. Does Core Size Matter in the Kinetics of Ligand Exchanges of Monolayer-Protected Au Clusters? *J. Am. Chem. Soc.* **127**, 2752–2757 (2005).

15. Heinecke, C. L. *et al.* Structural and Theoretical Basis for Ligand Exchange on Thiolate Monolayer Protected Gold Nanoclusters. *J. Am. Chem. Soc.* **134**, 13316–13322 (2012).

16. Qian, H., Eckenhoff, W. T., Zhu, Y., Pintauer, T. & Jin, R. Total Structure Determination of Thiolate-Protected Au_{38} Nanoparticles. *J. Am. Chem. Soc.* **132**, 8280–8281 (2010).

17. Ni, T. W., Tofanelli, M. A., Phillips, B. D. & Ackerson, C. J. Structural Basis for Ligand Exchange on $Au_{25}(SR)_{18}$. *Inorg. Chem.* **53**, 6500–6502 (2014).

18. Wang, Y. *et al.* An Intermetallic Au $_{24}$ Ag $_{20}$ Superatom Nanocluster Stabilized by Labile Ligands. *J. Am. Chem. Soc.* **137**, 4324–4327 (2015).

19. Tofanelli, M. A., Ni, T. W., Phillips, B. D. & Ackerson, C. J. Crystal Structure of the PdAu $_{24}$ (SR) $_{18}$ ^{0} Superatom. *Inorg. Chem.* **55**, 999–1001 (2016).

20. de Heer, W. A. The physics of simple metal clusters: self-consistent jellium model and semiclassical approaches. *Rev. Mod. Phys.* 611–676 (1993).

21. Templeton, A. C., Wuelfing, W. P. & Murray, R. W. Monolayer-Protected Cluster Molecules. *Acc. Chem. Res.* **33**, 27–36 (2000).

22. Kurashige, W., Niihori, Y., Sharma, S. & Negishi, Y. Recent Progress in the Functionalization Methods of Thiolate-Protected Gold Clusters. *J. Phys. Chem. Lett.* **5**, 4134–4142 (2014).

23. Jiang, D., Tiago, M. L., Luo, W. & Dai, S. The "Staple" Motif: A Key to Stability of Thiolate-Protected Gold Nanoclusters. *J. Am. Chem. Soc.* **130**, 2777–2779 (2008).

24. Hu, G., Jin, R. & Jiang, D. Beyond the staple motif: a new order at the thiolate–gold interface. *Nanoscale* **8**, 20103–20110 (2016).

25. Aikens, C. M. Electronic Structure of Ligand-Passivated Gold and Silver Nanoclusters. *J. Phys. Chem. Lett.* **2**, 99–104 (2011).

26. Deng, H. *et al.* Active metal (cadmium) doping enhanced the stability of inert metal (gold) nanocluster under O2 atmosphere and the catalysis activity of benzyl alcohol oxidation. *Gold Bull.* **48**, 161–167 (2015).

27. Kwak, K. & Lee, D. Electrochemistry of Atomically Precise Metal Nanoclusters. *Acc. Chem. Res.* **52**, 12–22 (2019).

28. Wong, O. A., Compel, W. S. & Ackerson, C. J. Combinatorial Discovery of Cosolvent Systems for Production of Narrow Dispersion Thiolate-Protected Gold Nanoparticles. *ACS Comb. Sci.* **17**, 11–18 (2015).

29. Truttmann, V. *et al.* Ligand engineering of immobilized nanoclusters on surfaces: ligand exchange reactions with supported $Au_{11}(PPh_3)_7Br_3$. *Nanoscale* **12**, 12809–12816 (2020).

30. Shibu, E. S., Muhammed, M. A. H., Tsukuda, T. & Pradeep, T. Ligand Exchange of $Au_{25}SG_{18}$ Leading to Functionalized Gold Clusters: Spectroscopy, Kinetics, and Luminescence. *J. Phys. Chem. C* **112**, 12168–12176 (2008).

31. Niihori, Y., Kikuchi, Y., Kato, A., Matsuzaki, M. & Negishi, Y. Understanding Ligand-Exchange Reactions on Thiolate-Protected Gold Clusters by Probing Isomer Distributions Using Reversed-Phase High-Performance Liquid Chromatography. **9**, 10 (2015).

32. Niihori, Y., Kikuchi, Y., Kato, A., Matsuzaki, M. & Negishi, Y. Understanding Ligand-Exchange Reactions on Thiolate-Protected Gold Clusters by Probing Isomer Distributions Using Reversed-Phase High-Performance Liquid Chromatography. *ACS Nano* **9**, 9347–9356 (2015).

33. Ackerson, C. J., Powell, R. D. & Hainfeld, J. F. Site-Specific Biomolecule Labeling with Gold Clusters. in *Methods in Enzymology* vol. 481 195–230 (Elsevier, 2010).

34. Safer, D., Hainfeld, J., Wall, J. & Reardon, J. Biospecific labeling with undecagold: visualization of the biotin-binding site on avidin. *Science* **218**, 290–291 (1982).

35. Lasagna-Reeves, C. *et al.* Bioaccumulation and toxicity of gold nanoparticles after repeated administration in mice. *Biochem. Biophys. Res. Commun.* **393**, 649–655 (2010).

36. Schleh, C. *et al.* Size and surface charge of gold nanoparticles determine absorption across intestinal barriers and accumulation in secondary target organs after oral administration. *Nanotoxicology* **6**, 36–46 (2012).

37. Loynachan, C. N. *et al.* Renal clearable catalytic gold nanoclusters for in vivo disease monitoring. *Nat. Nanotechnol.* **14**, 883–890 (2019).

38. Lin, C.-A. J. *et al.* Synthesis, Characterization, and Bioconjugation of Fluorescent Gold Nanoclusters toward Biological Labeling Applications. *ACS Nano* **3**, 395–401 (2009).

39. Chevrier, D. M. Properties and applications of protein-stabilized fluorescent gold nanoclusters: short review. *J. Nanophotonics* **6**, 064504 (2012).

40. Zhang, L. & Wang, E. Metal nanoclusters: New fluorescent probes for sensors and bioimaging. *Nano Today* **9**, 132–157 (2014).

41. Sardar, R., Funston, A. M., Mulvaney, P. & Murray, R. W. Gold Nanoparticles: Past, Present, and Future †. *Langmuir* **25**, 13840–13851 (2009).

42. Kwak, K. *et al.* A molecule-like PtAu24(SC6H13)18 nanocluster as an electrocatalyst for hydrogen production. *Nat. Commun.* **8**, 14723 (2017).

43. Compel, W. S. *et al.* Dynamic Diglyme-Mediated Self-Assembly of Gold Nanoclusters. *ACS Nano* **9**, 11690–11698 (2015).

44. Schulz-Dobrick, M., Sarathy, K. V. & Jansen, M. Surfactant-Free Synthesis and Functionalization of Gold Nanoparticles. *J. Am. Chem. Soc.* **127**, 12816–12817 (2005).

45. Babu, S. S., Praveen, V. K. & Ajayaghosh, A. Functional π-Gelators and Their Applications. *Chem. Rev.* **114**, 1973–2129 (2014).

46. Burey, P., Bhandari, B. R., Howes, T. & Gidley, M. J. Hydrocolloid Gel Particles: Formation, Characterization, and Application. *Crit. Rev. Food Sci. Nutr.* **48**, 361–377 (2008).

47. Douglas, J. Weak and Strong Gels and the Emergence of the Amorphous Solid State. *Gels* **4**, 19 (2018).

48. Ahmed, E. M. Hydrogel: Preparation, characterization, and applications: A review. *J. Adv. Res.* **6**, 105–121 (2015).

49. Musgrave, C. S. A. & Fang, F. Contact Lens Materials: A Materials Science Perspective. *Materials* **12**, 261 (2019).

50. Bentz, K. C. & Cohen, S. M. Supramolecular Metallopolymers: From Linear Materials to Infinite Networks. *Angew. Chem. Int. Ed.* **57**, 14992–15001 (2018).

51. Datta, S., Saha, M. L. & Stang, P. J. Hierarchical Assemblies of Supramolecular Coordination Complexes. *Acc. Chem. Res.* **51**, 2047–2063 (2018).

52. Dawn, A. & Kumari, H. Low Molecular Weight Supramolecular Gels Under Shear: Rheology as the Tool for Elucidating Structure-Function Correlation. *Chem. - Eur. J.* **24**, 762–776 (2018).

53. Liu, M., Ouyang, G., Niu, D. & Sang, Y. Supramolecular gelatons: towards the design of molecular gels. *Org. Chem. Front.* **5**, 2885–2900 (2018).

54. M. Sangeetha, N. & Maitra, U. Supramolecular gels: Functions and uses. *Chem. Soc. Rev.* **34**, 821–836 (2005).

55. Luo, B. *et al.* Hierarchical self-assembly of 3D lattices from polydisperse anisometric colloids. *Nat. Commun.* **10**, 1815 (2019).

56. Draper, E. R. & Adams, D. J. Low-Molecular-Weight Gels: The State of the Art. *Chem* **3**, 390–410 (2017).

57. Sahoo, P., Kumar, D. K., Raghavan, S. R. & Dastidar, P. Supramolecular Synthons in Designing Low Molecular Mass Gelling Agents: L-Amino Acid Methyl Ester Cinnamate Salts and their Anti-Solvent-Induced Instant Gelation. *Chem. - Asian J.* **6**, 1038–1047 (2011).

58. Draper, E. R. & Adams, D. J. Controlling the Assembly and Properties of Low-Molecular-Weight Hydrogelators. *Langmuir* acs.langmuir.9b00716 (2019) doi:10.1021/acs.langmuir.9b00716.

59. Häring, M. & Díaz, D. D. Supramolecular metallogels with bulk self-healing properties prepared by in situ metal complexation. *Chem. Commun.* **52**, 13068–13081 (2016).

60. Lima, J. & Rodríguez, L. Supramolecular Gold Metallogelators: The Key Role of Metallophilic Interactions. *Inorganics* **3**, 1–18 (2014).

61. Chen, L.-J. & Yang, H.-B. Construction of Stimuli-Responsive Functional Materials via Hierarchical Self-Assembly Involving Coordination Interactions. *Acc. Chem. Res.* **51**, 2699–2710 (2018).

62. Cheng, C.-C. *et al.* Hydrogen-bonded supramolecular micelle-mediated drug delivery enhances the efficacy and safety of cancer chemotherapy. *Polym. Chem.* **11**, 2791–2798 (2020).

63. Davis, A. V., Yeh, R. M. & Raymond, K. N. Supramolecular assembly dynamics. *Proc. Natl. Acad. Sci.* **99**, 4793–4796 (2002).

64. Aiyappa, H. B., Saha, S., Wadge, P., Banerjee, R. & Kurungot, S. Fe(III) phytate metallogel as a prototype anhydrous, intermediate temperature proton conductor. *Chem. Sci.* **6**, 603–607 (2015).

65. Sarkar, S., Dutta, S., Chakrabarti, S., Bairi, P. & Pal, T. Redox-Switchable Copper(I) Metallogel: A Metal–Organic Material for Selective and Naked-Eye Sensing of Picric Acid. *ACS Appl. Mater. Interfaces* **6**, 6308–6316 (2014).

66. Zhou, Q. *et al.* Reversible Redox Switching of Concurrent Luminescence and Visual Color Change Based on Lanthanide Metallogel. *Langmuir* **35**, 15344–15351 (2019).

67. Weng, W., Beck, J. B., Jamieson, A. M. & Rowan, S. J. Understanding the Mechanism of Gelation and Stimuli-Responsive Nature of a Class of Metallo-Supramolecular Gels. *J. Am. Chem. Soc.* **128**, 11663–11672 (2006).

68. Zhu, L. *et al.* New Insight into Intermediate Precursors of Brust–Schiffrin Gold Nanoparticles Synthesis. *J. Phys. Chem. C* **117**, 11399–11404 (2013).

69. Barngrover, B. M. & Aikens, C. M. Electron and Hydride Addition to Gold(I) Thiolate Oligomers: Implications for Gold–Thiolate Nanoparticle Growth Mechanisms. *J. Phys. Chem. Lett.* **2**, 990–994 (2011).

70. Vaidya, S. *et al.* Transparent and luminescent glasses of gold thiolate coordination polymers. *Chem. Sci.* **11**, 6815–6823 (2020).

71. Antoine, R. Supramolecular Gold Chemistry: From Atomically Precise Thiolate-Protected Gold Nanoclusters to Gold-Thiolate Nanostructures. *Nanomaterials* **10**, 377 (2020).

72. Odriozola, I., Loinaz, I., Pomposo, J. A. & Grande, H. J. Gold–glutathione supramolecular hydrogels. *J. Mater. Chem.* **17**, 4843 (2007).

73. Odriozola, I., Ormategui, N., Loinaz, I., Pomposo, J. A. & Grande, H. J. Coinage Metal–Glutathione Thiolates as a New Class of Supramolecular Hydrogelators. *Macromol. Symp.* **266**, 96–100 (2008).

74. Casuso, P., Carrasco, P., Loinaz, I., Grande, H. J. & Odriozola, I. Converting drugs into gelators: supramolecular hydrogels from N-acetyl-l-cysteine and coinage-metal salts. *Org. Biomol. Chem.* **8**, 5455 (2010).

75. Casuso, P. *et al.* Aurophilically cross-linked "dynamic" hydrogels mimicking healthy synovial fluid properties. *Chem Commun* **50**, 15199–15201 (2014).

76. Casuso, P. *et al.* Injectable and Self-Healing Dynamic Hydrogels Based on Metal(I)-Thiolate/Disulfide Exchange as Biomaterials with Tunable Mechanical Properties. *Biomacromolecules* **16**, 3552–3561 (2015).

77. Chivers, P. R. A. & Smith, D. K. Shaping and structuring supramolecular gels. *Nat. Rev. Mater.* **4**, 463–478 (2019).

78. Pekkanen, A. M., Mondschein, R. J., Williams, C. B. & Long, T. E. 3D Printing Polymers with Supramolecular Functionality for Biological Applications. *Biomacromolecules* **18**, 2669–2687 (2017).

79. Wong, K. V. & Hernandez, A. A Review of Additive Manufacturing. *ISRN Mech. Eng.* **2012**, 1–10 (2012).

80. Direct Ink Writing of 3D Functional Materials - Lewis - 2006 - Advanced Functional Materials - Wiley Online Library. https://onlinelibrary.wiley.com/doi/abs/10.1002/adfm.200600434.

81. Barras, F., Aussel, L. & Ezraty, B. Silver and Antibiotic, New Facts to an Old Story. *Antibiotics* **7**, (2018).

82. Sim, W., Barnard, R., Blaskovich, M. A. T. & Ziora, Z. Antimicrobial Silver in Medicinal and Consumer Applications: A Patent Review of the Past Decade (2007–2017). *Antibiotics* **7**, 93 (2018).

83. Alvarado-Gomez, E. *et al.* Evaluation of anti-biofilm and cytotoxic effect of a gel formulation with Pluronic F-127 and silver nanoparticles as a potential treatment for skin wounds. *Mater. Sci. Eng. C* **92**, 621–630 (2018).

84. Boonkaew, B., Kempf, M., Kimble, R., Supaphol, P. & Cuttle, L. Antimicrobial efficacy of a novel silver hydrogel dressing compared to two common silver burn wound dressings: Acticoat™ and PolyMem Silver®. *Burns* **40**, 89–96 (2014).

85. Rai, M. K., Deshmukh, S. D., Ingle, A. P. & Gade, A. K. Silver nanoparticles: the powerful nanoweapon against multidrug-resistant bacteria: Activity of silver nanoparticles against MDR bacteria. *J. Appl. Microbiol.* **112**, 841–852 (2012).

86. Doudi, M., Naghsh, N. & Setorki, M. Comparison of the effects of silver nanoparticles on pathogenic bacteria resistant to beta-lactam antibiotics (ESBLs) as a prokaryote model and Wistar rats as a eukaryote model. *Med. Sci. Monit. Basic Res.* **19**, 103–110 (2013).

CHAPTER 2: THE $Au_{25}PMBA_{17}$DIGLYME NANOCLUSTER*

2.1 Synopsis

The following work explores the synthesis of gold nanoclusters with diglyme as a solvent. Nanoparticles are nanomaterials composed of a metal core passivated by an organic ligand layer, typically defined by their size. Gold nanoclusters are small, atomically precise nanoparticles. The work accomplished here utilize glyme as a solvent, to synthesize a unique nanocluster which includes diglyme as a ligand, presenting a ligand-type for these nanomaterials.

Herein, a modification of a $Au_{25}(pMBA)_{18}$ nanocluster that incorporates one diglyme ligand as a direct synthetic product is reported. Notably the expected statistical production of clusters containing other ligand stoichiometries is not observed. This $Au_{25}(pMBA)_{17}$ diglyme product is characterized by electrospray mass spectrometry (ESI-MS) and optical spectroscopy. Thiolate for thiolate ligand exchange proceeds on this cluster, whereas thiolate for diglyme ligand exchange does not.

2.2 Introduction

The ligation shell surrounding protected metal clusters determine properties of the cluster including solubility, capacitance, biocompatibility, reactivity toward ligand exchange and catalytic capability.[1–5] Ligand shells of thiolate protected gold clusters can be modified by ligand exchange reactions. When a mixed ligand shell is produced, the product is inexact, representing a statistical

* *The work presented herein is in preparation for submission to Molecules with James Armstrong and Chris J. Ackerson as coauthors. James Armstrong's contributions include experimental design, data analysis, and synthetic development.*

distribution of both ligands, summing to the total number of ligands.[6,7] Mixed ligand shells with such a statistical distribution of 2 or more ligand types can also be produced when multiple ligand types are used in cluster synthesis.[8]

A few approaches can produce monofunctional gold clusters. These are desirable for bio-labelling, to create bioconjugates of exclusively 1:1 cluster:biomolecule stoichiometry.[9,10] Production of monofunctional clusters and/or nanoparticles can proceed by either of two approaches. One is to purify monofunctional clusters from a statistical distribution which contains multi-functional clusters.[10] Alternatively, a solid phase approach can produce clusters or nanoparticles that are monofunctional.[11] Both approaches represent a substantial and labor-intensive endeavor compared to a typical one-pot direct synthesis of gold nanoclusters.

Previously, our group reported that the phenolethanethiol (PET) protected nanocluster $Au_{20}(PET)_{15}$ could be assembled into dimers linked by diglyme. The clusters must be synthesized in diglyme as a solvent to observe this behavior.[12] The $Au_{20}(PET)_{15}$(diglyme)$Au_{20}(PET)_{15}$ dimers are in a dynamic equilibrium with $Au_{20}(PET)_{15}$ protomers. The finding of glyme linked clusters is interpreted as glyme making direct and dative (weak) bonds to gold. The overall finding was surprising due to the high strength of the Au-S bond compared to the bonding strength of diglyme to gold.[13] The overall interpretation is that when diglyme is present as solvent (in high molar quantities), that it can compete with thiolates for bonding to the surface of gold clusters.

2.3 Results and Discussion

$Au_{25}(SR)_{18}$ is the benchmark thiolate protected gold nanocluster.[14] It is preferentially produced in gold cluster synthesis due to its high stability against thermal etching.[15] This has made it a

widely used molecule to establish aspects of gold nanocluster synthesis, ligand exchange, and applications; Many properties that are found initially for $Au_{25}(SR)_{18}$ are later shown to be common to thiolate protected gold clusters in general.[2,16,17]

In this work, we show a modification of p-mercaptobenzoic acid (pMBA) protected $Au_{25}(pMBA)_{18}$ with a diglyme ligand, resulting in a cluster formulated as $Au_{25}pMBA_{17}$diglyme. Spectroscopic and Mass spectrometric analysis establish the existence of this cluster. Ligand exchange with incoming a thiol ligand was attempted, under the hypothesis that the diglyme ligand would preferentially exchange. Unexpectedly, diglyme does not exchange with a thiol ligand in any exchange condition, whereas other thiolate ligands do exchange.

To synthesize the cluster, a 125mL Erlenmeyer flask was charged with 24mL of 100mM pMBA in 0.3M NaOH in water and a stir bar. Addition of 8mL 100mM $HAuCl_4$ in diglyme was added dropwise. This creates a clear, yellow solution which is stirred for 30 minutes. 0.500mL of 10mM sodium borohydride in diglyme is slowly drip added to the solution over 1 minute, resulting in a color change to a deep red color. This solution is collected and diluted from 8mL aliquots to 50mL with diglyme, 1 mL of ammonium acetate is added. The product is collected by centrifugation. This results in an aqueous biphasic system, with the reaction products concentrated in the bottom phase at approximately 2mL volume and black in color. The black, aqueous phase is then separated using polyacrylamide gel electrophoresis (PAGE.) This typically reveals 3 products (bands) (Figure S1), with the bottom band appearing as a deep red color. All products are thought to be nanocluster sized, however this manuscript focuses on the bottom (red) product because it could be characterized by ESI-MS, whereas the other products could not be characterized by ESI-MS, presumably due to harsh ionization conditions.

The red product is collected by excising the band from of the PAGE gel. The excised gel containing the product is powdered with a mortar and pestle and eluted from the gel by an overnight soak in 10mL of water. Gravity filtration through a 150mm filter separates the soluble product from the insoluble gel.

The purified product was analyzed by Electrospray ionization – mass spectrometry (ESI-MS). Triethylammonium counterions were added because they improve spectra in ESI-MS of gold nanoclusters.[18]

ESI-MS of the purified cluster is shown in Figure 1.1. There are three apparent groups of peaks. The distance between peaks each grouping allows inference of the species charge, allowing a total mass calculation. The three peak groupings correspond to three charge states (-3, -4, and-5) of a nanocluster of atomic mass 7655a.u. This mass corresponds well with a cluster formula of $Au_{25}pmba_{17}diglyme$.

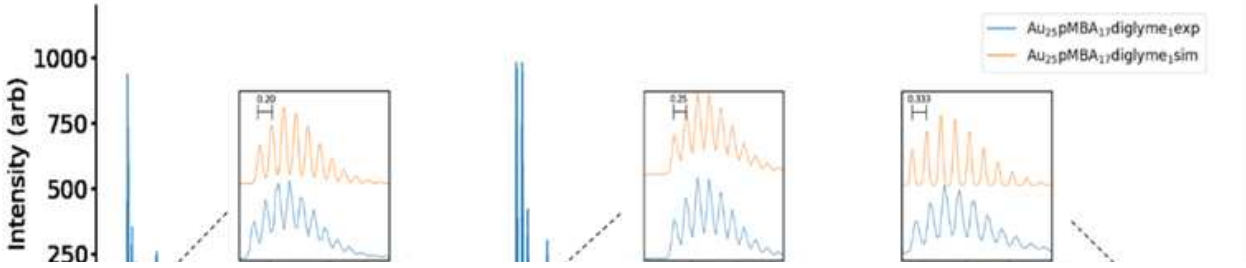

Figure 2.1: ESI-MS spectra Au25pMBA17diglyme, with 9 protonated carboxylic acid groups, and 8 deprotonated, shows 3 peak groupings. The peak spacing indicates charge states of -5, -4, and -3 respectively. All 3 parent peaks can be explained by a Au25pMBA17

That cluster has a mass of 7655a.u. when 8 of the ligands are deprotonated. Figure 2.1, inset, shows the simulated ESI mass spectrum for $Au_{25}pmba_{17}diglyme$ without 8 protons, comparing it to the experimental spectrum. The possibility of other combinations of Au and pMBA were also considered. Notably, we cannot assign this spectrum to the known $Au_x(SR)_y$ clusters of nearby formulae, including[18] $Au_{25}pMBA_{18}$ (mass 7682 a.u.), $Au_{23}pMBA_{16}$ (6981a.u) or $Au_{24}pMBA_{20}$ (7791a.u.). Table S1 tabulates the expected masses for each of these clusters and their possible protonation states. Some calculated nanocluster assignments are explored further in Table S1. Based on the mass spectrum of Figure 2.1, the product is assigned as $Au_{25}(pMBA)_{17}diglyme$.

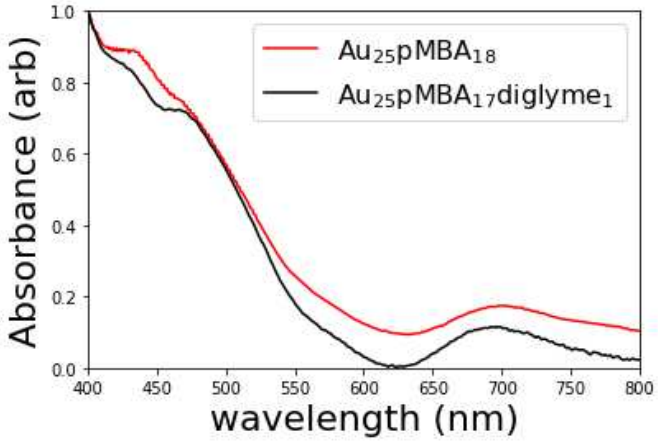

Figure 2.2: UV-VIS for Au25pMBA17diglyme1 (black) is comparable to the UV-VIS spectrum for Au25pMBA18(red), reproduced from Ref. 19)

Supporting this assignment is that the linear absorbance spectrum of $Au_{25}(pMBA)_{17}diglyme$ is similar, but not identical to the $Au_{25}(pMBA)_{18}$ spectrum (Figure 2.2). The $Au_{25}(pMBA)_{17}diglyme$ spectrum exhibits features at around 410, 440 and 680 nm. These features are similar to the $Au_{25}(SR)_{18}$ nanocluster,[19] which shows similar features around 430, 470 and 680nm. These linear absorption spectral features are attributed to the geometry of Au in a cluster.[20] This linear absorbance spectrum, therefore, suggests that the cluster consists of 25 gold atoms with 18 ligands in a similar geometric configuration to the very well-studied $Au_{25}(SR)_{18}$.

We considered that the differences in the linear optical spectrum could be explained as different oxidation states of $Au_{25}(SR)_{18}$ clusters. $Au_{25}(SR)_{18}$ clusters are known to be stable and isolable in +1 /0/-1 oxidation states. Generally, the oxidation state of a cluster can be determined most reliably by electrochemical means, such as a differential pulse voltammogram to establish the potentials at which the cluster (with a given ligand shell) is in each of the oxidation states. Then a resting potential measurement of a sample can establish the oxidation state of the clusters in the sample. For water-soluble gold clusters, however, electrochemical measurements cannot be made reliably.

Optical spectra of $Au_{25}SR_{18}$ nanoclusters are reported in +1, neutral and -1 oxidation states, and show distinguishing features. The linear absorption spectrum for $Au_{24}(pMBA)_{17}$diglyme appears most similar to known spectra of +1 oxidation state of $Au_{25}(SR)_{18}$ at the features around 430 and 470. However, the $Au_{24}(pMBA)_{17}$diglyme spectrum around 680nm more closely resembles the -1 oxidation state of $Au_{25}(SR)_{18}$.[15,21] Therefore, we cannot conclusively attribute the oxidation state based on the spectrum; The differences in the spectrum between the $Au_{25}(pMBA)_{18}$ (which can be assigned as oxidation state 0 based on the spectrum) and $Au_{25}(pMBA)_{17}$diglyme are likely due to the presence of diglyme in the ligand shell.

The finding of a synthesis that produces a monofunctional $Au_{25}pMBA_{17}$diglyme cluster prompted study of ligand exchange characteristics. Incoming ligand feeds of 3-mercaptopropionic (3-MPA) acid to pMBA were tested from a 1:1 ratio of incoming ligand:cluster, up to 10000:1 (Figures S2, S3). Solution pH was varied from 6 to 11; At pH values below 6 the clusters are insoluble. Temperatures from room temperature to 60°C were attempted. In all cases, ESI-MS spectra of the ligand exchange products revealed exchange of pMBA for 3-MPA, but no exchange of diglyme for 3-MPA.

Figure 2.3 shows the ESI-MS spectrum of a ligand exchange reaction executed with a 1000-fold excess of 3-MPA for 30 minutes at room temperature. This represents a typical result. In Figure 2.3, each peak can be attributed to the exchange of a pMBA ligand for a 3-MPA ligand, as annotated in the figure. In this reaction condition, we observe the exchange of up to 5 ligands, with 2 ligand-exchange appearing as the dominant product. There is no evidence of diglyme exchange.

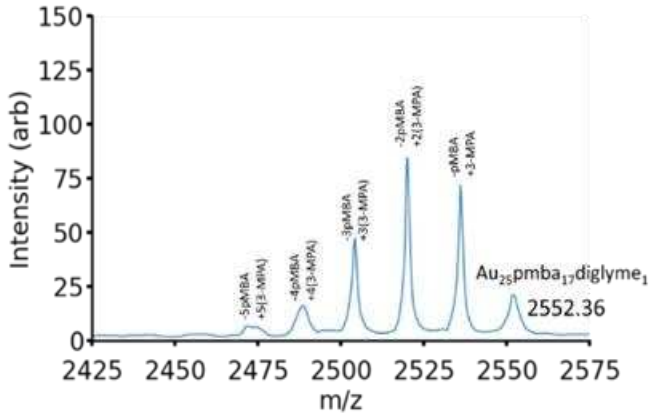

Figure 2.3: ESI-MS spectra of ligand exchange of Au25pMBA17diglyme1 with 3-mercaptopropionic acid. The furthest right peak can be attributed to the -5-charge state of Au25pMBA17diglyme1. Each subsequent peak to the left correlates to the exchange of a pMBA ligand for an incoming 3-MPA ligand.

Because the binding energy of thiolate ligands on gold is much more favorable than the binding energy of diglyme on gold[12], the absence of diglyme for thiol exchange is surprising. We can propose some mechanistic reasons for the absence diglyme exchange. For instance, most ligand exchange on gold clusters proceeds by an associative mechanism[22] which requires solvent exposed gold atoms[2]. It may be the case that diglyme ligands are bonded to gold atoms that have no solvent exposure, mechanistically blocking ligand exchange. Diglyme may also be bound in a

multidentate manner, whereas the thiolate ligands are monodentate; Multidentate binding of diglyme may interfere mechanistically with ligand exchange.

One ongoing interest is deciphering ligand regiochemistry[17] on gold nanoclusters. Regiochemical control of ligand location on gold nanoclusters is challenging because of the facile nature of inter-particle ligand exchange[7]. The inability of diglyme to exchange with thiolate ligands may represent a step toward improved regiochemical control of ligand locations on gold nanoparticles.

Interestingly, this system does not show any evidence for assembly into dimers or larger structures through the diglyme ligand. This was unexpected given our previous observations of $Au_{20}(PET)_{15}$ dimers linked through a diglyme molecule.[12] The present finding implies an enhanced role of pi-pi stacking between $Au_{20}(PET)_{15}$ nanoclusters playing a role in assembly, as was initially suggested by IR spectroscopy in our initial report.[12] The carboxylic acid group functional groups on pMBA could prevent this interaction occurring here through steric hindrance or the repulsion of similar surface charges between nanoclusters.

Overall, this project introduces promising aspects of glyme-synthesized materials. Shown here was the synthesis of atomically precise small nanoclusters where diglyme binds as a single ligand to the nanocluster. This synthesis is carried out in diglyme as a solvent to produce these nanoclusters. The unique aspect of utilizing diglyme is the controlled synthesis of a nanocluster with a single ligand which is unique from the remainder of the ligand son the nanocluster. Future chapters will discuss the use of glyme as antisolvent to produce supramolecular metallogels, however the reduction of these materials to create small, metal nanoparticles will be discussed in Chapter 4.

2.4 Conclusions

In conclusion, the highlights of this work include the synthesis of a cluster with a single diglyme ligand that does not participate in subsequent self-assembly. Because these clusters are water-soluble and singly functionalized, they may represent the beginnings of a more straightforward pathway for synthesizing the mono-functional clusters commonly used in bio-labeling.[23]

2.5 Experimental

Materials

Gold(III) chloride trihydrate ($HAuCl_4*3H_2O$, ACSreagent, >49.0% Au basis), sodium borohydride ($NaBH_4$, powder, >98.0%), ammonium acetate (NH_4OAc, ACSreagent, >97.0%), para-mercaptobenzoic acid (pMBA, >95.0%), 3-mercaoptopropionic acid (≥99%), (sodium hydroxide (NaOH, pellets, certified ACS) 2-Amino-2-(hydroxymethyl)-1,3-propanediol (Tris base, ≥ 99.9%), boric acid (H_3BO_3, ≥99.5%), glycerol ($C_3H_8O_3$, ≥99.5%), calcium chloride dehydrate ($CaCl_2*2H_2O$, crystalline), Ethylenediaminetetraacetic acid (EDTA, powder, >99.4%), and diethylene glycol dimethyl ether (diglyme, anhydrous, 99.5%) were obtained from Sigma-Aldrich.

Synthesis of $Au_{25}(pMBA)_{17}$diglyme

First, 8 mL of 100 mM $HAuCl_4*3H_2O$ in diglyme was added to 24 mL of 100 mM p-MBA in 0.3 M NaOH in a 250 mL Erlenmeyer flask. The reaction mixture was stirred for 30 minutes at 0°C in an ice bath. The reaction mixture underwent a color change from transparent red to transparent yellow indicating the reduction of gold in the formation of Au(I)-$[SR\text{-}Au(I)]_x$ chains. Addition of 10mM $NaBH_4$ in diglyme, by 100μL aliquots, 1 per minute for 5 minutes, caused a

color change to dark brown/black indicating the formation of nanoclusters. Dilution of 8 mL aliquots of reaction mixture to 50 mL was done with diglyme, followed by 1 mL addition of 5M ammonium acetate. Centrifugation caused separation into solid black, viscous black layer, and a colorless layer. The viscous layer is separated by TBE-PAGE, giving three products A, B, and C. Polyacrylamide gel electrophoresis (PAGE) is run using a buffer of 89 mM Tris base, 89 mM boric acid, and 2mM EDTA (TBE). PAGE is run using a VWR power source at a constant voltage of 125V for 3:00 hours. Samples are mixed 1:1by volume with 50/50 %b/v glycerol:water to assist loading into gel.

Ligand exchange of $Au_{25}pMBA_{17}$diglyme

An Erlenmeyer flask is charged with 0.1mM $Au_{25}pMBA_{17}$diglyme. Appropriate volume of 3-mercaptopropionic acid for the intended ratio of incoming ligand:cluster(1:1-10000:1) is added and allowed to stir at the appropriate temperature for 30 minutes. The reaction is quenched by dilution of 8 mL aliquots of reaction mixture to 50 mL was done with diglyme, followed by 1 mL addition of 5M ammonium acetate. Samples are collected by centrifugation and prepared for ESI-MS analysis.

Electrospray Ionization- Mass Spectrometry

Samples were prepared by dissolving clusters in 1 mL of 10mM triethylammonium buffer. These samples were precipitated in 50mL ethanol with 1 mL of 5M ammonium acetate, this was repeated 3 times. Mass Spectrometry-Electrospray Ionization (ESI-MS) was run using an Agilent Technologies G6220A instrument run in negative ionization mode. Source parameters include: Gas Temp 150 °C, Vaporizer 120, Gas Flow(l/min) 6.0, Nebulizer(psi) 18, and VCharge 2000. The scan rate was 1.34. Samples were run at a concentration of 0.01 mg/ml in water.

REFERENCES

1. Heinecke, C. L. *et al.* Structural and Theoretical Basis for Ligand Exchange on Thiolate Monolayer Protected Gold Nanoclusters. *J. Am. Chem. Soc.* **134**, 13316–13322 (2012).

2. Ni, T. W., Tofanelli, M. A., Phillips, B. D. & Ackerson, C. J. Structural Basis for Ligand Exchange on $Au_{25}(SR)_{18}$. *Inorg. Chem.* **53**, 6500–6502 (2014).

3. Zuber, G., Weiss, E. & Chiper, M. Biocompatible gold nanoclusters: synthetic strategies and biomedical prospects. *Nanotechnology* **30**, 352001 (2019).

4. Luo, Z., Zheng, K. & Xie, J. Engineering ultrasmall water-soluble gold and silver nanoclusters for biomedical applications. *Chem Commun* **50**, 5143–5155 (2014).

5. Nasaruddin, R. R., Chen, T., Yan, N. & Xie, J. Roles of thiolate ligands in the synthesis, properties and catalytic application of gold nanoclusters. *Coord. Chem. Rev.* **368**, 60–79 (2018).

6. Salassa, G., Sels, A., Mancin, F. & Bürgi, T. Dynamic Nature of Thiolate Monolayer in $Au_{25}(SR)_{18}$ Nanoclusters. *ACS Nano* **11**, 12609–12614 (2017).

7. Niihori, Y., Kikuchi, Y., Kato, A., Matsuzaki, M. & Negishi, Y. Understanding Ligand-Exchange Reactions on Thiolate-Protected Gold Clusters by Probing Isomer Distributions Using Reversed-Phase High-Performance Liquid Chromatography. **9**, 10 (2015).

8. Yuan, X. *et al.* Balancing the Rate of Cluster Growth and Etching for Gram-Scale Synthesis of Thiolate-Protected Au_{25} Nanoclusters with Atomic Precision. *Angew. Chem. Int. Ed.* **53**, 4623–4627 (2014).

9. Wang, H.-H. *et al.* Fluorescent Gold Nanoclusters as a Biocompatible Marker for *In Vitro* and *In Vivo* Tracking of Endothelial Cells. *ACS Nano* **5**, 4337–4344 (2011).

10. Safer, D., Hainfeld, J., Wall, J. & Reardon, J. Biospecific labeling with undecagold: visualization of the biotin-binding site on avidin. *Science* **218**, 290–291 (1982).

11. Worden, J. G., Dai, Q., Shaffer, A. W. & Huo, Q. Monofunctional Group-Modified Gold Nanoparticles from Solid Phase Synthesis Approach: Solid Support and Experimental Condition Effect. 10.

12. Compel, W. S. *et al.* Dynamic Diglyme-Mediated Self-Assembly of Gold Nanoclusters. *ACS Nano* **9**, 11690–11698 (2015).

13. Xue, Y., Li, X., Li, H. & Zhang, W. Quantifying thiol–gold interactions towards the efficient strength control. *Nat. Commun.* **5**, 4348 (2014).

14. Kang, X., Chong, H. & Zhu, M. $Au_{25}(SR)_{18}$: the captain of the great nanocluster ship. *Nanoscale* **10**, 10758–10834 (2018).

15. Tofanelli, M. A. & Ackerson, C. J. Superatom Electron Configuration Predicts Thermal Stability of $Au_{25}(SR)_{18}$ Nanoclusters. *J. Am. Chem. Soc.* **134**, 16937–16940 (2012).

16. Tracy, J. B. *et al.* Electrospray Ionization Mass Spectrometry of Uniform and Mixed Monolayer Nanoparticles: $Au_{25}[S(CH_2)_2Ph]_{18}$ and $Au_{25}[S(CH_2)_2Ph]_{18-x}(SR)_x$. *J. Am. Chem. Soc.* **129**, 16209–16215 (2007).

17. Hosier, C. A. & Ackerson, C. J. Regiochemistry of Thiolate for Selenolate Ligand Exchange on Gold Clusters. *J. Am. Chem. Soc.* **141**, 309–314 (2019).

18. Das, A. *et al.* Crystal structure and electronic properties of a thiolate-protected Au24 nanocluster. *Nanoscale* **6**, 6458 (2014).

19. Bertorelle, F. *et al.* Isomeric Effect of Mercaptobenzoic Acids on the Synthesis, Stability, and Optical Properties of $Au_{25}(MBA)_{18}$ Nanoclusters. *ACS Omega* **3**, 15635–15642 (2018).

20. Aikens, C. M. Electronic and Geometric Structure, Optical Properties, and Excited State Behavior in Atomically Precise Thiolate-Stabilized Noble Metal Nanoclusters. *Acc. Chem. Res.* **51**, 3065–3073 (2018).

21. Qian, H., Zhu, M., Wu, Z. & Jin, R. Quantum Sized Gold Nanoclusters with Atomic Precision. *Acc. Chem. Res.* **45**, 1470–1479 (2012).

22. Guo, R., Song, Y., Wang, G. & Murray, R. W. Does Core Size Matter in the Kinetics of Ligand Exchanges of Monolayer-Protected Au Clusters? *J. Am. Chem. Soc.* **127**, 2752–2757 (2005).

23. Ackerson, C. J., Powell, R. D. & Hainfeld, J. F. Site-Specific Biomolecule Labeling with Gold Clusters. in *Methods in Enzymology* vol. 481 195–230 (Elsevier, 2010).

CHAPTER 3: RIGID METALLOGELS THROUGH DISRUPTED SELF-ASSEMBLY*

3.1 Synopsis

The work herein investigates the underlying assembly of an amorphous coinage-metal thiolate supramolecular assembly synthesized using glyme as an antisolvent. This glyme-synthesized nanomaterial consists of silver-cysteine oligomers which assemble into amorphous colloids with a hydrodynamic radius of 42.6nm. These secondary structure colloids coalesce into a continuous network at low water content creating a surprisingly rigid material. These glyme-synthesized metallogels will be the focus for the remainder of this dissertation, this chapter and beyond. These supramolecular assemblies are synthesized from the same precursors as the nanoclusters discussed in Chapter 2, yet the addition of a large excess of glyme, and the lack of a reducing agent, yields a drastically different result.

Coinage metal-thiolate polymers exemplify hierarchical structure and structure-property relationships. They comprise structurally weak hydrogels of stacked sheets. Inclusion of an anti-solvent in synthesis of these polymers fundamentally changes their structure, resulting instead in colloidal amorphous metal complexes. The colloids undergo a hydration-dependent and reversible sol-gel transition. Because the colloids are flexible, they morph in the sol-gel transition to eliminate void spaces, producing a surprisingly rigid gel. Sodium ions that are aqueous in the sol transition to bridge colloids in the gel, rigidifying the system. The resulting mesh of colloids resembles a continuous network more similar to polymeric materials than colloidal gels. The

---

* *The work herein is in preparation for submission to Nature Materials with James Armstrong Patrick Shea, Cameron C. Cornell, Taylor Bryson, Harris E. Mason, Keith D. Morrison, Marcus Tofanelli, James P. Lewicki, Brandon C. Wood, Chris J. Ackerson and W. Scott Compel as coauthors. James Armstrong's contributions include synthetic development, data analysis, experimental design, including experiments in rheology, NMR, XRD, DLS, FT-IR and development of the schematic representation of the system.*

underlying structure results in a material that is strikingly disparate from compositionally similar materials. The distinct rheological properties that emerge that may render coinage metal-thiolate polymers as engineering-grade materials.

3.2 Introduction

The interactions among nanoscopic and microscopic component materials dictate the observed macroscopic behavior of their bulk assemblies.[1–6] For instance, fibers entangle to form gels, spheres agglomerate to form pastes, and sheets stack to form clays.[7–9] In each case, interparticle interactions control how the particles move past each other and shape the material's

mechanical response. Control over these behaviors afforded the existence of household synthetic items such as toothpaste, body lotion, and hair gel.

Incorporation of metals into soft materials weds the magnetic, optical, and catalytic properties of metals to the tunable mechanical behavior of soft materials.[10–12] The nano- and microstructures of these materials are defined at the nanoscale by the bonding geometries unique to metal-ligand chemistry.[1,4] Metallosupramolecular assemblies, coordination polymer networks, and metal-organic frameworks are all composed of cationic metal nodes bound to organic ligands to frame a molecular architecture.[10,13,14] Judicious selection of organic ligands in conjunction with a metal's preferred coordination environment enables rational design.[15,16]

Coinage metals (Au, Ag, Cu) are well-known to bind to thiols (HSR) to form metallopolymers with 1:1 M(I):SR stoichiometry.[2,17,18] These coinage metal-thiolate polymers (CMTPs) assemble laterally into crystalline sheets. These sheets stack in the third dimension, forming fibers that entangle and trap solvent to form "metallophilic" hydrogels (metallogels).[17,18]

Silver-cysteine (Ag-cys) hydrogels are highly desirable for their antibiotic properties, but they are structurally weak materials that often require adsorption onto other more rigid substrates.[1,19]

Here, we report a Ag-cys hydrogel with unprecedented hydration-state dependent rheological properties. The material undergoes a hydration-dependent and reversible sol-gel transition. The material's atypical rheological properties arise from a fundamentally different nanoscale structure than observed for previously described Ag-cys hydrogels. This anomalous Ag-cys metallogel is formed in the presence of the coordinating solvent 1,2-dimethoxyethane (glyme). Glyme hinders the self-assembly process that crystallizes the metallopolymers into sheets, but instead of producing an insoluble by-product the reaction phase-separates into a colloidal sol containing the precursors. The resulting material we call an amorphous metal complex (AMX), which yields an exceptionally rigid gel when dehydrated. This method of disrupting a hierarchical self-assembly process is unprecedented in the literature and may translate to supramolecular gels of all compositions, opening the door to many new structure-property relationships and soft-materials applications.

3.3 Results and Discussion

Glyme presence during Ag-cys metallopolymer synthesis induces phase-separation of the precursors into a dense sol. The sol phase thickens as it dries and exhibits rheological properties highly dependent on its moisture content. Sufficient dehydration triggers a sol-gel transition. The sol-gel transition is reversible; rehydration returns the gel to the sol phase. Sol-gel transitions are typically irreversible processes that permanently bind colloids to form a gel.[20] The sol-gel transition for the AMX, however, is completely reversible by dehydration and rehydration, shown in Figure 3.1.

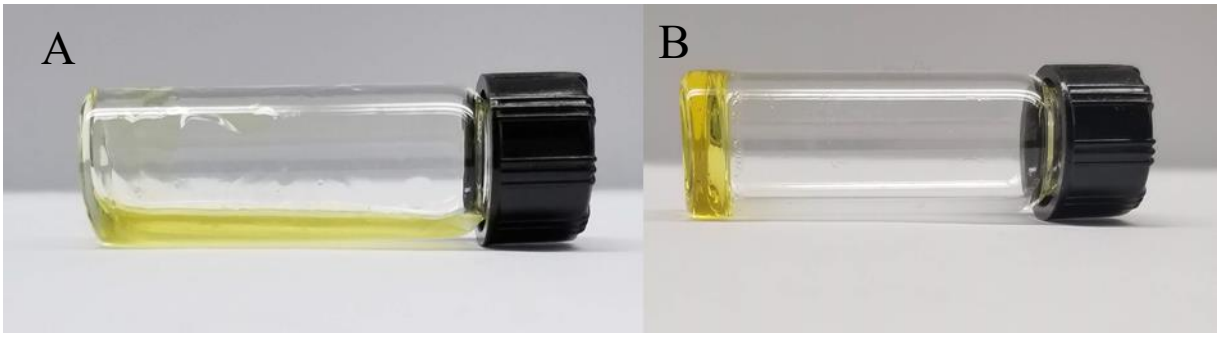

Figure 3.1: A silver- cysteine AMX in the A) solution phase and B) gel state.

At a high-water content, the AMX behaves as a sol, as exhibited by Figure 3.1A. As water is removed from the system, the AMX forms a gel material, shown in Figure 3.1B. Complete removal of water, as through lyophilization, interrupts the network formation, resulting in a powder.

Study of AMXs at various moisture content revealed the role of water in the sol-gel transition. Equilibration in relative humidity (RH) chambers containing saturated salt solutions provided consistent control over moisture content due to the hygroscopic nature of the material. Table S2 lists the equilibrium moisture content that arises in the metallogel at six RH environments. Oscillatory strain rheology performed on these samples pinpoints the moisture content that defines the gel point during the sol-gel transition (Figure 3.2).

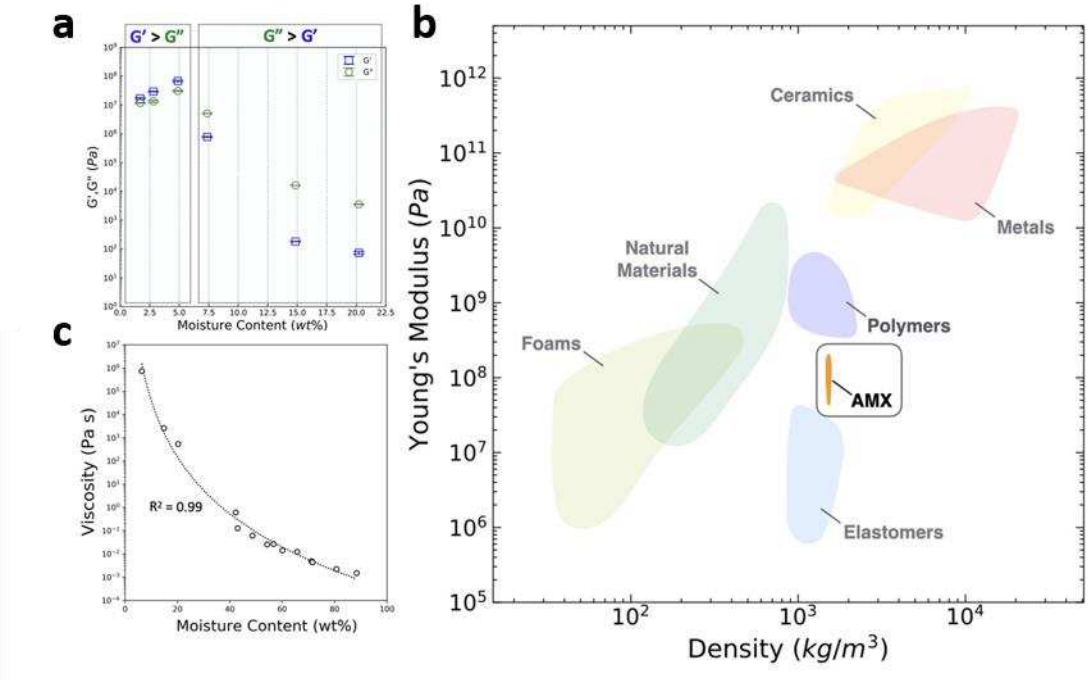

Figure 3.2: Physical properties of AMX. a) Comparison of G' (blue square) and G" (green circle) for different moisture contents. b) Ashby chart of Young's modulus vs. density of AMXs compared to engineering materials. c) Viscosity of AMX at various moisture contents.

Measuring the elastic (G') and viscous (G") moduli for each sample reveals the conditions at which the metallogel is a solid (G'>G") or a liquid (G">G'). Measurements were averaged across low strains to ensure the recorded moduli accurately represent an intact network. Figure 3.2A plots moduli for each sample as a function of moisture content. The data for samples at and below 4.9% moisture content exhibit solid gel character, while samples at and above 7.9% moisture content are liquid solution. This data indicates a sol-gel transition between 4.9% and 7.4% moisture content.

The data confirm the sol thickens as it dries by displaying an initial increase in moduli. Remarkably, this trend does not continue beyond the gel point. Once the material gels, further dehydration results in a drop of moduli, representing a surprising increase in flexibility. Thus, the data suggest a moisture content near the gel point where the gel is in its most rigid state. This

observation posits water in a structural role in gelation during the sol-gel transition, where dehydration past the gel point removes structural water and breaks down the network. Indeed, complete desiccation disintegrates the gel into a powder, demonstrating water's vital role in material integrity.

The material is solid under *ca.* 5% moisture content and exhibits G' ~ 10^7 Pa. Typical G' for coinage-metal thiolate hydrogels with similar composition are on the order of 10^1 Pa, while attempts to increase G' through incorporation into elastomeric networks plateaued at 10^3 Pa.[21] To better visualize the magnitude of this leap in rigidity it is best to convert G' to Young's modulus, a measure of uniaxial elastic deformation commonly reported for engineering materials (Equation S1). Figure 3.2B illustrates this range in a property chart of E' vs. density with comparison to common engineering materials.[22] The AMX materials surprisingly exhibit a modulus comparable to polymers and elastomers while in a gel-phase. The increase in modulus over traditional metallophilic hydrogels of nearly identical composition is clearly more than incremental. Such an advancement potentially renders metallogels as a whole available for use as engineering-grade materials.

Figure 3.2C depicts viscosity measurements of the sol over a broad range of moisture contents greater than the gel point. Viscosity initially drops rapidly with hydration then plateaus off with excessive dilution and approaches that of neat water. The continuous change in viscosity suggests water behaves as a classic solvent in the sol state, which contrasts with the clearly defined rheological domains manifested in organic polymers. Organic polymers move between highly concentrated entangled non-linear viscoelastic, semi-dilute, and dilute linear viscous Newtonian regimes. This difference indicates the metallogel does not interact with solvent in a manner similar to other polymeric materials, which suggests the metallopolymers that comprise AMXs are not

polymeric but oligomeric. Although though these trends are less clear in metal containing systems, the rheological response of the AMX resembles a colloidal system more a polymeric one than.

A previously unobserved molecular structure underlies these previously unobserved rheological properties. At the highest level of structural description, the material is amorphous. This is the conclusion of X-Ray diffraction measurements and Scanning Electron Microscopy (Figure 3.3). X-ray diffraction (XRD) analysis reveals a broad hump at 6º 2θ (1.47 nm) that potentially indicates the presence of long-range ordering (Figure 3.3A).

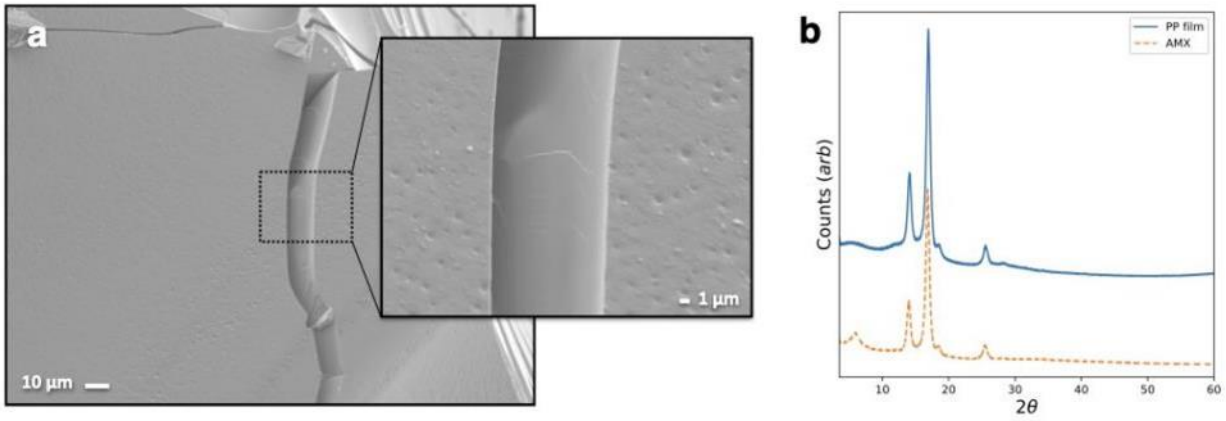

Figure 3.3: Structural investigation of AMX. a) SEM micrograph of dehydrated AMX showing lack of microstructure in material. Zoom inset of crack formed during dehydration shows sub-surface structure is uniform. b) XRD of AMX powder (orange dash trace) and the polypropylene film substrate (blue solid trace).

Otherwise, all other observed peaks arise from the polypropylene (PP) films the AMX material was deposited on. By comparison, XRD performed on Ag^0 nanocrystals generates a distinctive diffraction pattern with sharp peaks,[23] and CMTP hydrogels exhibit equally spaced peaks that arise as metallopolymer sheets assemble.[24] Lacking any of these features, XRD analysis

shows no crystallinity, revealing the AMX as amorphous. Electron microscopy provides structural insight into this amorphous material. Scanning electron microscopy (SEM) of the gel shows smooth, flat surfaces with cracks that formed as the gel dried (Figure 3.3B). There is no evidence of sub-surface structure within these cracks (Figure 3.3B, inset), implying the material is uniform. This is expected considering the amorphous nature of the material: the absence of building blocks precludes spontaneous assembly into secondary structures. In CMTP hydrogel systems, metallopolymers assemble into sheets that stack to form fibrils observable through SEM. The lack of structural similarity between these two materials of nearly identical composition is striking and indicates a fundamental change in molecular structure. Silver-cysteine hydrogels synthesized without glyme as an anti-solvent exhibit long-range order and microstructure (Figures S4, S5).

Ultimately, the AMX material is amorphous. This is vastly removed from compounds with a similar makeup, CMTP's. The addition of glyme as an antisolvent to the synthesis precipitates AMX's, creating the amorphous material as opposed to traditionally structured CMTP's. This change in structure happens alongside a drastic change in physical characteristics, exhibited by the rheological data seen in Figure 3.2. The change in structure is the most likely cause for this increase in rigidity. As such, determination of the underlying structure is of interest, and is the focus of the remainder of this work.

This material that appears amorphous in bulk measurements is comprised of colloids. Evidence for colloidal composition is implied by the reversible sol-gel transition described above. Gel permeation chromatography with multi-angle light scattering (GPC-MALS) also supports a colloidal composition. GPC-MALS (Figure S6) measurement of the sol phase determined the hydrodynamic radius (R_H) of colloids to be 41.4±0.3% nm and the radius of gyration (R_G) to be 277±0.3% nm. Dynamic light scattering (DLS) corroborates the ca. 40nm species (Figure 3.4).

Since R_H defines the radius of a hard sphere and R_G defines that of a mass-weighted average, the ratio between the two values provides insight into colloid structure. Observation of $R_G/R_H \sim 6.7$ in this system suggests the colloids are loosely packed, non-spherical agglomerates. For comparison, globular proteins or tightly bound polymer coils characteristically exhibit $R_G/R_H \leq 1$. In this case, the R_G radius of 277 nm is likely a more accurate interpretation of colloid size.

DLS data shows a bimodal distribution with radii of 1.42 ±0.08nm and 42.6 ±13.2nm. The first peak is thought to be due to dimers of cysteine or possibly cysteine-Ag-cysteine. The larger species represents larger assemblies is therefore the species of interest for investigation of the colloids. This could point to the oligomeric species folding similarly to classic long-chain polymers. Typically, a polymer would fold in an aqueous solution into a sphere to leave hydrophilic groups on the outside, with hydrophobic groups inside.

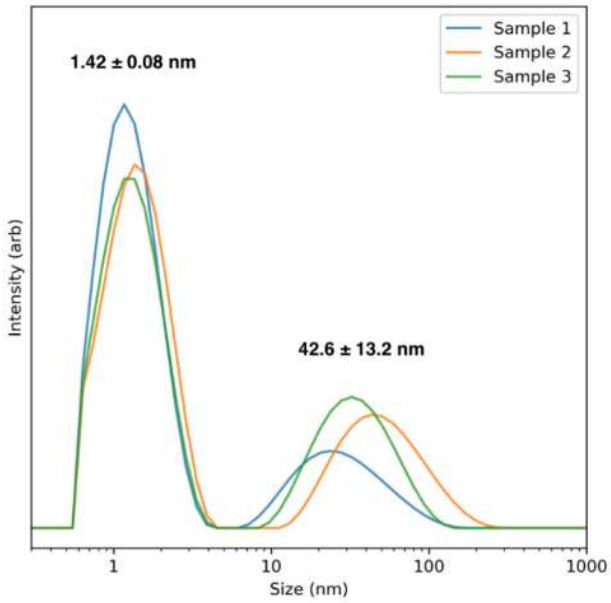

Figure 3.4: DLS data showing size of colloids in solution of hydrated AMX's.

This is typically not seen in a metal-thiolate system, as hydrogels are the notable product. This points to the addition of glyme as playing a major role in this process. Glymes inclusion as a solvent could cause a similar folding process to occur, as the AMX formation only occurs at a high enough concentration of glyme. It is interesting to note that once this colloid formation occurs, it is non-reversible, as the DLS is done in an aqueous environment with no glyme present. This data suggests there is a stable base unit building block to the assembly. A particle with same radius 42.6nm is seen repeatedly in different samples from different syntheses. If this structure was not a repeatedly formed unit, we would expect to see a large variety of sized materials with DLS. Instead, the stable colloids exist as secondary structures which assemble the metallogel. These colloids must be a secondary structure assembled from silver, cysteine, and potentially sodium. This secondary structure must then be assembling into some larger amorphous network at low water content to create the rigid structure exhibited in Figure 3.2.

The colloids are comprised of cysteine, silver, and sodium. Inductively coupled plasma mass-spectroscopy (ICP-MS) analysis of the AMX suggests molar ratios of 5:2:2 Ag:S:Na. A 2.5-fold excess of Ag over cysteine is unexpected and is unique among Ag-cys metallopolymer reports where CMTPs are well-known to exist in 1:1 M:SR stoichiometry.[18]

Carbon-13 nuclear magnetic resonance (^{13}C NMR) show that all three of cysteine's functional groups are bound to Ag^+ or Na^+ in some way (Figure 3.5, Table S3). The spectra show peak broadening for all three cysteine peaks. This broadening could be indicative of the ligands' functional groups being used in binding intra-colloidally, i.e. multiple functional groups of cysteine are involved in the production of these colloids. One interesting thing of note is the lack of peaks for carbon related to 1,2-dimethyoxyethane in the spectra. This is just further evidence

that while glyme plays a synthetic role in the production of AMXs, it does not play a structural role.

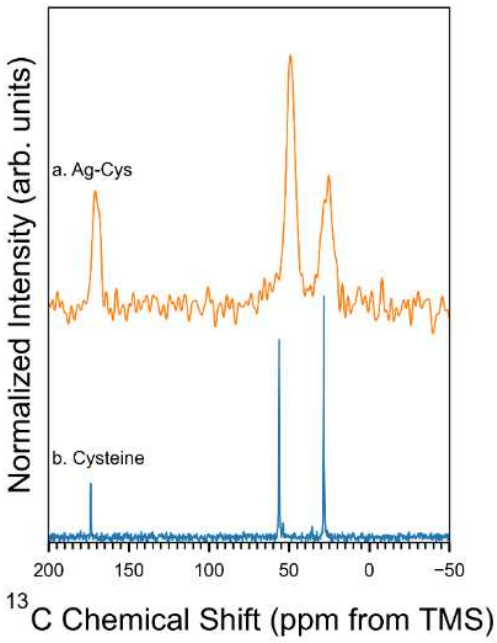

Figure 3.5: ^{13}C NMR showing a) AMX and b) cysteine. Functional group peaks broaden when cysteine is bound in the metallogel system.

Density functional theory (DFT) simulations of binding energies among AMX components were used to interpret the stoichiometric ratios of Ag and Na to cysteine in the context of promiscuous binding observed in ^{13}C NMR results. Bond dissociation energies (BDEs) were calculated for both Ag^+ and Na^+ cations with the thiol, carboxylic, and amine groups of cysteine, as well as for possible cysteine dimer configurations coordinated through these cations. The BDEs of the most stable conformers for Ag^+ and Na^+ coordination are given in Table S4 and depicted graphically in Figure 3.3. Ag^+ binding energies to cysteine functional groups are always larger than those for Na^+ and generally follow $S>NH_2>COO^-$.

` Of cysteine's three functional groups, Ag^+ binds least strongly to COO^-, while Na^+ binds most strongly to this group. Sodium present in the AMX is therefore expected to coordinate with

COO^- groups. The weaker nature of the Na-cysteine interactions compared to Ag-cysteine also suggests that these Na-cysteine bonds will be more readily broken up by water with increasing moisture content, while Ag-cysteine bonds will resist dissolution. BDE calculations collectively predict the molecular structure within the AMX colloids consists of short-chain -Ag-S- oligomers crosslinked through side-chain bonds to Ag^+; all Na^+ in the system is expected to coordinate to COO^-, shown in Figure 3.6.

Solid state ^{13}C NMR of pure cysteine displays three sharp peaks that correspond to the nearest carbon for each functional group of cysteine: CH_2-S, CH-NH_2, and COO. In comparison, the AMX displays very broad peaks shifted upfield from pure cysteine with no evidence of free cysteine in the system (Figure 3.5). The breadth of the peaks indicates that binding around cysteine is highly disordered and exists in a variety of conformations.

Formation of the metallogel herein requires the immediate addition of glyme at the onset of metallopolymer synthesis. Glyme quenches Ag-cys polymerization and precipitates the precursors into AMX colloids instead of assembling into thermodynamically favored structures. An in-depth discussion of glyme's role in AMX synthesis is out of the scope of this paper and will instead be described in a follow-up work. It is of note to point out glyme does not play a structural role in the resultant metallogel. This can be briefly seen in Figure 3.5, with the absence of peaks correlating to glyme carbons.

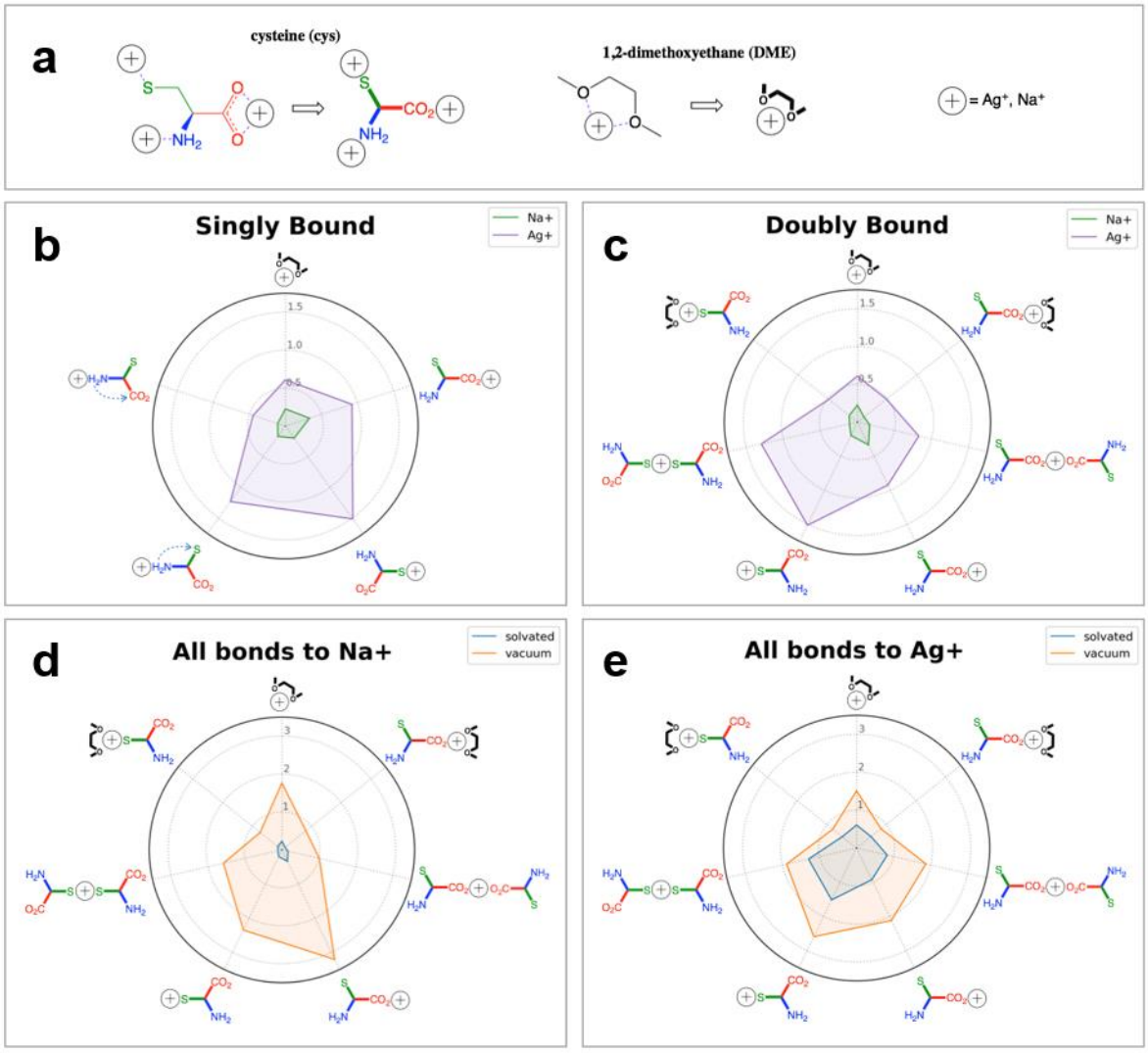

Figure 3.6: DFT calculations of bond dissociation energies (BDE). a) Cartoon legend of cysteine and 1,2-dimethoxyethane (DME) with Ag^+ and Na^+ ions shown in possible bonding configurations. b,c) Radar graphs depicting BDE (eV) of Na^+ and Ag^+ bound to functional groups of cysteine and DME for b) singly bound configurations and c) additional doubly bound configurations. d,f) Radar graphs depicting BDE (eV) of all bonds simulated in solvent and in vacuum for cysteine and DME bonds to d) Na^+ and e) Ag^+.

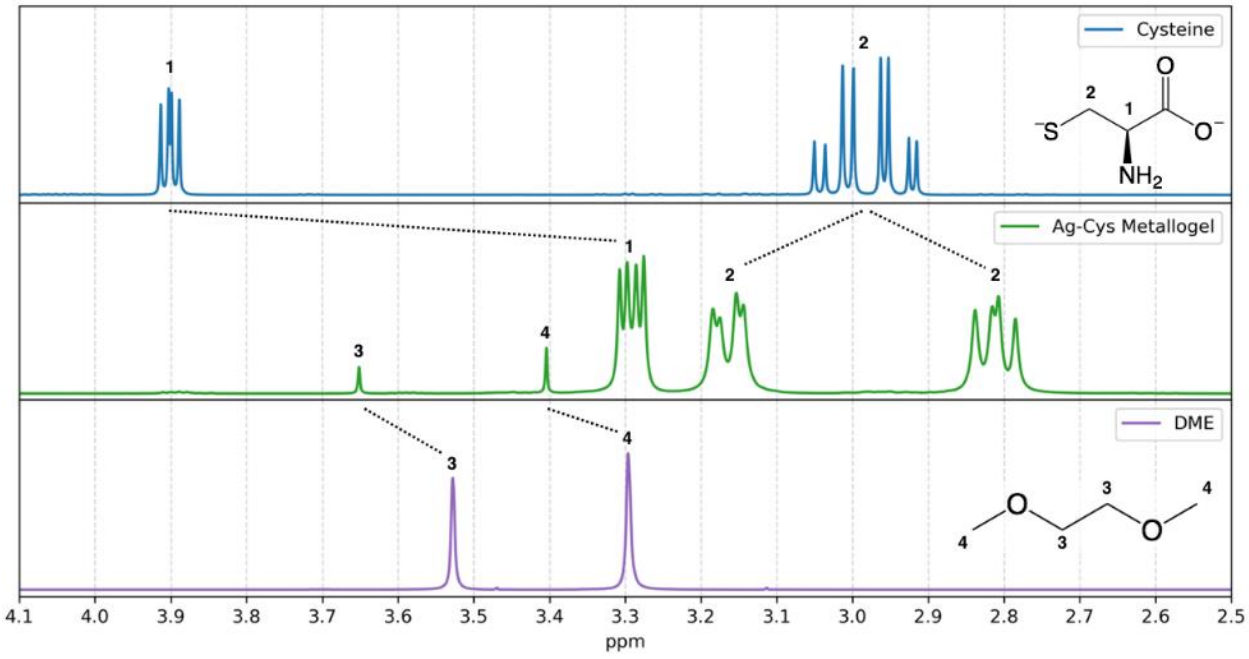

Figure 3.7: ^{1}H NMR of AMX's compared to neat cysteine and neat 1,2 dimethoxyethane.

^{1}H-NMR was run to examine the cysteine ligand. Shown here is ^{1}H-NMR data comparing neat cysteine, the metallogel, and 1,2-dimethoxyethane. Interestingly, one cysteine methylene peak grouping appears to be split into two peak groups in the metallogel. This is further investigated using HSQC and COSY. 1,2-dimethoxyethane appeared in the sample, shifted to higher ppm. This was due to incomplete purification of the metallogel product. Further investigation of 1,2-dimethoxyethane in synthesis was performed by comparing the peak shifts to 1,2-dimethoxyethane when mixed with both Ag^{+} and Na^{+} in solution.

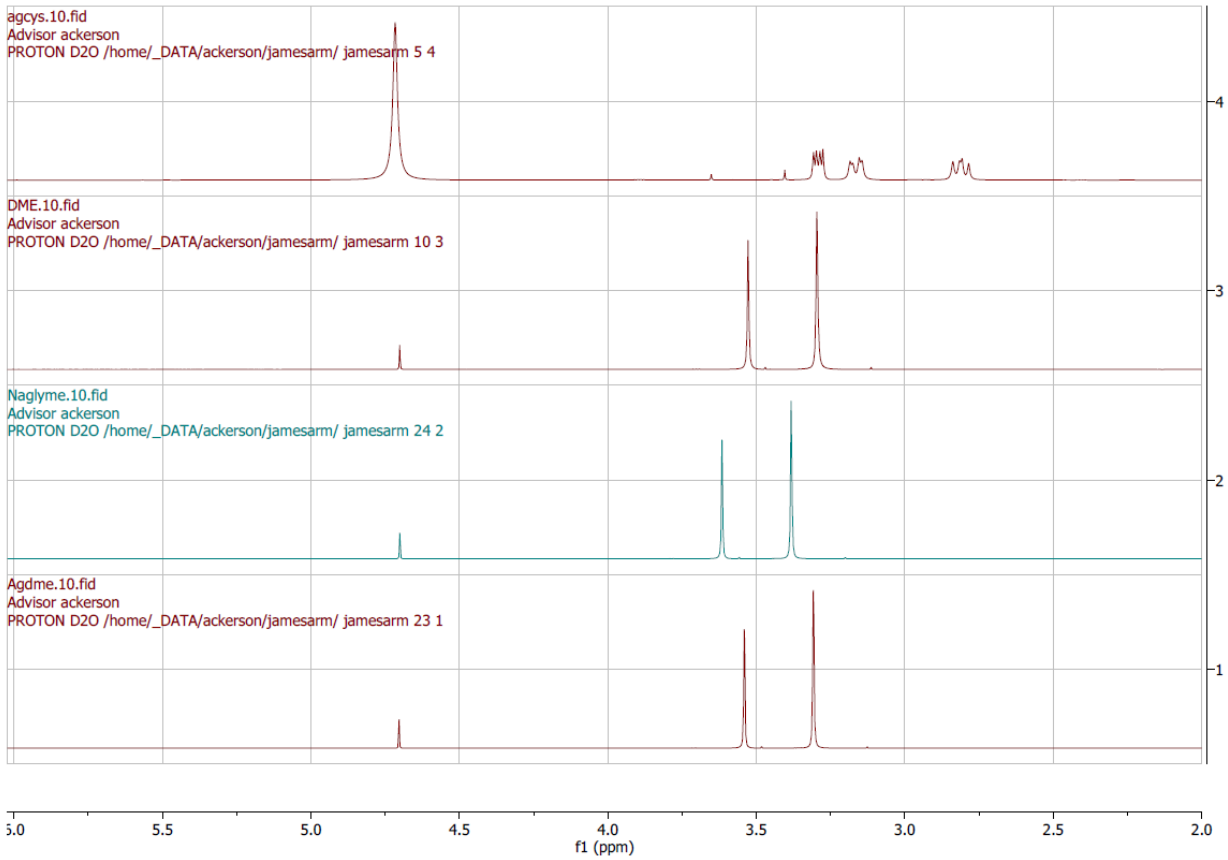

Figure 3.8:[1]H-NMR of 1,2-dimethoxyethane in various environments. Top down: metallogel synthesis, neat DME, DME with sodium ions, DME with silver ions.

Figure 3.8 shows 1H-NMR of 1,2-dimethoxyethane in different environments. Glyme peaks in the metallogel reaction solution are shifted to higher ppm. This could be due to glyme chelating to a metal ion in solution. Glyme is known to be a chelating solvent. Glyme mixed with Ag^+ in aqueous solution has the same peak shifting as neat glyme. When glyme is mixed with Na^+, the resultant peak shift is similar to the metallogel reaction. This could indicate glyme is chelating to Na^+ when added to the synthesis. Earlier, the idea of glyme causing folding of the oligomeric species was introduced. The idea was proposed that insolubility in the reaction solution

would precipitate this folding into AMX colloids. Glyme's chelation to Na^+ ions in solution could be the change in solution that causes this to occur.

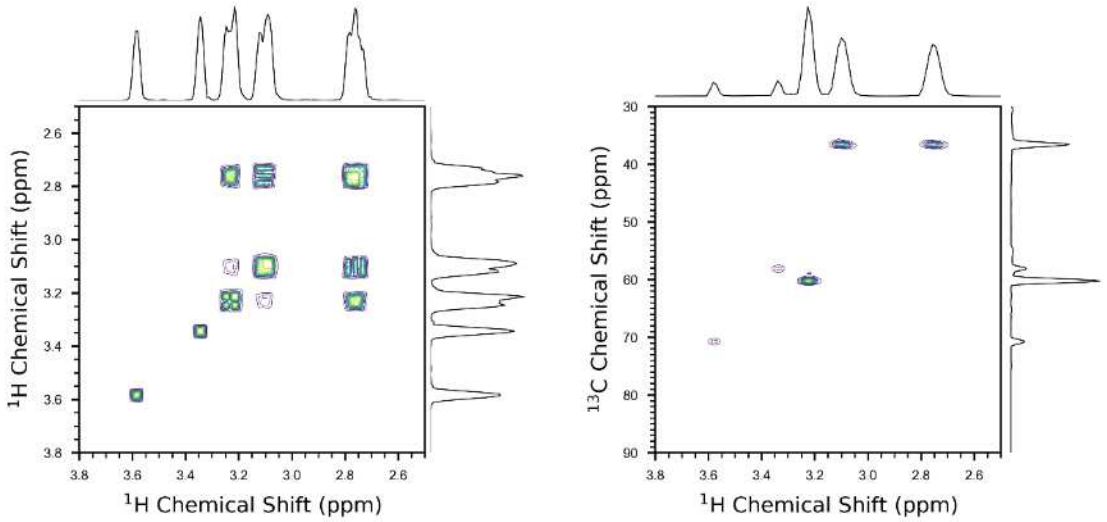

Figure 3.9: The solution NMR results show that strong Ag-cysteine complexes form in these solutions with substantial changes in the chemical shifts of the bound cysteine molecules. The results from 2D ^{1}H{^{13}C} HSQC (right) and ^{1}H COSY (left) experiments indicate that the two sets of peaks centered at 3.1 and 2.7 ppm are diasterotopic protons from the same methylene group on the cysteine group. These peaks are coupled to one another with strong cross peaks in the COSY spectra as well as coupled to the same carbon in the HSQC spectrum.

Figure 3.9 above shows HSQC and COSY data investigating the cysteine ligand. These were run as the peak splitting seen in the 1H-NMR (Figure 3.7) were unusual. 1H-COSY shows the peaks at 3.1 and 2.7ppm are strongly coupled. HSQC confirms these peaks are coupled to the same carbon atom. This result indicates these are diasterotopic protons. This could occur from the ligand being bound on each side by cysteines functional groups. These protons are equivalent in neat cysteine, as they are symmetrical. By binding the cysteine ligand into a larger network, this symmetry is broken, making these protons non-equivalent. This causes the peak splitting.

^{1}H-NMR data provides insight into the results of ^{13}C-NMR in Figure 3.5. ^{13}C-NMR shows broadening of peaks, which can be attributed to cysteine being bound in the network from multiple points i.e. the thiol functional group, and at least one of the carboxylic or amine functional group. The peak splitting seen in Figure 3.7 backs this up, as it can be a product of the ligand being bound.

A structural model of the sol-gel transition for these colloids is informed by Fourier transform infrared spectroscopy (FTIR) (Figure 3.10) and ^{23}Na NMR analysis of material in both the sol and the gel state. FTIR shows a distinct change for cysteine COO^- in the hydrated (sol) versus dehydrated (gel) states. Relative to cysteine, the sol-state cysteine COO^- and NH_2 groups shift to lower energies (7 and 4 cm^{-1}, respectively, Figure 3.4). This arises from network incorporation and/or hydrogen bonding.

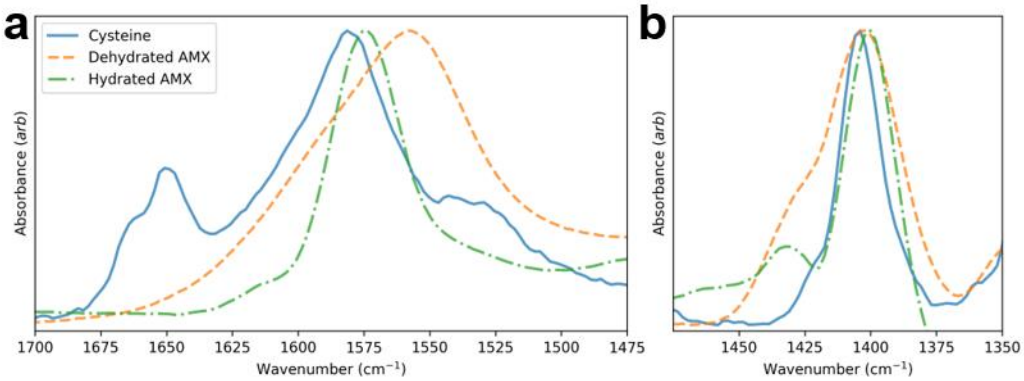

Figure 3.10: FTIR of solid cysteine (solid blue trace), dehydrated AMX (dashed orange trace), and hydrated AMX (dot-dashed green trace). Absorbance values are scaled so peak heights are equivalent to highlight comparisons between a) C=O and b) NH2 stretches.

The COO^- peak for the gel shows a larger redshift of 24 cm^{-1}. A shift of this magnitude is characteristic of cation coordination. Thus, cations (Ag^+ or Na^+) must be coordinated to the COO^- group during the transition from sol to gel. The reversible nature of the sol-gel transition implies that cation coordination is broken by solvation. BDE calculations point to COO^- as the most likely

site for Na^+ coordination, and the relatively weak binding energies for COO-Na imply that dissolution of these bonds occurs more readily than cysteine-Ag^+ bonds. Taken together, this suggests that Na^+ dominates coordination to COO^- during the sol-gel transition.

^{23}Na NMR experiments support Na^+ coordinates to COO^- during the sol-gel transition. A dilute solution of the sol exhibits a sharp peak at 0.2 ppm for Na^+ referenced to a 10 mM NaCl solution (Figure 3.11). This suggests that Na^+ is essentially aqueous in the sol state. This data also suggests Na^+ is excluded from the colloidal component, as colloidally contained Na^+ would produce a second ^{23}Na NMR peak. Indeed, diffusion ordered spectroscopy (DOSY) ^{23}Na NMR gives similar diffusion coefficients for Na^+ in both the sol and in aqueous form (Table S5). In contrast to the single, sharp peak for ^{23}Na in the sol state, solid-state ^{23}Na NMR of the gel shows a single, very broad peak with a chemical shift at -22.1 ppm (Figure 3.11). The breadth of the peak suggests multiple different bonding conformations. Overall, this data suggests that Na^+ is key to the remarkable reversible sol-gel transitioning of this material; it moves from a complex and entrapped solid to essentially aqueous form in the gel to sol transition. Similar behavior is observed in Na-montmorillonite clays, which exhibit peak shift and broadening as the clays dry and trap Na^+ within the interlayer spaces of the microstructures.[25]

FTIR of the sol and gel state displays insignificant peak shift for NH_2, implying no chemical modification to this functional group. The peak does broaden significantly upon gelation, which indicates a more disordered NH_2 bonding environment brought about by water loss. Considering the excess of Ag^+ observed in ICP-MS, and the DFT predicted Ag-N bonding favorability (Figure 3.3), Ag^+ is forming dative bonds to the cysteine NH2. Since these bonds crosslink the -Ag-S- oligomers to construct the AMX network, water must exist within the AMX colloids and must be drawn out to some extent during dehydration. The interparticle network thus

rearranges through water loss and disturbs the hydrogen bond network around the NH_2 moiety, producing a broad peak observed through FTIR.

In context of the larger story, FTIR data shows how the colloids can assemble into the rigid metallogel. DLS data, Figure 3.5, shows a stable secondary structure of coinage-metal thiolates make up the dissolved units for the metallogel. This data, figure 3.10 suggest the colloids assemble into the metallogel through Na^+ coordination to the carboxylic group of cysteine.

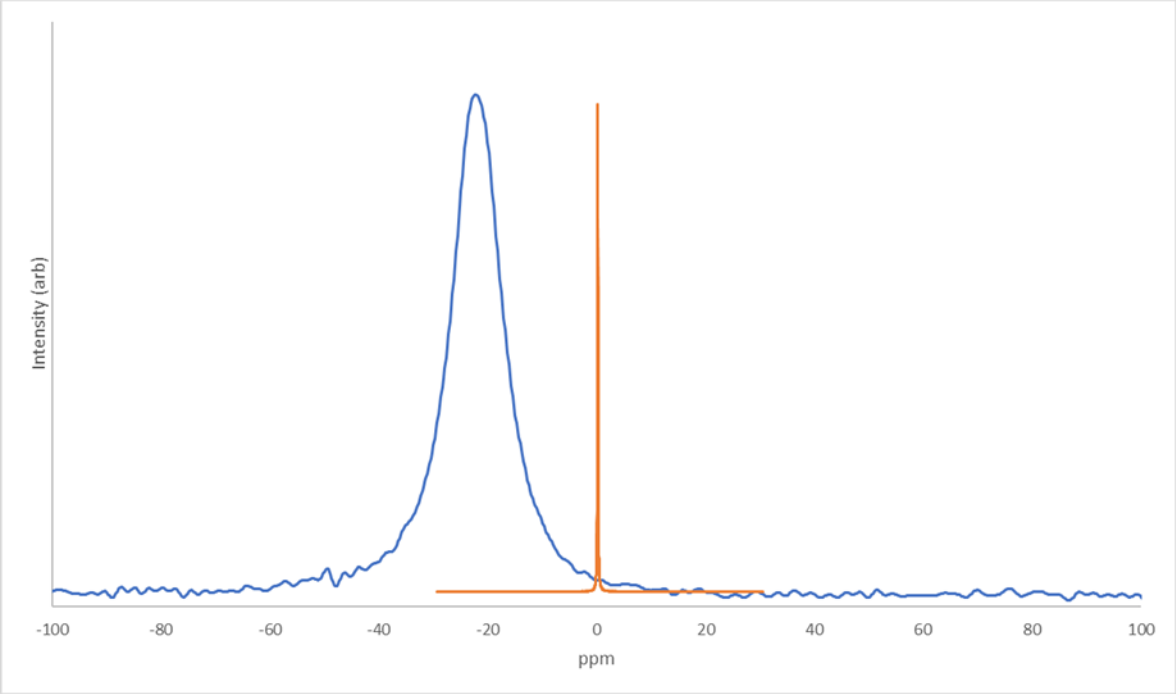

Figure 3.11: ^{23}Na NMR data of AMX in solid state (blue trace) and aqueous AMX (orange trace).

We present a scheme of a potential gel formation based on the above data in Figure 3.12. Metal-thiolate chains (Figure 3.12a, b) compose the AMXs with side-chain functional groups allowing for the gelation of the material through water-content and ion-bridging (Figure 3.12c-f).

The presence of water within the AMX network should impart generous flexibility to the colloid. As such, the colloids are considered aggregates of Ag-cys oligomers without well-defined surface structure. Water retained on the surface of the colloids that passivates Na^+ coordination should also provide some adaptability as the colloids assemble. The flexible colloids are likely capable of structural rearrangement as they assemble to suit their most favorable surface-to-surface interactions.

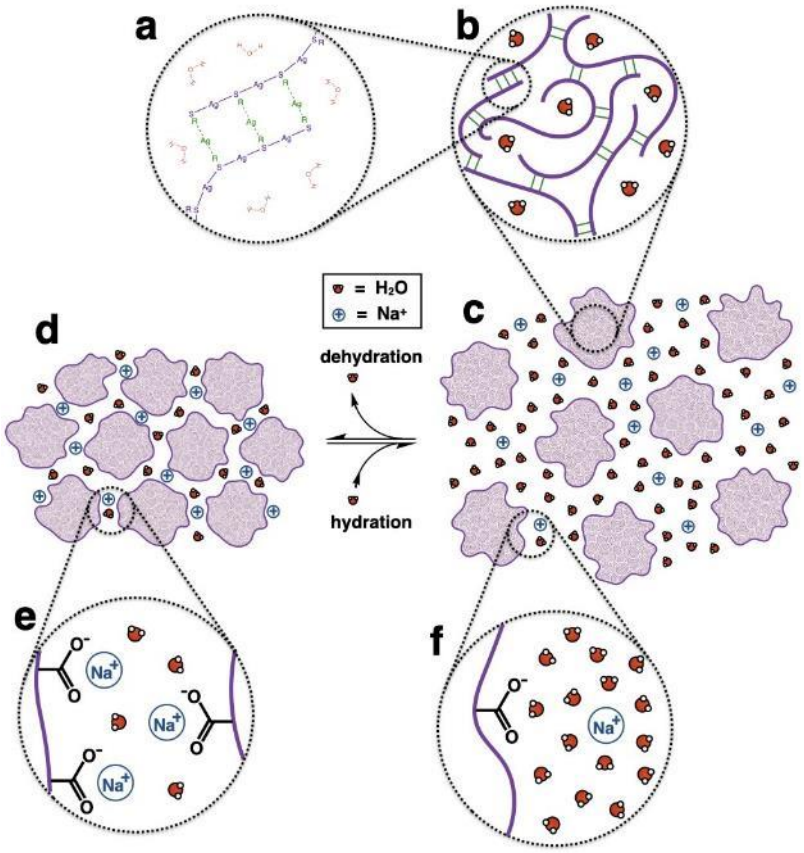

Figure 3.12: Scheme of AMX structure and method of agglomeration. a) Molecular structure of linear silver-cysteine oligomers (purple) bridged through cysteine side chains by free Ag^+ ions (green). b) Illustration of silver-thiolate oligomers (purple lines) bridged by Ag^+ (green lines). c) AMX sol containing flexible, globular colloids solvated by water with aqueous Na^+ ions. d) Dehydration drives the reversible sol-gel transition as AMXs agglomerate and trap Na^+ ions. The flexible colloids are expected to alter their shape to minimize void space. e,f) Insets of interstitial space between colloids in the e) gel state, where Na^+ binds to cysteine's carboxylic acid functional groups, and f) sol state, where aqueous Na^+ ions are freely soluble

In this scenario, dehydration drives colloid assembly to minimize void space and maximize surface interactions in order to retain as little water as possible. This critical moisture content defines the sol-gel transition. Rheology results reflect that dehydration past this point removes structural water and instigates network degradation.

The molecular structures within and between AMX colloids are remarkably similar in the gel phase. Both cases consist of cysteine functional groups bound to a metal cation and stabilized through water-mediated hydrogen bond networks. This is strikingly similar to the published structures of traditional Ag-cys metallopolymers that require cations and water to bridge interpolymer interactions.[18] In disregard of the identity of the cation, a densely packed network of flexible colloids would appear to be a single, continuous network. This architecture is more similar to polymeric materials that form a continuous network through entanglement than to traditional metallogels constructed from hierarchical structures. A continuous network would resolve the origin of this material's exceptional increase in rigidity considering its Young's modulus is on the order of silicon- and carbon-based organic polymers. This chaotic assembly of loosely bound metal complexes out-performs hierarchical structures designed at the nanoscale and requires a new model to understand its rheological behavior.

This synthesis is not unique to silver. Similar results have been shown with copper previously. Herein we also report similar behavior from gold, nickel, and tin materials (Figure 3.13). This result shows the potential broad applicability of the synthesis towards other transition metals. The materials exhibit the same properties as explored above with the silver-cysteine system. Figure 3.13 shows DLS data exhibit similar sized materials in solution, as well as a reversible sol-gel transition controllable through water content. The addition of glyme to disrupt self-assembly of materials can result in rigid metallogel formation of various metals.

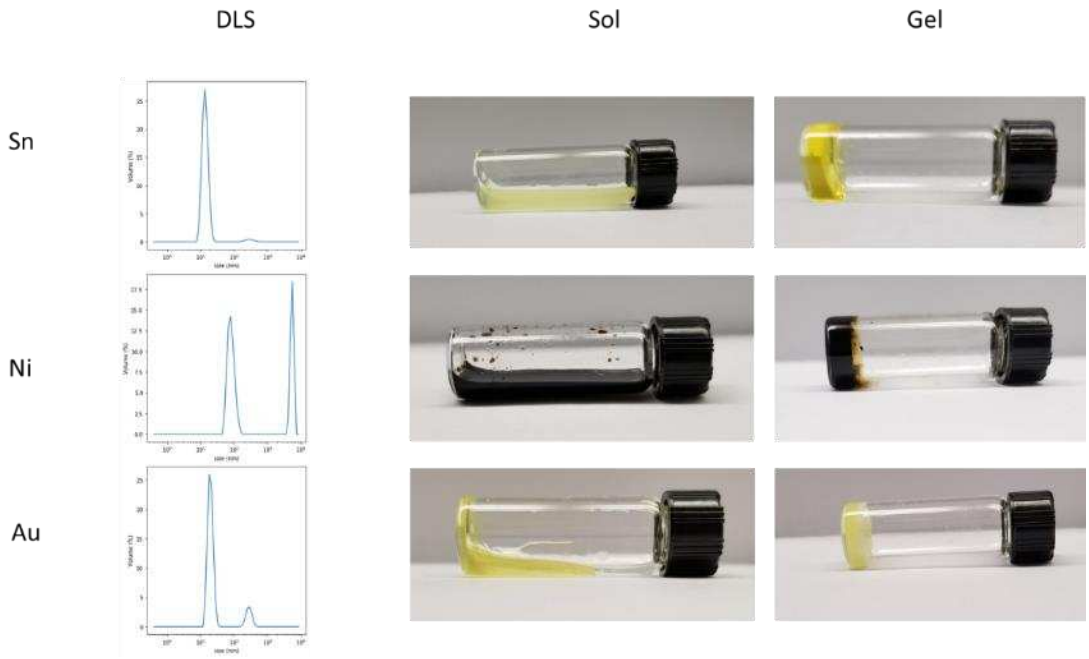

Figure 3.13: DLS, and sol-gel images for similarly formed metallogel systems of tin-glutathione, nickel-thiomalate, and gold-thiomalate.

Figure 3.13 above shows data similar to the data presented before about silver-cysteine metallogels. Similarly, to the Ag-cysteine systems, DLS data shows nanoparticles in the 10-100nm range for all systems. This suggests that the formation of AMX complexes is not unique to silver thiolate materials but can be applied to other metallic systems as well. Figure 3.13 also shows similar water content dependent properties of these new metal-thiolate systems, wherein the samples can be diluted to exhibit solution-like behavior, but at low water content (<5%) they show gel like behavior. Like the silver system, this is a reversible process. Similar products can be formed with non-thiolate ligands, like glutamic acid (Figure S7). However, these metallogels degrade much more quickly and therefore have not been the focus of any in depth study.

Overall, this metallogel system presented herein represents the main body of work presented in this dissertation. The metallogel is synthesized using glyme as an antisolvent to

precipitate the metallogel. The metallogel exhibits interesting properties which present exciting opportunities for this synthesis include: the water-dependent properties, which can be useful for stimuli-responsive materials, such as sensors. Similar supramolecular assemblies can be synthesized using a variety of metals and ligands, allowing for highly specific tuning of properties. Coinage-metal thiolates are also precursors to highly stable nanoparticles. This presents the opportunity for glyme-synthesized assemblies which include nanoparticles. This would make the system worth investigating for the numerous applications of nanoparticles in optics, sensing, energy, and more. The two following chapters, Chapters 4 and 5, will describe attempts to utilize the characteristics of this glyme-synthesized metallogel system for potential applications. Chapter 4 will focus on synthesis of nanoparticles encapsulated by the metallogel, as well as the sintering of this material to create a metal foam, which is desired for applications in additive manufacturing. Chapter 5 will study the antimicrobial properties of the silver-cysteine metallogel discussed here in Chapter 3.

3.4 Conclusion

A unique synthetic approach generates silver-cysteine (Ag-cys) metallogels with unprecedented properties compared to metallophilic hydrogels constructed from the same component pieces. Inclusion of an anti-solvent during synthesis precipitates the precursors as a sol of amorphous metal complex (AMX) colloids. Dehydration drives the sol-gel transition, though some residual water is necessary to stabilize the molecular network. The resulting gels are exceptionally rigid and exhibit a Young's modulus on the order of silicon- and carbon-based polymeric materials. Simulation and experimentation in concert uncover a complex molecular structure that resembles a single continuous network. Such a network resolves the origin of the

unique properties observed in this metallogel compared to compositionally similar materials composed of hierarchical structures.

The method presented herein counterintuitively creates a continuous metal-ligand network where previously reported materials composed of the same building blocks create hierarchical architectures. As such, this work opens the door to rational design of metallogels with previously inaccessible material properties. Overall, this report represents a starting point in exploration of a new class of soft materials.

3.5 Methods and materials

Materials

All Materials were purchased through Sigma-Aldrich. 1,2-dimethyoxyethane (anhydrous, 99.5%, inhibitor-free), DL-cysteine (technical grade), silver nitrate (ACS reagent, ≥99.0%), sodium hydroxide (certified ACS pellets). Water used was nanopure water. Salts used for relative humidity chambers were potassium carbonate (anhydrous, ACS reagent ≥99%), potassium acetate (ACS grade), lithium chloride (ACS reagent, ≥99%), lithium bromide (ReagentPlus®, ≥99%), magnesium chloride (anhydrous, ≥98%), magnesium nitrate hexahydrate (ACS reagent, ≥99%).

NMR Methods

Samples for solution NMR data were prepared in D_2O in a 5 mm (o.d.) tube and spectra collected on a 500 MHz Bruker Avance III spectrometer using a 5 mm Bruker HX Prodigy Cyroprobe. The resonance frequencies for ^{1}H, ^{23}Na, and ^{13}C are 500.08, 132.28, and 125.75 MHz, respectively. The gradient assisted $^{1}H\{^{13}C\}$ HSQC NMR data were collected as complex data points using echo-antiecho acquisition with the *hsqcetgp* pulse sequence included with Topspin 2.1. The data were

collected with a 48 μs delay corresponding to a 20 kHz spectral window in the indirect dimension. The diffusion ordered spectroscopy experiments (DOSY) were collected using biopolar gradients and the *ledbpgp2s* pulse sequence. For ^{1}H, a 2 ms gradient pulse and a 100 ms diffusion time were used to collect 32 spectra over a range of gradient strengths ranging from 2.6 to 116 G/cm. For ^{23}Na, a 2.5 ms gradient pulse and an 80 ms diffusion time were used to collect 44 spectra over a range of gradient strengths ranging from 1.28 to 66 G/cm. Samples for solid-state NMR spectra were contained within 4 mm (o.d.) pencil type rotors and spectra collected using a Revolution NMR HX probe on a 400 MHz Bruker Avance spectrometer at resonance frequencies of 400.09, 105.83 and 100.61 MHz for ^{1}H, ^{23}Na, and ^{13}C, respectively . The ^{23}Na magic angle spinning (MAS) NMR spectra were collected a spinning rate of 12 KHz for 360 acquisitions using a 5.0 s acquisition delay. The $^{13}C\{^{1}H\}$ cross polarization (CP) MAS NMR spectra were collected at a spinning rate of 10 kHz. The cysteine spectra were collected using 2 ms contact pulse and a 3 s acquisition delay for 4 096 acquisitions. The corresponding data for the target sample were collected using a 0.7 ms contact pulse and a 1 s acquisition delay for 16 384 acquisitions. The ^{23}Na and ^{13}C NMR data were referenced with respect to external samples of 0.1 M NaCl solution (δ_{Na} = 0 ppm) and carboxylic acid peak of α-glycine (δ_{C} = 176.56 ppm), respectively.

DFT Calculations

Density functional theory calculations were performed with the NWChem [2] software package, using the Def2-TZVP [3] basis set for non-Ag atoms, the TZP [4] basis set for Ag, and the B3LYP [5, 6, 7] functional. The COSMO [8, 9] model was employed to model the effect of solvation in water. Stable conformers for deprotonated cysteine were obtained by rotating the CH_2S and NH_2 groups in increments of 120° and performing geometry optimizations, resulting in 9 stable conformers. NMR simulations were performed with NWChem using the gauge-independent

atomic orbital method. ^{23}Na isotropic shifts were referenced by calculating the shielding for Na atoms at the center of a 2x2x2 supercell cluster of crystalline NaCl.

SEM of dehydrated AMX

Samples of AMX's were prepared by slowly drying the gel material with desiccant, followed by lyotholization. The resultant solid sample was powdered with a mortar and pestle and mounted on SEM grids. Samples were sputter coated with gold and observed using a JEOL JSM-6500-F scanning electron microscope. Images were taken with a voltage of 15kV.

DLS

Colloid size measurements were made using a Malvern Zetasizer nano ZS with a 633nm laser, utilizing nanopure water as a solvent. Samples were carried out at room temperature with a 1cm cuvette.

GPC-MALS measurement of dispersed AMX

The GPC-MALS analysis was performed under Impact Analytical SOP-SEP-004. The sample was prepared by diluting the 20 μL sample volume up to 1200 μL with HPLC water. The sample solution was transferred to an autosampler vial and injected into an instrument comprised of a Waters 2695 separations module and a Wyatt HELEOS II multi-angle light scattering detector with a Wyatt QELS+ dynamic light scattering module. The sample was prepared by dissolving 1 mg of AMX into 1mL of water. An injection volume of 15μL was used, with a flow rate of 0.5mL/min. Samples were taken every second, with a total of 7200 data points.

Synthesis of silver-cysteine AMX

A scintillation vial is charged with 3mL of 100mM AgNO3(H2O) and a stir bar on a stir plate. The stir plate is set to a medium rate, and 9mL of 100mM Cysteine (0.3MNaOH), followed immediately by 18mL of 1,2-dimethoxyethane. This is allowed to stir for 20 minutes before transfer to a centrifuge tube. The reaction is spun at 5000rpm for 10 minutes, resulting in precipitation of the gel phase, with a clear, colorless supernatant. The supernatant is decanted, and the gel is collected with a pipette.

Rheological measurements of AMX

AMX materials are not elastic and deform if touched, requiring clever experimental design to accurately perform the desired rheological measurements. To achieve adequate sample preparation, AMX solutions of known concentration were deposited directly onto tared 8-mm bottom plates with a rubber mold. Samples equilibrated in sealed relative humidity chambers for two weeks, which was determined to be enough time to equilibrate in a separate study. Immediately before being placed on the rheometer, the plates were weighed to calculate final moisture contents in the sample and the rubber molds were removed. Setup and measurements were performed as quickly as possible to ensure the hygroscopic material did not change before measurement.

Viscosity (η) measurements were collected using a TA Instruments AR2000ex rotational rheometer with a cone and plate geometry attachment (2° cone, 52μm truncation gap, 40mm stainless steel plates) within an environmental test chamber enclosure. Samples with varying moisture content were carefully dispensed via syringe between the upper and lower platens, which were then closed to the truncation gap (wiping away excess material during closure). The environmental chamber doors were then closed around the loaded platens and set to 25°C. Samples were allowed a 30 second equilibration time during a primary conditioning step, followed by a

flow sweep experiment from 0.05 1/s to 100 1/s. Viscosity values were selected from plateaued regions in the resulting viscosity vs shear rate curves.

Dynamic properties (G',G") were measured in compression using a TA Instruments ARES-G2 rheometer using a parallel plate geometry attachment (8mm SS upper plate, lower Peltier plate). Samples with varying moisture content were quickly from environmental chambers to the rheometer, where axial forces were applied to sandwich the samples between the upper and lower plates. Axial forces used were dependent upon the stiffness of the sample according to its physical state. Compressive oscillatory strain sweep experiments were performed for each sample to determine the appropriate compressive oscillatory strain (from the linear viscoelastic region) to use for the next experiment: a time sweep at the selected strain, performed at a frequency of 1Hz. G' and G" values & curve behaviors were collected and evaluated from the resulting G'/G" vs time plots.

XRD

Samples for XRD analysis were prepared by depositing AMX sols onto 6 µm thick polypropylene (PP) sheets, followed by equilibration in a ??% humidity chamber for 48 hours. After the desired humidity was achieved the PP films were inverted onto a polymethyl methacrylate (PMMA) sample holder and sealed with tape, providing a flat surface for XRD analysis. The XRD patterns were collected on a Bruker D8 advance XRD equipped with a LynxEye Si strip detector. Samples were scanned from 2 to 60° 2Θ using a 0.01° step and a 2 seconds per step counting time. A knife edge was installed to eliminate the scattering of X-rays at low angles and the divergence slits were set at 0.5 mm to ensure only the sample was illuminated by the X-rays.

FT-IR

FT-IR was run on a Nicolet IS-50 FT-IR spectrometer. Samples were run using an ATR-ZnSe attachment. 64 scans were averaged per sample with resolution of 0.482cm^{-1}. For the dissolved AMX sample, D_2O was used as a solvent, to move water peaks away from the area of interest.

REFERENCES

1. Chen, L.-J. & Yang, H.-B. Construction of Stimuli-Responsive Functional Materials via Hierarchical Self-Assembly Involving Coordination Interactions. *Acc. Chem. Res.* **51**, 2699–2710 (2018).

2. Randazzo, R. *et al.* Hierarchical Effect behind the Supramolecular Chirality of Silver(I)–Cysteine Coordination Polymers. *J. Phys. Chem. B* **119**, 4898–4904 (2015).

3. Datta, S., Saha, M. L. & Stang, P. J. Hierarchical Assemblies of Supramolecular Coordination Complexes. *Acc. Chem. Res.* **51**, 2047–2063 (2018).

4. Liu, M., Ouyang, G., Niu, D. & Sang, Y. Supramolecular gelatons: towards the design of molecular gels. *Org. Chem. Front.* **5**, 2885–2900 (2018).

5. Bentz, K. C. & Cohen, S. M. Supramolecular Metallopolymers: From Linear Materials to Infinite Networks. *Angew. Chem. Int. Ed.* **57**, 14992–15001 (2018).

6. Hamley, I. W. Nanotechnology with Soft Materials. *Angew. Chem. Int. Ed.* **42**, 1692–1712 (2003).

7. Sangeetha, N. M. & Maitra, U. Supramolecular gels: Functions and uses. *Chem. Soc. Rev.* **34**, 821 (2005).

8. Sposito, G. *et al.* Surface geochemistry of the clay minerals. *Proc. Natl. Acad. Sci.* **96**, 3358–3364 (1999).

9. Du, X., Zhou, J., Shi, J. & Xu, B. Supramolecular Hydrogelators and Hydrogels: From Soft Matter to Molecular Biomaterials. *Chem. Rev.* **115**, 13165–13307 (2015).

10. Fages, F. Metal Coordination To Assist Molecular Gelation. *Angew. Chem. Int. Ed.* **45**, 1680–1682 (2006).

11. Piepenbrock, M.-O. M., Lloyd, G. O., Clarke, N. & Steed, J. W. Metal- and Anion-Binding Supramolecular Gels. *Chem. Rev.* **110**, 1960–2004 (2010).

12. Söptei, B. *et al.* The supramolecular chemistry of gold and l -cysteine: Formation of photoluminescent, orange-emitting assemblies with multilayer structure. *Colloids Surf. Physicochem. Eng. Asp.* **470**, 8–14 (2015).

13. Cook, T. R., Zheng, Y.-R. & Stang, P. J. Metal–Organic Frameworks and Self-Assembled Supramolecular Coordination Complexes: Comparing and Contrasting the Design, Synthesis, and Functionality of Metal–Organic Materials. *Chem. Rev.* **113**, 734–777 (2013).

14. Zhu, Q.-L. & Xu, Q. Metal–organic framework composites. *Chem Soc Rev* **43**, 5468–5512 (2014).

15. Fucke, K., Peach, M. J. G., Howard, J. A. K. & Steed, J. W. A new water···Na+ coordination motif in an unexpected diatrizoic acid disodium salt crystal form. *Chem. Commun.* **48**, 9822 (2012).

16. Kumar, D. K. & Steed, J. W. Supramolecular gel phase crystallization: orthogonal self-assembly under non-equilibrium conditions. *Chem Soc Rev* **43**, 2080–2088 (2014).

17. Odriozola, I., Loinaz, I., Pomposo, J. A. & Grande, H. J. Gold–glutathione supramolecular hydrogels. *J. Mater. Chem.* **17**, 4843 (2007).

18. Odriozola, I., Ormategui, N., Loinaz, I., Pomposo, J. A. & Grande, H. J. Coinage Metal–Glutathione Thiolates as a New Class of Supramolecular Hydrogelators. *Macromol. Symp.* **266**, 96–100 (2008).

19. Boonkaew, B., Kempf, M., Kimble, R., Supaphol, P. & Cuttle, L. Antimicrobial efficacy of a novel silver hydrogel dressing compared to two common silver burn wound dressings: Acticoat^{TM} and PolyMem Silver®. *Burns* **40**, 89–96 (2014).

20. Sorensen, C. M. & Chakrabarti, A. The sol to gel transition in irreversible particulate systems. *Soft Matter* **7**, 2284–2296 (2011).

21. Luzuriaga, A. R. de *et al.* "Metallophilic crosslinking" to provide fast-curing and mendable poly(urethane-metallothiolate) elastomers. *J. Polym. Sci. Part Polym. Chem.* **53**, 1061–1066 (2015).

22. Ashby, M. *Materials Selection in mechanical Design*. (Butterworth-Heinemann, January 1, 10`7).

23. Chang, Y.-M., Lu, I.-T., Chen, C.-Y., Hsieh, Y.-C. & Wu, P.-W. High-yield water-based synthesis of truncated silver nanocubes. *J. Alloys Compd.* **586**, 507–511 (2014).

24. Bensebaa, F., Ellis, T. H., Kruus, E., Voicu, R. & Zhou, Y. Characterization of Self-Assembled Bilayers: Silver−Alkanethiolates. *Langmuir* **14**, 6579–6587 (1998).

25. Ohkubo, T., Saito, K., Kanehashi, K. & Ikeda, Y. A study on hydration behaviors of interlayer cations in montmorillonite by solid state NMR. *Sci. Technol. Adv. Mater.* **5**, 693–696 (2004).

CHAPTER 4: MATERIAL PROPERTY ANALYSIS OF COINAGE-METAL THIOLATE ASSEMBLIES FOR FUTURE APPLICATIONS IN DIRECT-INK WRITING*

4.1 Synopsis

The previous chapter, Chapter 3, discusses the underlying structure of a rigid coinage-metal thiolate metallogel with water content dependent properties. At the right water content, the metallogel can be self-supporting, yet also extruded through the use of an external force. The metallogel described in Chapter 3 is made from the same precursors as the nanoclusters described in Chapter 2. One objective of Chapter 4 was the synthesis of metal nanoclusters or nanoparticles which are trapped in the metallogel. The rheological and sintering properties of this glyme-synthesized compound of nanoparticles encapsulated in a gel are then studied as an investigation into the future use of this assembly for potential future applications in additive manufacturing.

Metal foams are of interest for potential laser targets. The objective was to use a gold metallogel system to develop direct ink write inks for the 3d printing of gradient density gold foams. Nanoparticles are known to sinter at temperatures below the melting point of the bulk metal. Project goals were to (1) develop gel-encapsulated nanoparticles and (2) sinter the nanoparticles into a metallic foam. Nanoparticle gels were successfully synthesized and sintered into a metallic network, however, control over the post-sintered structure was not exhibited.

* *This chapter includes unpublished work. James Armstrong's contribution includes synthetic design, data analysis, and experimental design including TGA, SEM/EDS, and optical microscopy.*

4.2 Introduction

Porous metallic networks substrates, such as foams or aerogels, have a high surface area, with low density.[1,2] These properties make them appealing for new technological applications in electronics, catalysis, and energy storage.[1,3–5] The formulation of porous nanostructures for many metals, e.g. Cu, Ni, have been reported.[6,7] Golds' excellent chemical stability and conductive make gold nanostructures are of specific interest for applications such as targets for high-power lasers.[2]

One typical route to nanoporous materials is the use of a sacrificial template. A sacrificial template material with the target porosity or structure is loaded with precursors to the metal of interest, either metal salts or nanoparticles. Removal of the initial template will leave a resultant metal material with the designed porosity. For example, Zhang et al. utilized polystyrene microspheres to form a sacrificial template.[8] The template was seeded with gold nanoparticles and $HAuCl_4$ to coat the polystyrene with gold. Heating above 400°C decomposes polystyrene, leaving a porous gold foam. This is an effective method, but also has a complex fabrication process, including the waste of sacrificial materials.[9]

Another method for the smart design of specific structures of materials is additive manufacturing.[10] Additive manufacturing is the industrial process of 3D printing. This is a field of large current interest for improving the machining of metals, plastics, and other materials. One aspect of additive manufacturing with lots of fundamental research is the printing of metal parts with specific geometry.[11–13] The end goal being new technologies to allow for the automated production of complex and multifunctional systems.[11,13]

One common method used in additive manufacturing is direct ink writing (DIW).[14] Direct ink writing is a method where an ink is extruded through a nozzle to build 3D structures. This process is widely used through commercial and hobby 3D printers for polymer inks, such as

polylactic acid, commonly known as PLA. However, while this process has been well studied for organic polymers, the DIW of metallic structures is still in development.

The use of supramolecular materials may present a pathway to additive manufacturing of polymeric and metal parts through use as DIW inks.[15–18] The self-supporting properties of supramolecular assemblies allows them to be used to build 3-dimensional structures through DIW printing.[15]

The printing of metal parts differs from the printing of polymeric parts as metals cannot easily be melted or extruded through a printing nozzle to create 3D structures. One major work around to creating printed metal parts is the use of nanoparticles. Nanoparticles can be loaded into a feedstock printable ink and then sintered to create a metallic network.[14,17] Sintering is the process where nanoparticles will fuse together, creating a bulk metallic structure.[19] Nanoparticles can sinter at temperatures lower than the melting point of metals. This allows for the processing of metal parts to be done at lower temperatures than typical processes.

Typically, metal nanoparticles are loaded into a feedstock, which is an existing polymer DIW ink, which is then used to print the basic structure. This can create further processing needs as the feedstock material must be removed post formulation. Using a feedstock material which includes the metal that is desired for a part can be an avenue to work around these issues.

It was proposed using the metallogel as a DIW ink. As discussed briefly in chapter 1 of this dissertation coinage metal-thiolates are precursors to coinage metal nanoparticles.[20,21] The metallogel described in Chapter 3 is composed of coinage metal-thiolate assemblies. This means there is potential to reduce the metallogel in question into small nanoparticles, which will remain encapsulated in the metallogel. To investigate the viability of this process the following objectives

were formed: the reduction of metal-thiolate assembly into nanoparticles, while retaining gel-like properties and the sintering of the nanoparticle metallogel into a bulk metallic structure. A scheme is shown in Figure 4.1 below, outlining the basic idea.

In Chapter 3, the synthesis of metallogels utilizing glyme as an antisolvent was discussed. This metallogel system shares a synthetic pathway with small metal nanoparticles, shown in Figure 4.1. It stands to reason that reduction of the metallogel can produce nanoparticles encapsulated in the metallogel. This hybrid nanoparticle metallogel should still maintain the physical properties of the metallogel discussed in Chapter 3 allowing for it to be utilized as an additive manufacturing material for the processing of metal foams. Presented here is work towards producing small nanoparticles encapsulated by the metallogel by adding a reducing agent during the metallogel formation, as well as an investigation into the processing of metal foams through sintering.

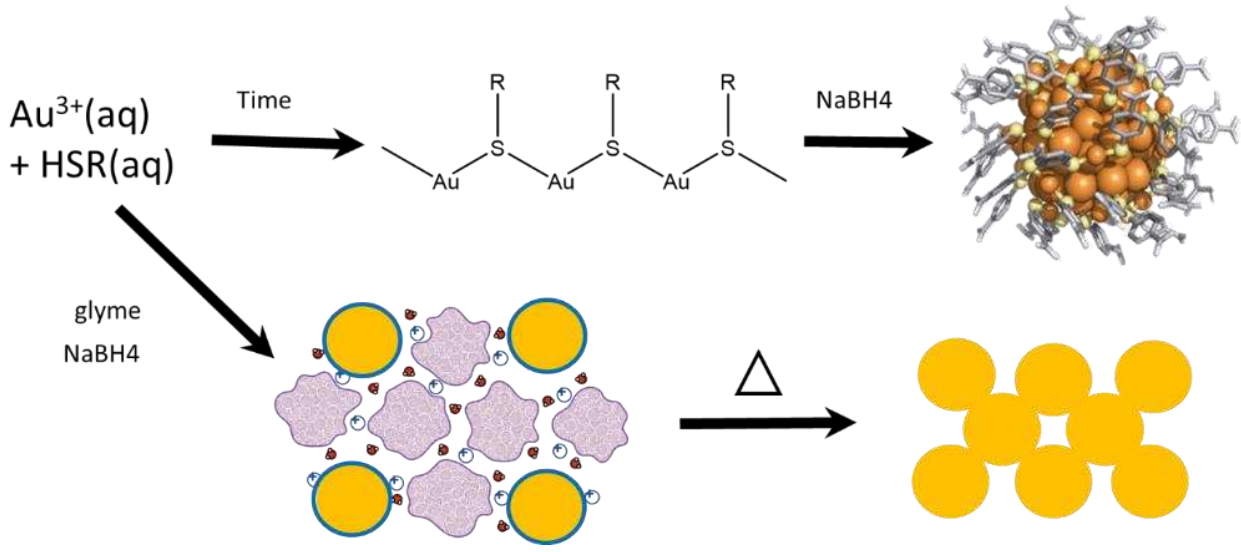

Figure 4.1: A scheme showing the synthetic route to form gold foams. The top route shows a typical synthetic pathway for gold nanoclusters where gold-thiolate oligomers are formed before reduction into nanoclusters. The bottom pathway shows the proposed synthetic pathway for metal foams, where a gold-thiolate metallogel is reduced to form nanoparticles, which are sintered into a foam network.

This project was funded to research the feasibility of this metallogel for the printing and control over gradient density gold foams. To show feasibility the following goals were set: the ability to form metallogel encapsulated nanoparticles, show shear thinning character of the metallogel as proof of concept for use as a DIW ink, and to sinter the metallogel encapsulated nanoparticles and observe the resultant metallic structure. Shown here is the synthesis of metallogel encapsulated nanoparticles, rheological data supporting the feasibility of this metallogel as a DIW ink and post sintering images of the resultant metallic gold structure.

4.3 Results and Discussion

The goal of this project was to create printed gold foams through the use of the novel metallogel described in previous chapters as a DIW ink. To prove feasibility of using the metallogel as a DIW ink, it must meet the basic characteristics needed for a viable DIW ink. A such, the first objective of this project was to see if the material is shear thinning. Shear thinning is a non-Newtonian characteristic of a material, where viscosity is lowered as shear strain is increased. One great example of this is toothpaste. Toothpaste does not freely flow from the tube, but when sufficient force is applied, toothpaste will flow out from the nozzle of the tube onto a toothbrush. This same behavior is required for DIW inks, as the inks should be self-supporting when under no strain, but strain can be applied to extrude the ink through the nozzle, allowing for the controlled deposition of the ink in the desired shape and structure.

Shear thinning behavior is studied through rheology. Rheology is the study of the flow of a material. Shear thinning behavior for a silver- cysteine metallogel is shown below in Figure 4.2.

Figure 4.2 shows the shear thinning behavior of the metallogel. This was done using a silver cysteine system as this experiment was run during the same time frame as the silver-cysteine experimentation done previously in Chapter 3 above. This was done using parallel plate rheology. In parallel plate rheology, a material sample is held between 2 flat plates. The bottom plate is oscillated at a known shear rate, while the response of the material in question is measured by the signal measured by the top plate in relation to the stress. Figure 4.2 shows the viscosity (Pascal seconds) vs shear rate (1/s). As shear rate is increased, the viscosity of the material decreases. This is shear thinning behavior.

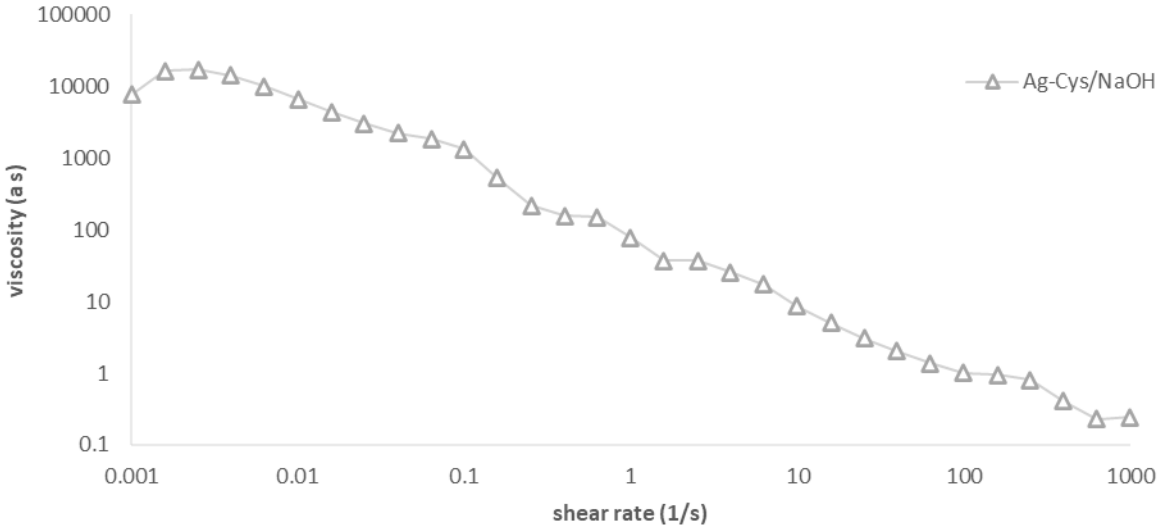

Figure 4.2: Rheology data showing viscosity as a function of shear rate for a silver-cysteine metallogel. The metallogel exhibits shear thinning behavior when shear rate is increased viscosity decreases.

The second objective of this project was the formation of nanoparticles in the metallogel. The metallogel is composed of metal-thiolate oligomers, which are a known precursor to nanoclusters. Two synthetic pathways were studied for the formation of nanoparticles, during

metallogel formation and post-synthesis of the metallogel. Metallogel formation is induced by the addition of sufficient amounts of glyme to a solution containing a metal ion and a thiolate ligand. To form nanoparticles during metallogel synthesis, a reducing agent, $NaBH_4$, was added to glyme prior to glymes addition to the solution. Figure 4.3 below shows a TEM micrograph of the resultant nanoparticles from the use of 1mM $NaBH_4$ in 1,2-dimethoxyethane added to a gold thiomalate solution.

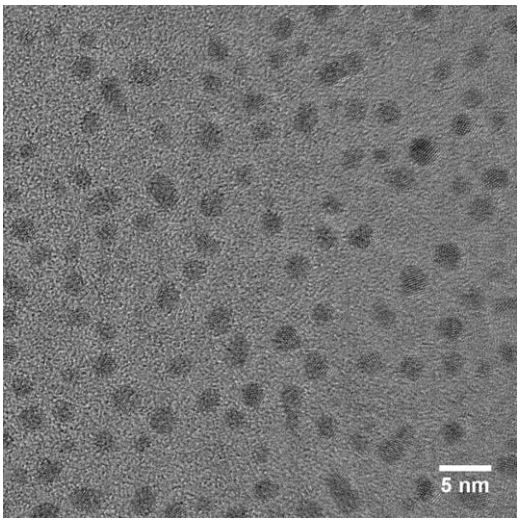

Figure 4.3: TEM micrograph of Au-thiomalate nanoparticles.

Nanoparticles were isolated from the metallogel using PAGE. In PAGE, an electric field is applied across an acrylamide gel. The components of the sample are separated based on their electrophoretic mobility. The nanoparticles in the metallogel move at a different rate than the metallogel itself, due to their size, as well as surface charge. When sufficient separation has occurred, the nanoparticle band on the acrylamide gel is cut out and crushed using a mortar and pestle. This gel is soaked in water to extract the water-soluble metal nanoparticles. These nanoparticles are shown above in Figure 4.3.

The nanoparticles produced through reduction during metallogel formation have an average size of 2nm. The well controlled size distribution of the resultant nanoparticles is thought to be a byproduct of the metallogel formation. As discussed in chapter 3, the metallogel is composed of metal-thiolate oligomers with a radius around 40nm. Perhaps reduction of a single such oligomer into a single tightly packed metal nanoparticle could result in the size similarities exhibited here. It was also noted that increased amounts of the reducing agent resulted in the lack of metallogel formation. Presumably, if enough of the metal-thiolate oligomers were reduced into nanoparticles, there would no longer be enough oligomers left to create a metallogel network.

Shown here was a modification of that synthesis, utilizing sodium borohydride to reduce the metallogel during synthesis creates a hybrid material, where metal nanoparticles are encapsulated by the metallogel, which still exhibits gel-like behavior. In other words, reduction of the material to nanoparticles does not destroy the assembly or interrupt the assembly mechanism. On this note, the assembly will be destroyed if an excess of reducing agent is added. This makes sense, as the assembly is formed from the underlying metal-thiolate oligomers, as discussed in Chapter 3. If enough of this material is reduced to nanoparticles, the assembly mechanism is no longer possible, and a solution of nanoparticles is formed instead.

Post-synthesis reduction of the metallogel was also attempted. In these experiments various concentrations of $NaBH_4$ in water was added to metallogel samples. It was hypothesized that this technique might allow for slow diffusion of $NaBH_4$ through the metallogel. This could potentially further reduce the top layer of metallogel, with less reducing agent reaching the lower parts of the sample. In theory, the hope here was that exposure to larger concentrations of $NaBH_4$ would reduce the top layers of the metallogel further than the bottom layers, in hopes of creating a gradient of resultant nanoparticles in the gel, with larger nanoparticles on top, and nanoparticles

being lower further down the sample. In practice, this resulted in large nanoparticles, resulting in a breakdown in the gel-like behavior of the material. From these experiments, reduction during synthesis presented the best pathway to creating a metallogel containing metal nanoparticles. It is of interest to note silver metallogels formed nanoclusters when exposed to UV light. These nanoclusters formed crystals, Figure S8, however sufficient diffraction data from single-crystal XRD to resolve the crystal structure was never achieved.

If the nanoparticle metallogel is to be viable as a DIW ink, the material must be sintered, leaving a metallic network. To best optimize this process, the temperature at which organic ligands were removed from the material was needed. This was done using thermogravimetric analysis, TGA, to see what temperature all the ligands are removed, shown below in Figure 4.4. This experimentation was done using a gold-thiomalate system, same as the nanoparticle TEM work done above.

TGA was run, increasing the temperature of a gold-thiolate nanoparticle metallogel sample by 10°C every minute up to 700°C. Figure 4.4 shows TGA of the gold-thiomalate nanoparticle metallogel. After 600°C there is no more weight loss seen, even with temperatures up to 700°C. This shows that in order to fully remove ligands from the network, the material must be heated to 600°C.

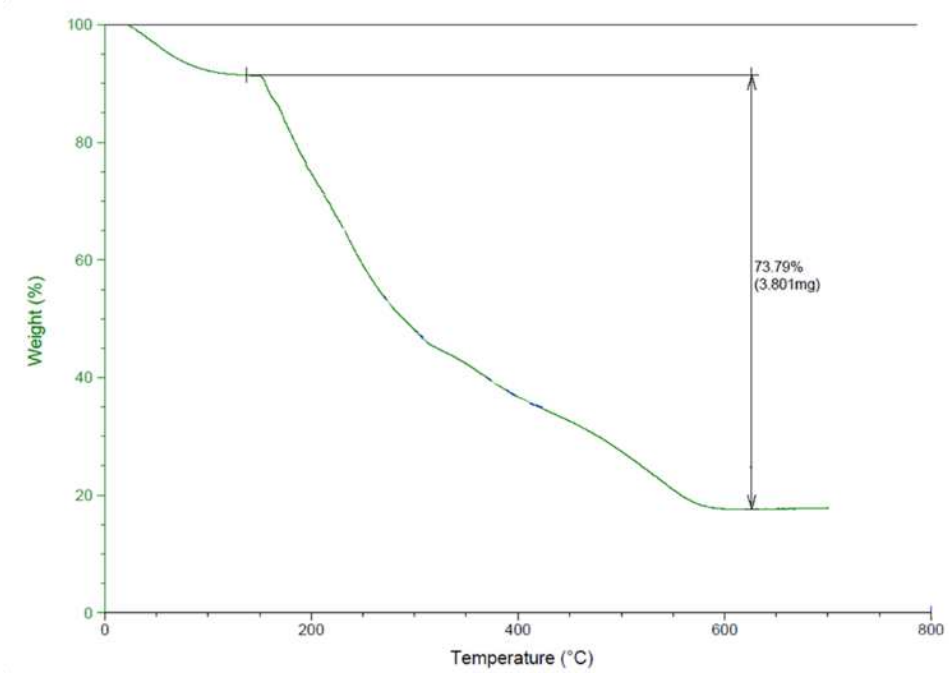

Figure 4.4: Thermogravimetric Analysis of a gold-thiomalate metallogel. TGA shows mass loss of the metallogel until 600°C, at which point only bulk gold remains.

The final step for showing feasibility of the metallogel as a DIW feedstock for metal printing was to sinter the material and observe the final nanostructure of the resultant metal material. Sintering was done using a tube furnace at 650°C under a slight reducing atmosphere of N_2 gas. This atmosphere was controlled to prevent oxidation during sintering. This is a common technique used to prevent the oxidation of sintered nanoparticles when done at atmospheric pressure, as done here. Figure 4.5 below shows an optical microscope image of the sintered material, as well as Figures S9, S10.

Figure 4.5: Optical Microscope image of gold foam post sintering.

Figure 4.5 shows the sintered gold system. Under an optical microscope the material appears to have the look of gold. The sintered material does not appear to have a flat surface, but rather an uneven surface. Originally, the goal was to print gradient density gold foams. This does appear from this image as though a foam like structure might have been produced. Scanning electron microscopy, SEM, was used to look closer at the micro/nanostructure of the material. Figure 4.6 below shows SEM micrographs of the sintered gold network.

The microstructure of the sintered network does appear to be foam-like in appearance. Figure 4.6a shows a cut of the material, exposing the inner structure, which appears porous. Figure 4.6b shows a closer look, examining the nanostructure of the material. From this magnification, The sintered gold network appears to be largely consisting of large, ~100nm, nanoparticles. From this initial proof of concept work, it is shown that this metallogel system can be sintered into a foam-like network. This structure is vastly different from The synthesized microstructure, Figures S11-S13.

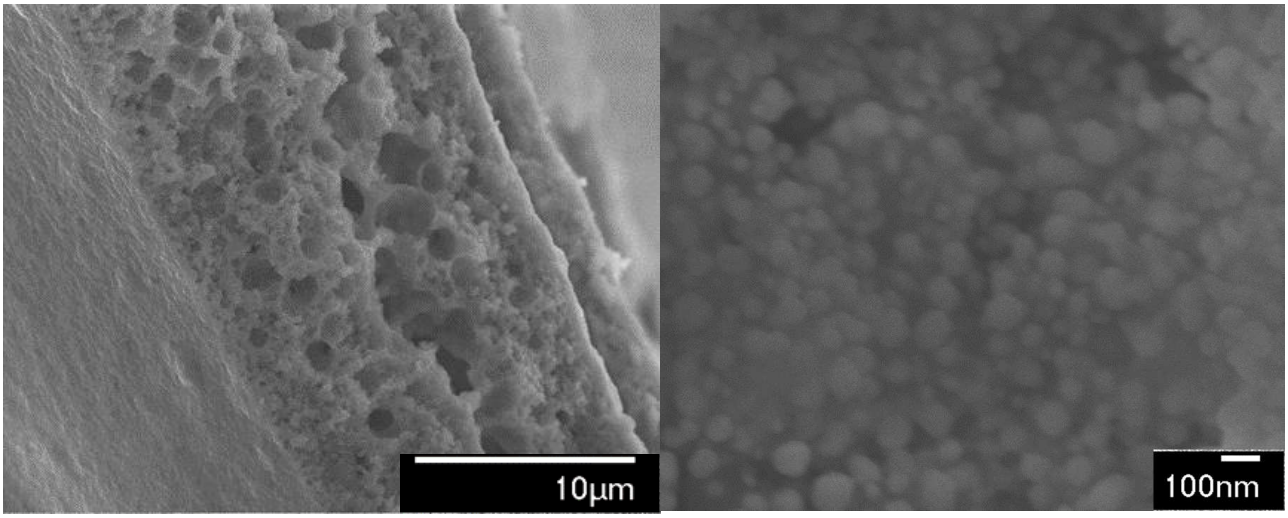

Figure 4.6: SEM micrographs of sintered gold foam showing (a) the foam-like microstructure of the gold foam, and (b) the makeup of the foam, which resembles large 100nm nanoparticles.

One interesting point of note is lack of control over post-sintered structure. Post-sintered microstructure could not be readily determined by the pre-sintered structure of the metallogel. This can be attributed to the presence of water, playing a structural role in the gel-phase of the assembly, as discussed in Chapter 3. Water is removed in the sintering process well before the nanoparticles can form a larger bulk network, as TGA shows a large drop at 100°C, which can be attributed to the removal of water from the system. Removing water from the system as it plays a structural role can cause the assembly to crumble into a powder prior to complete sintering. This limits the control and design of the post-sintered network by imposed pre-sintered structure.

The material was very brittle and fell apart with any sort of handling. Energy-dispersive X-ray spectroscopy (EDS) was utilized to look at the chemical makeup of the material (Figures S14-17). EDS analysis indicates the presences of sulfur and sodium throughout the resultant

material. This indicates that sintering did not result in solely a gold foam. The presence of other elements and potential composites could explain the brittleness of the post-sintered product.

There were quite a few experiments exposing limitations, or areas needing further research in this project. Similar experiments were tried using a silver and copper metallogels. The sintering of these systems resulted in an oxidized product of a black crumbling material which would not maintain its shape. For the gold-based systems, no control over the post sintered structure was exhibited by controlling the pre-sintered structure. There are a few possibilities for this due to the inherent nature of the metallogel. Previously discussed in Chapter 3 water plays a structural role in the metallogel. During the sintering process, water will be removed as temperatures reach above 100°C, thereby destroying any structure held together by the hydrogen bonding of water molecules in the metallogel. Another potential pitfall is the structural component of the ligands. The organic compound, thiomallic acid in the case of the gold system explored here, will decompose, and be removed from the system during sintering. Any structure that occurs from this ligand, either in the metallogel itself, or supporting nanoparticles in the metallogel, will be removed when this ligand is decomposed. If this decomposition occurs before the sintering of the nanoparticles, any ligand-based structure will be lost. These reasons are hypothesized to be the cause for current inability to control the resultant porosity of the gold foam post sintering.

4.4 Conclusions

Shown here is a feasibility study towards using this metallogel for additive manufacturing applications. The viability of the metallogel as a DIW ink is explored, showing the shear thinning character of the material. Synthesis of nanoparticles encapsulated by the metallogel is also shown. The sintering of these nanoparticles to create a bulk gold foam like material is visualized using

SEM and TEM. This proof of concept work shows potential for the application of the metallogel in additive manufacturing.

4.5 Experimental

Materials

All Materials were purchased through Sigma-Aldrich. Gold(III) chloride trihydrate ($HAuCl_4*3H_2O$, ACSreagent, >49.0% Au basis), 1,2-dimethyoxyethane (anhydrous, 99.5%, inhibitor-free), DL-cysteine (technical grade), silver nitrate (ACS reagent, ≥99.0%), sodium hydroxide (certified ACS pellets). Water used was nanopure water.

Synthesis of Nanoparticle gels

A scintillation vial is charged with 3mL of 100mM $HAuCl_4$ (H2O) and a stir bar on a stir plate. The stir plate is set to a medium rate, and 9mL of 100mM thiomalic acid (0.3MNaOH), followed immediately by 18mL of 1,2-dimethoxyethane. This is allowed to stir for 20 minutes before transfer to a centrifuge tube. The reaction is spun at 5000rpm for 10 minutes, resulting in precipitation of the gel phase, with a clear, colorless supernatant. The supernatant is decanted, and the gel is collected with a pipette.

Rheology

Rheology was done in the same manner as explained in chapter 3. AMX materials are not elastic and deform if touched, requiring clever experimental design to accurately perform the desired rheological measurements. To achieve adequate sample preparation, AMX solutions of known concentration were deposited directly onto tared 8-mm bottom plates with a rubber

mold. Samples equilibrated in sealed relative humidity chambers for two weeks, which was determined to be enough time to equilibrate in a separate study. Immediately before being placed on the rheometer, the plates were weighed to calculate final moisture contents in the sample and the rubber molds were removed. Setup and measurements were performed as quickly as possible to ensure the hygroscopic material did not change before measurement.

Viscosity (η) measurements were collected using a TA Instruments AR2000ex rotational rheometer with a cone and plate geometry attachment (2° cone, 52μm truncation gap, 40mm stainless steel plates) within an environmental test chamber enclosure. Samples were carefully dispensed via syringe between the upper and lower platens, which were then closed to the truncation gap (wiping away excess material during closure). The environmental chamber doors were then closed around the loaded platens and set to 25°C. Samples were allowed a 30 second equilibration time during a primary conditioning step, followed by a flow sweep experiment from 0.05 1/s to 100 1/s. Viscosity values were selected from plateaued regions in the resulting viscosity vs shear rate curves.

TEM

Nanoparticles are separated from the gel using PAGE. PAGE is run using a buffer of 89 mM Tris base, 89 mM boric acid, and 2mM EDTA (TBE). PAGE is run using a VWR power source at a constant voltage of 125V for 3:00 hours. Samples are mixed 1:1by volume with 50/50 %b/v glycerol:water to assist loading into gel. After visible separation of the gel layer from the nanoparticles, the nanoparticle band was cut out of the gel. This layer was crushed using a mortar and pestle, then soaked in water to extract the nanoparticles. Nanoparticles were dispersed on Ted Pella 1840 grids, carbon film on 200 mesh copper. Images were taken with a JEOL JEM-2100F Transition Electron Microscope at an acceleration voltage of 200kV,

SEM/EDS

Samples were sintered at 650°C under N_2 gas in a Thermo Fisher Linberg Blue M tube furnace . Samples were observed using a JEOL JSM-6500-F scanning electron microscope. Images were taken with a voltage of 15kV. EDS measurements were taken using an Oxford Instruments energy dispersive X-ray spectrometer.

REFERENCES

1. Banhart, J. Manufacture, characterisation and application of cellular metals and metal foams. *Prog. Mater. Sci.* **46**, 559–632 (2001).

2. Qian, F. *et al.* Gold Aerogel Monoliths with Tunable Ultralow Densities. *Nano Lett.* **20**, 131–135 (2020).

3. Zhu, C. *et al.* Toward digitally controlled catalyst architectures: Hierarchical nanoporous gold via 3D printing. *Sci. Adv.* **4**, eaas9459 (2018).

4. Dong, S. *et al.* High-purity foam-like micron-sized gold cage material with tunable plasmon properties. *Sci. Rep.* **10**, 16555 (2020).

5. Du, R. *et al.* Engineering Self-Supported Noble Metal Foams Toward Electrocatalysis and Beyond. *Adv. Energy Mater.* **10**, 1901945 (2020).

6. Tang, Y. *et al.* Ultralow-density copper nanowire aerogel monoliths with tunable mechanical and electrical properties. *J. Mater. Chem. A* **1**, 6723 (2013).

7. Jiang, B. *et al.* Ultralight metal foams. *Sci. Rep.* **5**, 13825 (2015).

8. Zhang, K., Tan, X., Wu, W. & Tang, Y. Template synthesis of low-density gold foams: Density, microstructure and compressive strength. *Mater. Res. Bull.* **48**, 3499–3504 (2013).

9. Egorov, V. & O'Dwyer, C. Architected porous metals in electrochemical energy storage. *Curr. Opin. Electrochem.* **21**, 201–208 (2020).

10. Wong, K. V. & Hernandez, A. A Review of Additive Manufacturing. *ISRN Mech. Eng.* **2012**, 1–10 (2012).

11. Espalin, D., Muse, D. W., MacDonald, E. & Wicker, R. B. 3D Printing multifunctionality: structures with electronics. *Int. J. Adv. Manuf. Technol.* **72**, 963–978 (2014).

12. Kullmann, C. *et al.* 3D micro-structures by piezoelectric inkjet printing of gold nanofluids. *J. Micromechanics Microengineering* **22**, 055022 (2012).

13. Xu, C., Quinn, B., Lebel, L. L., Therriault, D. & L'Espérance, G. Multi-Material Direct Ink Writing (DIW) for Complex 3D Metallic Structures with Removable Supports. *ACS Appl Mater Interfaces* 8 (2019).

14. Auyeung, R. C. Y. Laser Direct-Write of Metallic Nanoparticle Inks. *J. Laser MicroNanoengineering* **2**, 21–25 (2007).

15. Pekkanen, A. M., Mondschein, R. J., Williams, C. B. & Long, T. E. 3D Printing Polymers with Supramolecular Functionality for Biological Applications. *Biomacromolecules* **18**, 2669–2687 (2017).

16. Li, L., Lin, Q., Tang, M., Duncan, A. J. E. & Ke, C. Advanced Polymer Designs for Direct-Ink-Write 3D Printing. *Chem. – Eur. J.* **25**, 10768–10781 (2019).

17. Ko, S. H., Chung, J., Hotz, N., Nam, K. H. & Grigoropoulos, C. P. Metal nanoparticle direct inkjet printing for low-temperature 3D micro metal structure fabrication. *J. Micromechanics Microengineering* **20**, 125010 (2010).

18. Eloi, J.-C., Chabanne, L., Whittell, G. R. & Manners, I. Metallopolymers with emerging applications. *Mater. Today* **11**, 28–36 (2008).

19. Bakhishev, T. & Subramanian, V. Investigation of Gold Nanoparticle Inks for Low-Temperature Lead-Free Packaging Technology. *J. Electron. Mater.* **38**, 2720–2725 (2009).

20. Barngrover, B. M. & Aikens, C. M. Electron and Hydride Addition to Gold(I) Thiolate Oligomers: Implications for Gold–Thiolate Nanoparticle Growth Mechanisms. *J. Phys. Chem. Lett.* **2**, 990–994 (2011).

21. Nasaruddin, R. R., Chen, T., Yan, N. & Xie, J. Roles of thiolate ligands in the synthesis, properties and catalytic application of gold nanoclusters. *Coord. Chem. Rev.* **368**, 60–79 (2018).

CHAPTER 5: INVESTIGATION OF THE ANTIMICROBIAL PROPERTIES OF A NOVEL SILVER METALLOGEL*

5.1 Synopsis

Similar to Chapter 4, the project discussed here is a study for the future application of the metallogel assembly discussed in length in Chapter 3. Chapter 3 discusses the structure of a rigid silver-cysteine metallogel. Silver containing nanomaterials are of interest for many biological applications, specifically antimicrobial applications, due to the studied antimicrobial properties of silver ions. Presented herein is the investigation of the antimicrobial properties for the silver-cysteine metallogel discussed in Chapter 3.

The rise of antimicrobial resistance necessitates the need for more compounds and antimicrobial materials. To that end, silver nanomaterials have a rich history of antimicrobial application and are promising candidates for next-generation antimicrobials. Previously, a coinage-metal thiolate metallogel system has been discussed. This metallogel system presents a new supramolecular material, including silver-ion based systems, provoking interest for future antimicrobial applications. Herein, antimicrobial properties of a novel silver-cysteine metallogel described in previous chapters is examined.

5.2 Introduction

Healthcare-associated infections (HAIs) represent a class of bacterial infections affecting patients who are already receiving care for other health-related concerns.[1] HAIs result in

* *The work presented herein represents unpublished work. James Armstrong's contributions include experimental design, data analysis, and synthetic development representing all work presented here aside from the mammalian cell study.*

approximately 90,000 deaths and costs $28-45 billion per year to hospitals in the USA.[1] As such, the Center for Disease Control considers limiting HAIs a top priority.[2] More effective clinical practices and procedures, as well as new antibacterial agents are needed to address these issues. One particular area of research looking to combat these issues is through silver based

antibacterial materials.[3,4] Silver is already known for its antibacterial properties and has been

Used throughout history, although interest was lost with the invention of modern antibiotics.[4,5] Silver nanomaterials are now regaining scientific and commercial interest as a mechanism to fight against antibacterial-resistant microbes. Indeed, Multiple silver-based products are already commercially available for antimicrobial applications.[6,7]

Silver based antimicrobial technologies are among the most commonly used antimicrobial agents in the healthcare sector. A large amount of research is funded for developing soft materials for antimicrobial applications, commonly silver-based gel materials.[8,9] Silver nanomaterials' properties can be manipulated by changing the size, shape, and ligand associated with silver nanoparticles or ions. The flexibility has led to studies into silver nanoparticle-based antimicrobials, as well as silver-ion based supramolecular antimicrobial materials. While some current reports of silver nanoparticle systems appear promising for this application, questions remain about the toxicity of silver nanoparticles, such as the aggregation of non-toxic particles, leading to toxicity over time.[10] Silver-ion based soft materials are being explored as a potential solution to this problem.

Supramolecular materials have recently gained interest as antimicrobial agents due their tunable properties.[8] Supramolecular materials used in antimicrobial applications are typically formulated with silver, largely in part due to the extensive body of research elucidating silver's bio-active properties. Most of these materials in general will have silver loaded in nanoparticle

forms; for example, hydrogel bandages or pastes are typically loaded with silver nanoparticles to form a composite antimicrobial product. However, silver nanoparticles are disadvantageous due to their toxicity.[10] One might suspect that silver ions would be a more suitable substrate, but on the other hand, silver ions can be deactivated by chlorine ions which are ubiquitous in biological contexts.[11] As such, a system that could make use of silver ions while preventing their inhibition would have profound implications in next-generation healthcare.

We recently reported the advent of a novel silver cysteine metallogel system, which is discussed in Chapters 3 and 4. The material is unique due to its amorphous nature and hygroscopic properties; it is soluble in water and can reform into a metallogel when dehydrated. This reversible gelation process is a defining characteristic to the metallogel. The metallogel system provides unique architecture that could provide improved capabilities over competing silver-based antimicrobials. Here, silver ions are incorporated into the metallogel structure. This could lead to a longer lifetime of antimicrobial activity, resulting in an antimicrobial material that needs to be applied less often.

It is hypothesized that the metallogel could overcome some of the inherent limitations associated with silver-based materials that depend on toxic nanoparticles. As additional design assets, the metallogel is free of hazardous solvents, is water soluble, and can applied as a solid or liquid. Thus, the metallogel's implicit versatility in conjunction with its antimicrobial properties should provoke interest for developing next-generation healthcare products.

In Chapter 3 a silver-cysteine metallogel synthesized through the use of glyme as an antisolvent was explored in depth. Chapter 4 utilized similarly synthesized metallogels to explore their application for the additive manufacturing of metal foams. This project explores a different application for glyme synthesized metallogels, looking at the antimicrobial properties of a silver-

cysteine system. Presented here are some initial results quantifying the antibacterial properties of the silver-cysteine metallogel. The minimum inhibition concentration (MIC) of the metallogel towards *E. coli*, toxicity towards mammalian cells, and initial progresses towards long-term metallogel surface treatment are explored.

5.3 Results and Discussion

The initial objective was to measure the antimicrobial properties for a silver-cysteine based metallogel. Previous characterization had described versatility with respect to both ligands and metals used in metallogel formulation. Silver-cysteine was tested as the first ligand-metal pair primarily due to the hypothesis that its silver ions would display antibacterial activity, but also because it has been our most studied metallogel to date. To probe antibacterial activity, the MIC was measured against *E. coli*. This was compared to cultured mammalian cells in an effort to roughly assess compatibility with higher functioning organisms (e.g., hospital patients).

The metallogel effects on *E. coli* are investigated with a study of the MIC. The MIC of a material is the lowest concentration in which bacterial growth is prevented. One method of testing the MIC of an antimicrobial material is broth dilution, where increasing concentrations of an antimicrobial is added to liquid or solid cultures of the bacteria in question.[12] An example is shown in Figure 5.1 below, where the concentration of the silver-cysteine metallogel is increased as samples move from left to right. Cultures of *E. coli* in LB media are incubated in the presence of the metallogel.

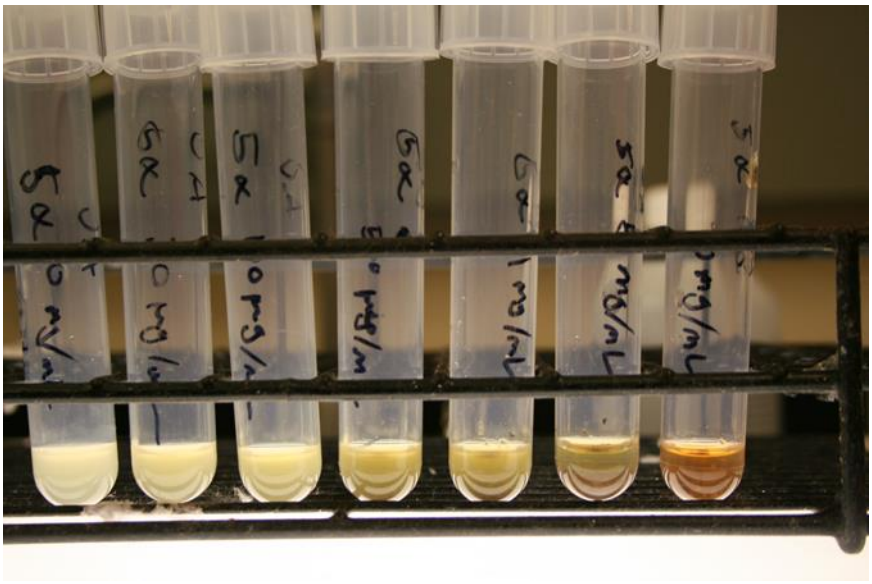

Figure 5.1: Broth dilution testing of the minimum inhibitory concentration of a silver-cysteine metallogel with respect to *E. coli*. Metallogel concentration increases from left to right. Higher concentration of metallogel results in precipitation, thought to be due to metallogel-cell media interactions.

Unfortunately, the Ag-Cys metallogel induces a color change at high concentrations. This prevents the ability observe the lack of bacterial growth in the culture, either by eye or by using an optical density measurement at 600nm to determine culture growth. This highlights an issue seen further, where the silver- cysteine metallogel interacts with cell media.

To work around this difficulty, serial dilution was used to determine the concentration at which bacterial growth was inhibited. This uses a similar process as the broth dilution above, however, cultures were plated from each trial, to allow for colony counting to find the MIC. Samples would be incubated overnight, similar to the broth dilution method above. After 24 hours, the culture is then plated on an agar plate to measure the bacteria levels to compare to initial concentrations. A series of dilutions are plated in triplicate on the agar plate and allowed to grow overnight. This method yielded an MIC value of 6.5 mg/mL for an Ag-Cys metallogel towards *E. coli*.

This is a relatively high MIC value compared to other silver nanomaterials towards *E. coli*. For example, silver ions have an MIC of 1-10µg/mL towards *E. coli*.[13] One potential explanation for this is the use of a thiolate ligand. Previous studies have shown the presence of thiols to decrease the antimicrobial activity of silver towards bacteria.[14] This is thought to be due to the strength of the silver-thiol bond, making silver inactive to react in solution.

Disk diffusion testing was utilized to study the ligands' effect on the antimicrobial activity. Disk diffusion test is a method of antimicrobial testing where the material in question is loaded onto a paper disk and diffuses out into an agar lawn of bacteria. The resultant ring where bacteria doesn't grow is called the zone of inhibition and is proportional to the MIC/ antimicrobial activity of the material.

A disk diffusion test was run to compare the efficacy of a silver-cysteine metallogel compared to a silver nitrate solution. The goal of this study was to compare the metallogel to unprotected silver ions in solution. A paper disk was saturated with a solution, allowed to dry, then placed on an agar plate with an even distribution of *E. coli*. The plates were then incubated at 37 °C for 24 h. The materials on the disk will diffuse out from the disk, creating a zone of inhibition where bacteria will not grow. The samples shown in Figure 5.2 below, clockwise from the top, 10, 20, 30, 40 mg/mL. The metallogel exhibits a larger zone of inhibition than the unprotected silver ions. This is thought to be due to silver ion deactivation through the formation of insoluble products. Silver ions are easily precipitated by chlorine ions, resulting in a deactivated product, whereas the metallogel protects silver from being deactivated and results in a much larger zone of inhibition. The silver cystine metallogel can diffuse further, as silver is bound to cysteine and is not free to react with chlorine. A silver cysteine hydrogel synthesized without glyme as an anti-

solvent does not exhibit a zone of inhibition at any concentration. This control was run to show the metallogel formation is unique and necessary for this behavior.

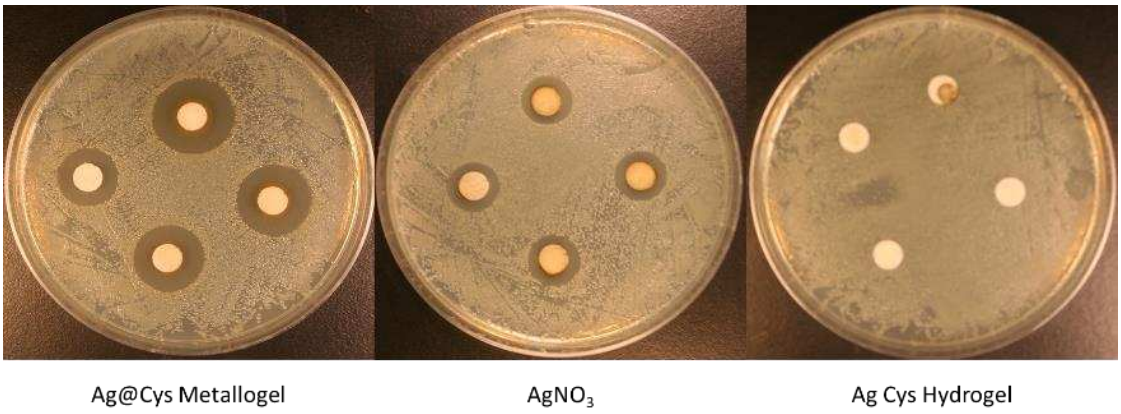

Figure 5.2: Disk diffusion study comparing silver ions to the silver cysteine metallogel.

This study likely shows increased diffusion of the silver metallogel when compared to silver ions and a silver cysteine hydrogel. Silver ions react rapidly with chloride ions to form AgCl, an insoluble precipitate, which has vastly lower antimicrobial properties when compared with silver ions.

The previous test showed that silver ions supplied by the metallogel are resistant to deactivation. This resistance indicated the metallogel could be utilized well as a topical application with a slow-release action of silver. As such, use of the metallogel as a surface coating was investigated. To do this, Kimwipes saturated with [aqueous] metallogel were applied to glass slides as a thin coating, simulating commercially available antimicrobial wipes. *E. coli* was added to the metallogel slide as well as a control slide which did not have any coating. The slides were incubated for 24 hours after which growth was assessed, Figure 5.3 and Table S6. In summary, the control slides showed bacteria growth, while the metallogel slides did not. Slides coated with metallogels were left to sit up to a month without showing any evidence of bacterial growth.

Shown here is that the metallogel can be applied to a surface and prevent *E. coli* growth up to 4 weeks later. There was no sign of *E. coli* growth at any step in the study. The next initial aim was to investigate how the metallogel interacts with mammalian cells to compare to the effect towards bacterial cells. If a product is to be formed with this metallogel formulation, non-toxicity towards mammalian cells is an important step.

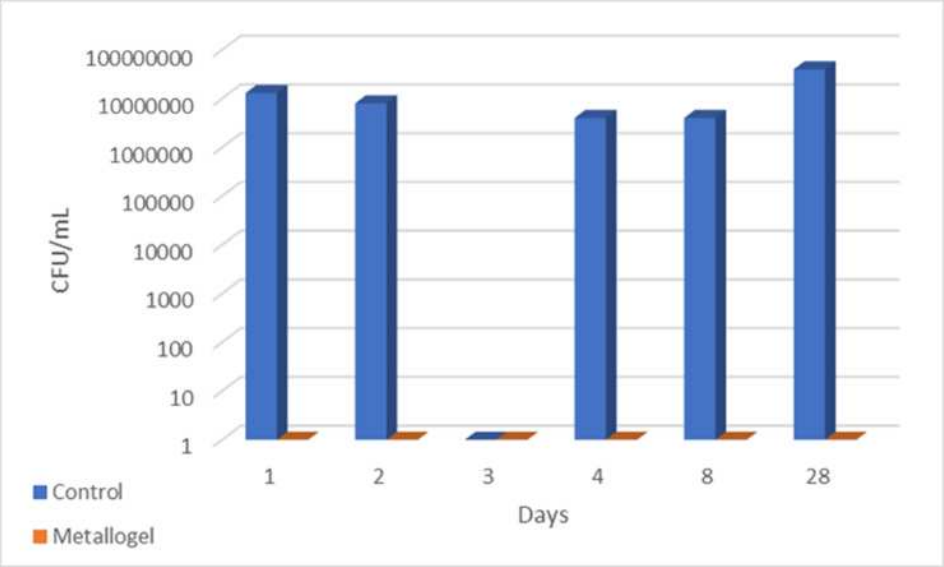

Figure 5.3: *E. coli* growth on glass slides coated with silver-cysteine metallogel compared to bare glass slides.

Herein we are looking for the effective concentration, EC_{50}, of the analyte towards the mammalian cells. This is the concentration where half of the expected concentration is seen. In other words, it is the concentration of metallogel added which results in half the response of a similar trial with no metallogel present. HeLa cells are grown over 24 hours in a 96-well plate, with samples of increasing concentrations of the metallogel spiked into the cell media, Figure 5.4.

This study was also affected by metallogel compatibility with cell media. Precipitates were visibly observed in the wells after incubating with the metallogel. The precipitate was unable to be easily washed away with PBS buffer. As a workaround, wells of cell media with similar concentrations of metallogel were run alongside the cell culture samples, set ups is shown in Table S7. The signal response for the optical density measurement of the media + metallogel was subtracted from the corresponding sample.

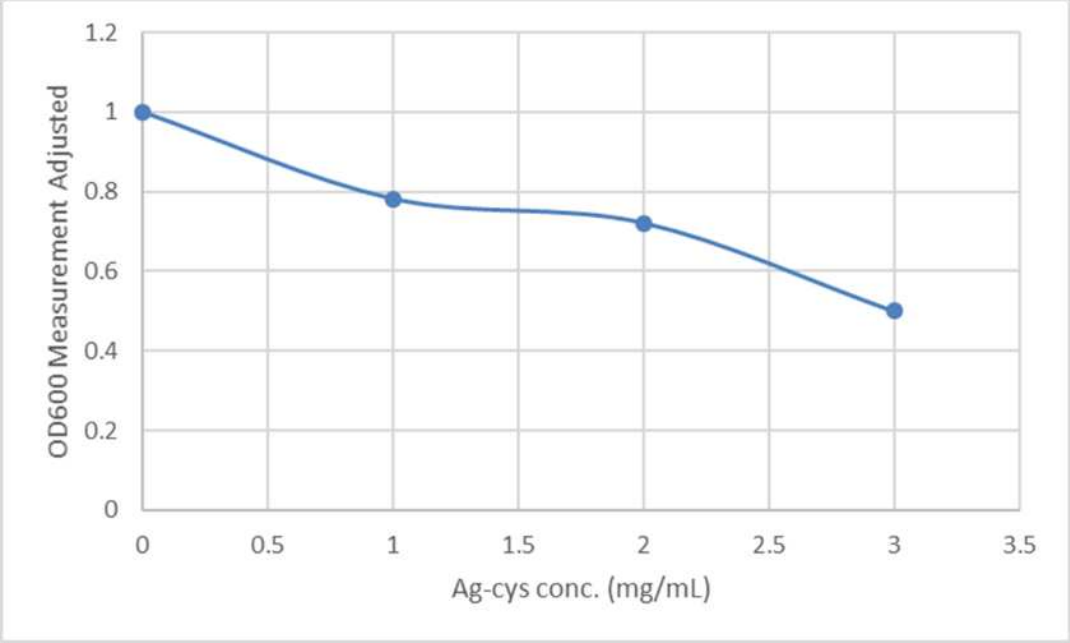

Figure 5.4: Study of silver cysteine metallogel effect on HeLa cell growth.

The results are shown above in Figure 5.4. This result indicates an EC_{50} around 3mg/mL. This is unfortunate, as this number is below the MIC of the metallogel towards *E. coli*.

Although the EC_{50} is lower towards mammalian cells than the MIC is towards *E. coli,* there are many studies that need to be done to explore the efficacy of the metallogel as an antimicrobial material. The use of HeLa cells could be a factor, as cancer cells may have a different response than non-cancerous mammalian cells. The study also measured the growth of HeLa cells over a

24-hour period. This does not necessarily mean the metallogel is killing the cells, it could be inhibiting growth. In future studies, a live/dead stain to measure the toxicity of the metallogel towards mammalian cells is needed. Development of further tests or assays which facilitate direct measurement of metallogel interactions with mammalian cells without cell media present could also be an avenue of future research, such as mouse studies.

The studies are also affected by the reaction of cell media and the metallogel. This isn't unexpected, as in the past cell media has been seen to play a role in the efficacy of antimicrobial silver materials.[15] This could potentially be resolved by finding a formulation which is more compatible with cell media, potentially through the use of a different ligand.

Potential applications for glyme-synthesized metallogels range widely from additive manufacturing, discussed in Chapter 4, to antimicrobial applications as discussed here. The scope of these initial results was impacted by the shutdown from Covid-19. A larger project envisioned utilizing other metallogel formulations, i.e. different metals and ligands, to compare these formulations and discover promising formulations for antimicrobial applications. The silver metallogel appears to have a longer lifetime of antimicrobial activity, at the cost of some efficacy, requiring a higher concentration than silver ions to inhibit bacterial growth. This does make the metallogel interesting for potential surface coating applications. For this reason, future work comparing glyme-synthesized metallogel efficacy towards biofilms would be of scientific interest. The lower efficacy of the metallogel could also open applications where the metallogel is applied in lower concentrations than would impact a system. For example, small molecule drugs could potentially be utilized instead of organic ligands for creation of metallogels. As the state of the metallogel is water content dependent, this opens the pathway for using the glyme-metallogel synthesis to create products which will slowly release the drug. For the antimicrobial application,

the slow release of silver ions was presented as an opportunity. Controlled drug release metallogel formulations would be similar in scope, however, they would be dependent on the slow release of the ligand, or drug, instead of the metal ion.

5.4 Conclusion

Presented here is an initial investigation into the antimicrobial properties of a novel silver metallogel. A silver-cysteine metallogel was analyzed. The material appears to be unstable in various cell media. This has made accurate measurements of the metallogel interaction with mammalian cells an ongoing difficulty. The material also appears to have a long lifetime when used as a surface treatment. This is a promising result that warrants further studies. Future work envisions metallogel formulation designs with higher compatibility with cell media, as well as more in-depth studies on the toxicity of the metallogel towards mammalian cells.

5.5 Experimental

Materials

1,2-dimethyoxyethane (anhydrous, 99.5%, inhibitor-free), DL-cysteine (technical grade), silver nitrate (ACS reagent, ≥99.0%), sodium hydroxide (certified ACS pellets), Penicillin-Streptomycin were sourced from Sigma-Aldrich. Water used was nanopure water. CellTiter 96 Aqueous One Cell Proliferation Assay was sourced from Promega. Gibco Dulbecco's Modified Eagle Medium (DMEM) was sourced from Thermo Fisher. Escherichia coli (Migula) Castellani and Chalmers (ATCC 25922) was sourced from ATCC.

Silver-Cysteine Metallogel Synthesis

A scintillation vial is charged with 3mL of 100mM AgNO3(H2O) and a stir bar on a stir plate. The stir plate is set to a medium rate, and 9mL of 100mM Cysteine (0.3MnaOH), followed immediately by 18mL of 1,2-dimethoxyethane. This is allowed to stir for 20 minutes before transfer to a centrifuge tube. The reaction is spun at 5000rpm for 10 minutes, resulting in precipitation of the gel phase, with a clear, colorless supernatant. The supernatant is decanted, and the gel is collected with a pipette. The gel is lyophilized into a powder, to allow for an accurate mass measurement.

Broth dilution

Ag-Cys metallogel material is dissolved in LB in a 50mg/mL solution. This solution is diluted to the appropriate concentration using LB. *E. coli* cultures are seeded at an OD_{600} measurement of 0.01, or ~8*10^6 CFU/mL. The cultures are incubated overnight at 37 degrees C for 24 hours.

MIC testing, Serial Dilution

Testing the MIC from the broth dilutions is done using serial dilution. The initial concentration is known, in CFU/mL. After 24h of growth, cultures are serial diluted and plated in triplicate on LB agar plates in 10 microL samples. These plates are then grown at 37 degrees C overnight. The dilution where the colonies present can accurately be counted is counted, averaged and a concentration is back calculated.

Disk Diffusion

Disks were prepared by punching 8mm disks out of filter paper. These disks were then saturated with 10µL of metallogel at various concentrations in water. The disks were allowed to dry before use.

Plates were prepared by evenly spreading 100 µL of *E. coli* on an LB agar plate. The disks were then pressed onto the plate, which was incubated overnight at 37°C.

EC_{50} Study

Hela cells were passaged in DMEM with 10% Foetal Bovine Serum and 100 Units/mL Penicillin. Cells trypsinized in the 3rd passage were plated to 5000 cell/well density in 200 uL media to adhere overnight. Media was aspirated off and 200µL of filtered media containing a variable amount of metallogel was added to each well. These cells were incubated for 24 hours. Media was aspirated off and 200µL media containing containing 20µL CellTiter Aqueous one Proliferation Assay dye was added to each well. Absorbance at 490nm was measured for each sample after 1 hour.

Surface treatment studies

As-synthesized silver-cysteine metallogel was thinly coated on a glass slide, using a chemwipe saturated with the metallogel. This was done to simulate an antimicrobial wipe using this material. A sample of *E. coli* was added to the metallogel slide, as well as a control slide which didn't have any coating. The slides were incubated for 24 hours to see if bacteria would grow.

REFERENCES

1. Haque, M., Sartelli, M., McKimm, J. & Abu Bakar, M. Health care-associated infections – an overview. *Infect. Drug Resist.* **11**, 2321–2333 (2018).

2. Antibiotic resistance threats in the United States, 2013. (2013).

3. Doudi, M., Naghsh, N. & Setorki, M. Comparison of the effects of silver nanoparticles on pathogenic bacteria resistant to beta-lactam antibiotics (ESBLs) as a prokaryote model and Wistar rats as a eukaryote model. *Med. Sci. Monit. Basic Res.* **19**, 103–110 (2013).

4. Rai, M. K., Deshmukh, S. D., Ingle, A. P. & Gade, A. K. Silver nanoparticles: the powerful nanoweapon against multidrug-resistant bacteria: Activity of silver nanoparticles against MDR bacteria. *J. Appl. Microbiol.* **112**, 841–852 (2012).

5. Barras, F., Aussel, L. & Ezraty, B. Silver and Antibiotic, New Facts to an Old Story. *Antibiotics* **7**, (2018).

6. Sim, W., Barnard, R., Blaskovich, M. A. T. & Ziora, Z. Antimicrobial Silver in Medicinal and Consumer Applications: A Patent Review of the Past Decade (2007–2017). *Antibiotics* **7**, 93 (2018).

7. Liu, Y. *et al.* Silver(i)–glutathione biocoordination polymer hydrogel: effective antibacterial activity and improved cytocompatibility. *J. Mater. Chem.* **21**, 19214 (2011).

8. Yang, K. *et al.* Antimicrobial hydrogels: promising materials for medical application. *Int. J. Nanomedicine* **13**, 2217–2263 (2018).

9. Boonkaew, B., Kempf, M., Kimble, R., Supaphol, P. & Cuttle, L. Antimicrobial efficacy of a novel silver hydrogel dressing compared to two common silver burn wound dressings: Acticoat^{TM} and PolyMem Silver®. *Burns* **40**, 89–96 (2014).

10. Vazquez-Muñoz, R. *et al.* Toxicity of silver nanoparticles in biological systems: Does the complexity of biological systems matter? *Toxicol. Lett.* **276**, 11–20 (2017).

11. De Leersnyder, I., De Gelder, L., Van Driessche, I. & Vermeir, P. Influence of growth media components on the antibacterial effect of silver ions on Bacillus subtilis in a liquid growth medium. *Sci. Rep.* **8**, 9325 (2018).

12. Wiegand, I., Hilpert, K. & Hancock, R. E. W. Agar and broth dilution methods to determine the minimal inhibitory concentration (MIC) of antimicrobial substances. *Nat. Protoc.* **3**, 163–175 (2008).

13. Schierholz, J. M., Wachol-Drewek, Z., Lucas, L. J. & Pulverer, G. Activity of silver ions in different media. *Zentralblatt Für Bakteriol.* **287**, 411–420 (1998).

14. Mulley, G., Jenkins, A. T. A. & Waterfield, N. R. Inactivation of the Antibacterial and Cytotoxic Properties of Silver Ions by Biologically Relevant Compounds. *PLoS ONE* **9**, e94409 (2014).

15. Souter, P., Cunningham, J. C., Horner, A. & Genever, P. G. The variable toxicity of silver ions in cell culture media. *Toxicol. In Vitro* **60**, 154–159 (2019).

APPENDIX A: SUPPLEMENTAL FIGURES

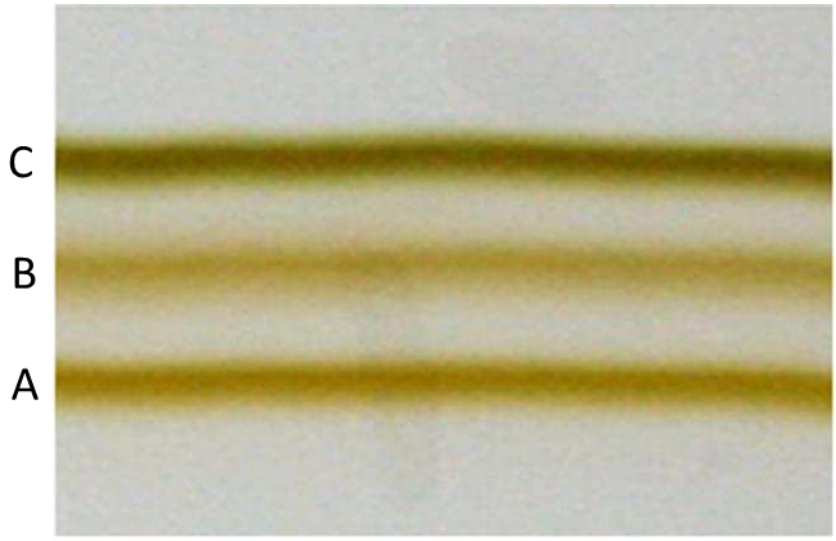

Figure S1: TBE-PAGE separation of synthetic products A, B, and C. A has been identified as $Au_{25}(pMBA)_{17}diglyme_1$ and is the focus of this work, B and C are expected to be a larger cluster but has yet to be identified.

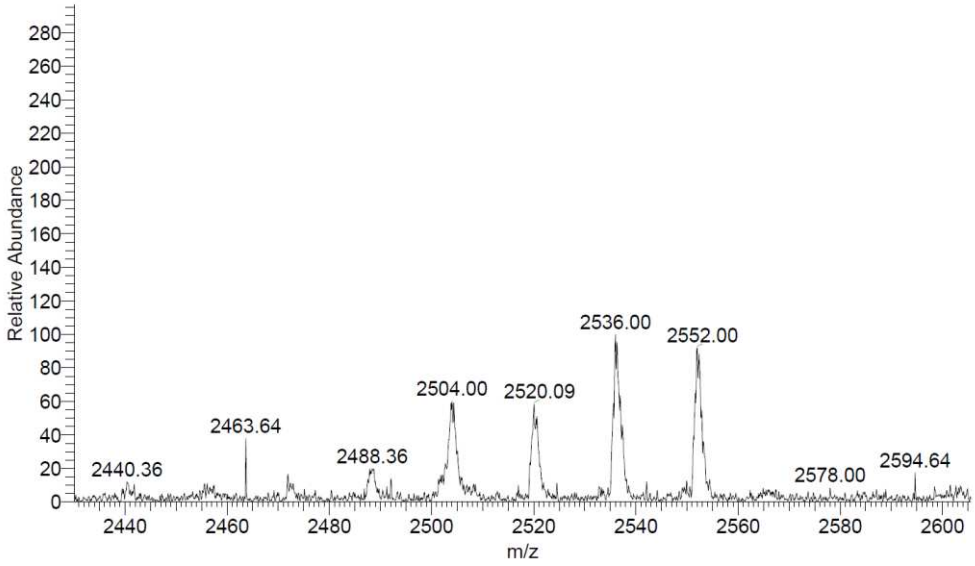

Figure S2: Ligand exchange with 3-mercaptopropionic acid as the incoming ligand. This was done at a 5000:1 ligand:cluster ratio, and pH of 6.

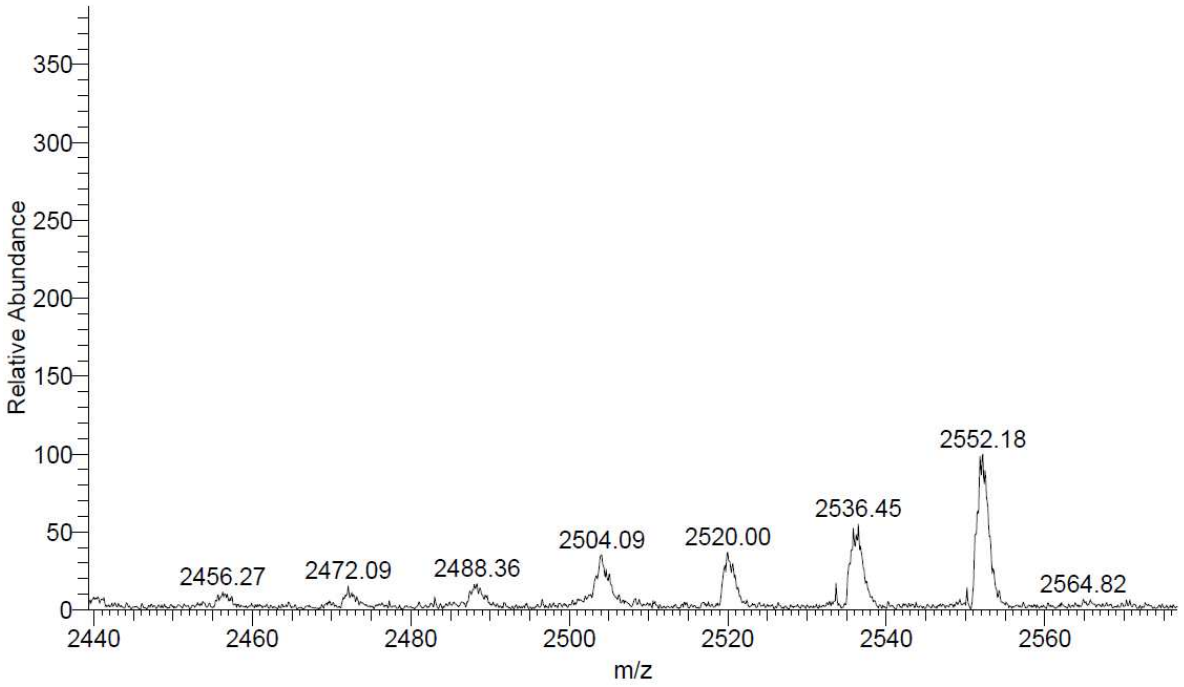

Figure S3: Ligand exchange with 3-mercaptopropionic acid as the incoming ligand. This was done at a 1000:1 ligand:cluster ratio, and pH of 6.

Table S1: Table of the observed nanocluster mass and potential assignments.

Atom Counts								
Au (196.97a.u.)	pMBA -H (153.182a.u.)	pMBA - 2H(152.182a.u.)	diglyme (134.17a.u.)	mass	mass/2	mass/3	mass/4	mass/5
25	18	0	0	7681.526	3840.763	2560.509	1920.382	1536.305
25	0	18	0	7663.382	3831.691	2554.461	1915.846	1532.676
25	17	0	1	7662.514	3831.257	2554.171	1915.629	1532.503
25	0	17	1	7645.378	3822.689	2548.459	1911.345	1529.076
25	9	8	1	7654.45	3827.225	2551.483	1913.613	1530.89
24	0	20	0	7770.76	3885.38	2590.253	1942.69	1554.152
23	16	0	0	6981.222	3490.611	2327.074	1745.306	1396.244
Observed Nanocluster						2551.843	1913.666	1530.749

\

Table S2: Saturated salt solutions used to generate relative humidities (RH%) and resulting equilibrium water content in the AMXs.

Sample	Salt	RH% (20 °C)	Equil. water wt%
A	**LiBr**	**6.61%**	**1.69%**
B	**LiCl**	**11.3%**	**2.80%**
C	**KOAc**	**23.1%**	**4.88%**
D	**$MgCl_2$**	**33.1%**	**7.37%**
E	**K_2CO_3**	**43.2%**	**14.9%**
F	**$Mg(NO_3)_2$**	**54.4%**	**20.2%**

Equation S1: Calculation for Young's Modulus from G'.

$$G' = \frac{E'}{2(1+\nu)}$$

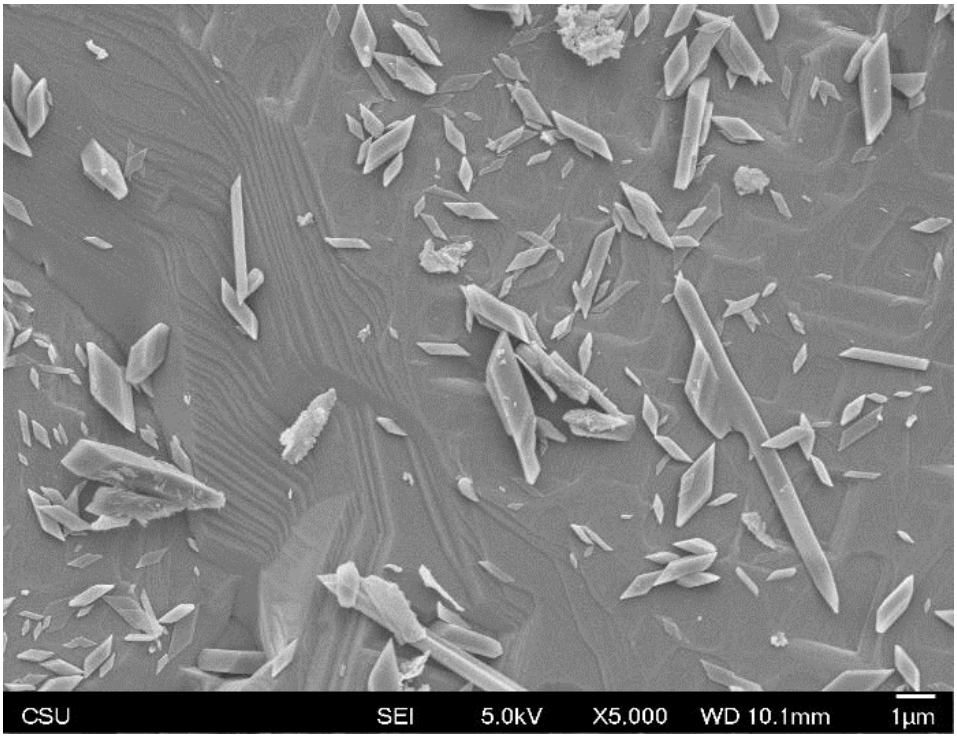

Figure S4: SEM micrograph showing microstructure of silver-cysteine hydrogel synthesized without glyme.

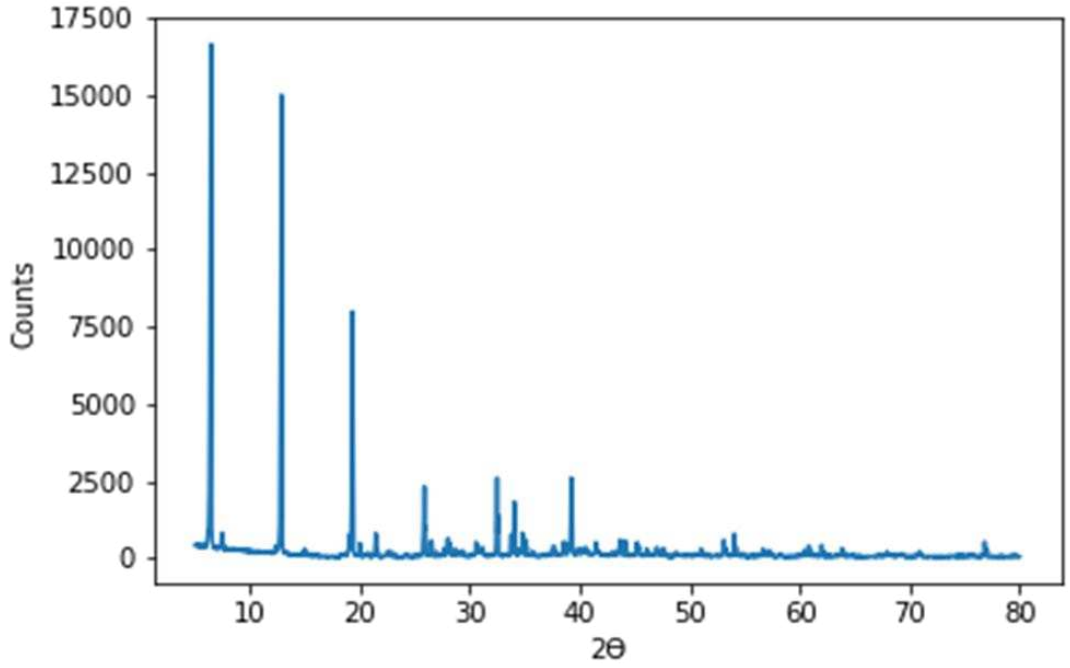

Figure S5: XRD of silver-cysteine hydrogel synthesized without glyme.

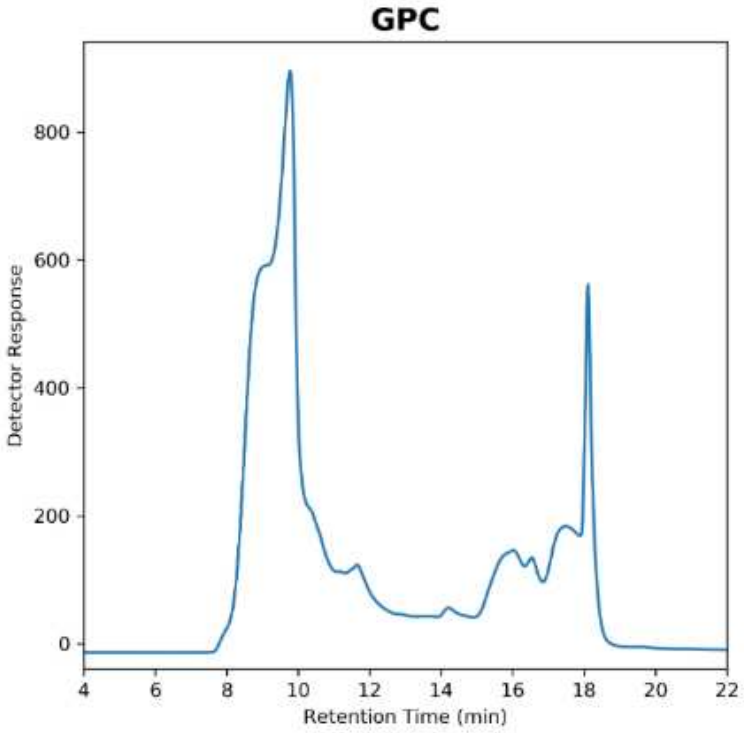

Figure S6: GPC-MALS chromatogram for silver-cysteine AMX.

Table S3: Fitted ^{13}C chemical shifts (δ_c) and peak widths (reported as full-width at half-maximum; fwhm) obtained by $^{13}C\{^1H$ CP/MAS NMR.

	δ_C (ppm)	**fwhm (ppm)**
Cysteine	**173.86**	**0.34**
	56.34	**0.43**
	28.44	**0.36**
Ag-Cys	**170.35**	**5.3**
	49.03	**5.96**
	26.24	**8.46**

Table S4: Binding energies (eV) for cations to functional groups of cysteine and DME, in singly and doubly bound configurations bridged by a metal center.

	Singly Bound					**Doubly Bound**			
Ion	**DME**	**COO**	**S**	**NH_2--S**	**NH_2--COO**	**COO-M-COO**	**COO-M-DME**	**S-M-S**	**S-M-DME**
Na+	**0.225**	**0.334**	**0.196**	**0.168**	**0.107**	**0.165**	**0.109**	**0.107**	**0.139**
Ag+	**0.609**	**0.923**	**1.514**	**1.231**	**0.449**	**0.827**	**0.487**	**1.296**	**0.482**

Table S5: ^{23}Na DOSY NMR for Na+ ions dissolved in water, and AMX material dissolved in water. The diffusion constants are very close, with the difference explainable by the increased viscosity of the AMX solution. This indicates Na ions in dissolved AMX are similar to free Na+ ions in solution.

Material	**Diff. Constants**	**RSS**	**SD**
NaCl	**8.608e-10 m2/s**	**3.924e-3**	**9.444e-3**
AMX	**6.309e-10 m2/s**	**7.801e-3**	**1.332e-2**

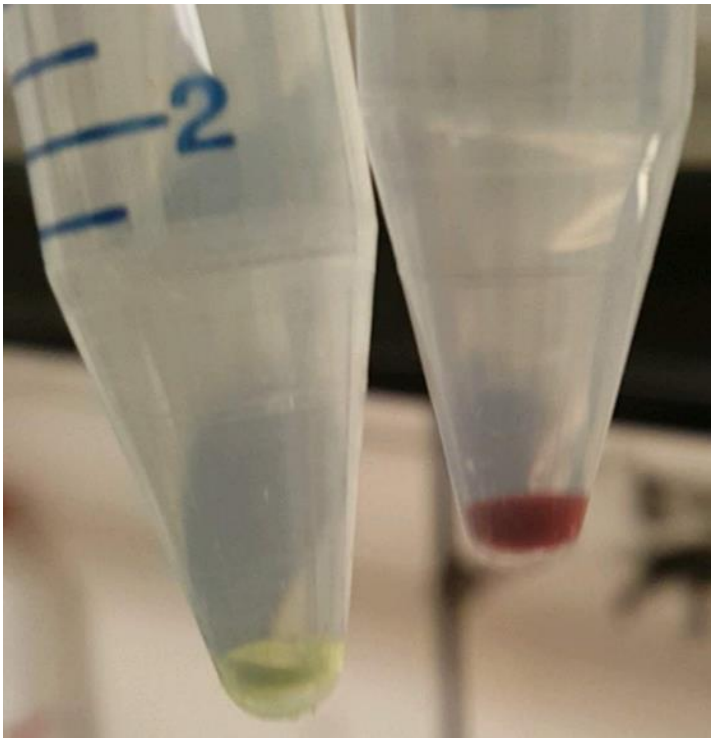

Figure S7: Metallogel synthesized with mercaptosuccinic acid (left) and glutamic acid (right).

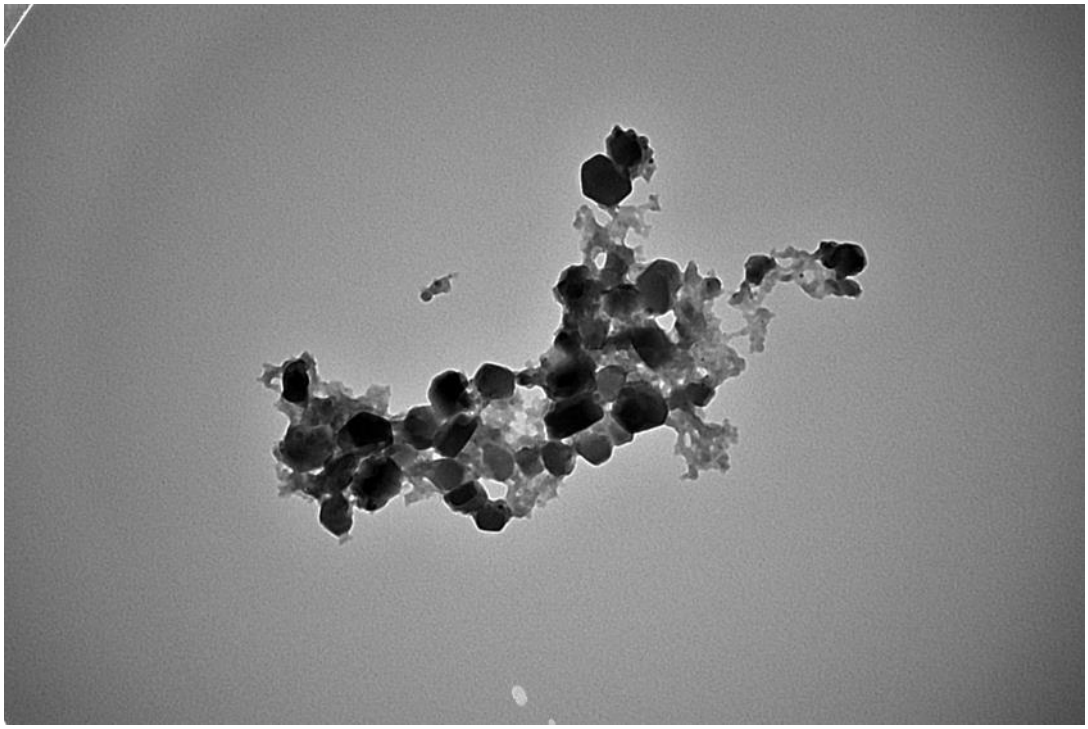

Figure S8: Crystallized silver-cysteine nanoparticles

Figure S9: Optical micrograph of sintered gold network

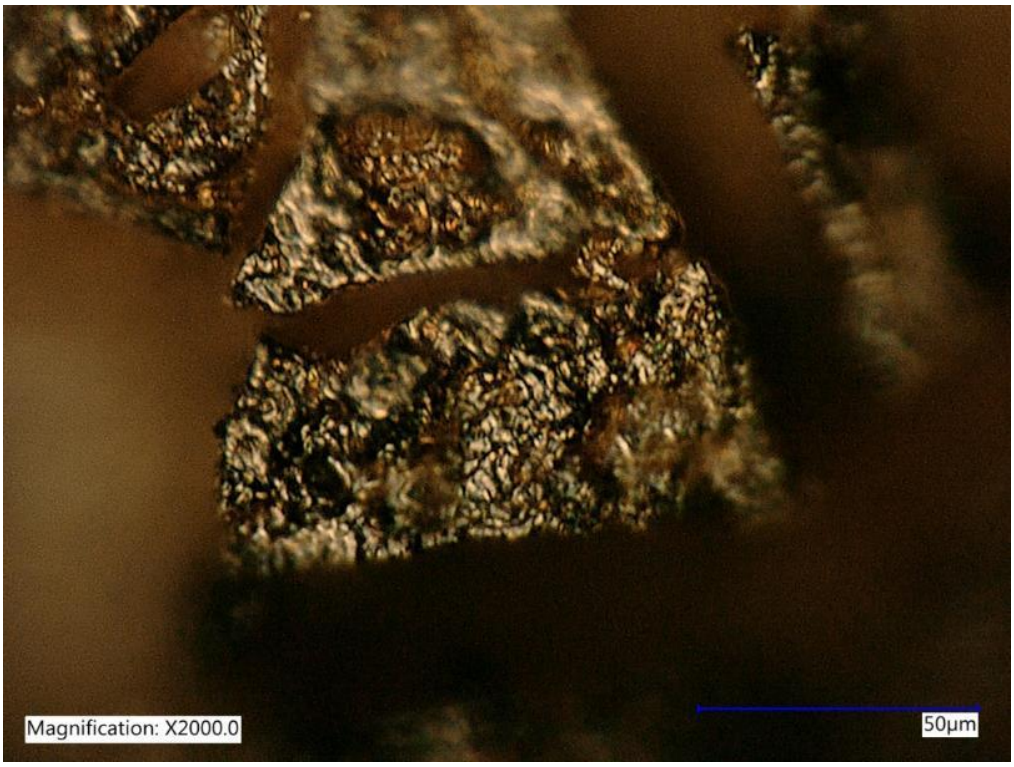

Figure S10: Optical micrograph of sintered gold network

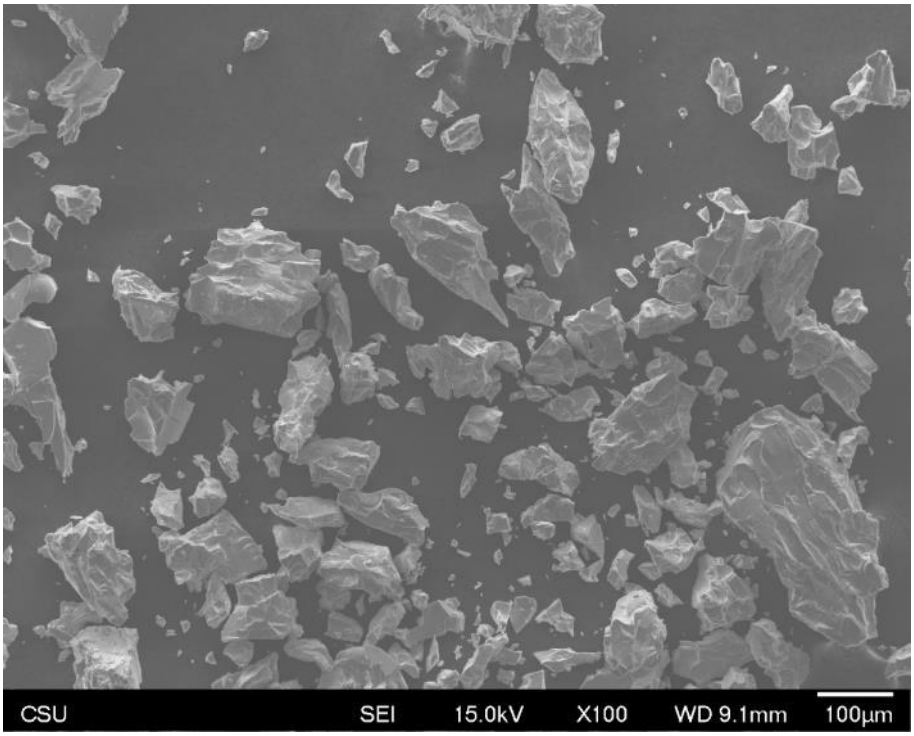

Figure S11: SEM micrograph of gold-thiomalate prior to sintering.

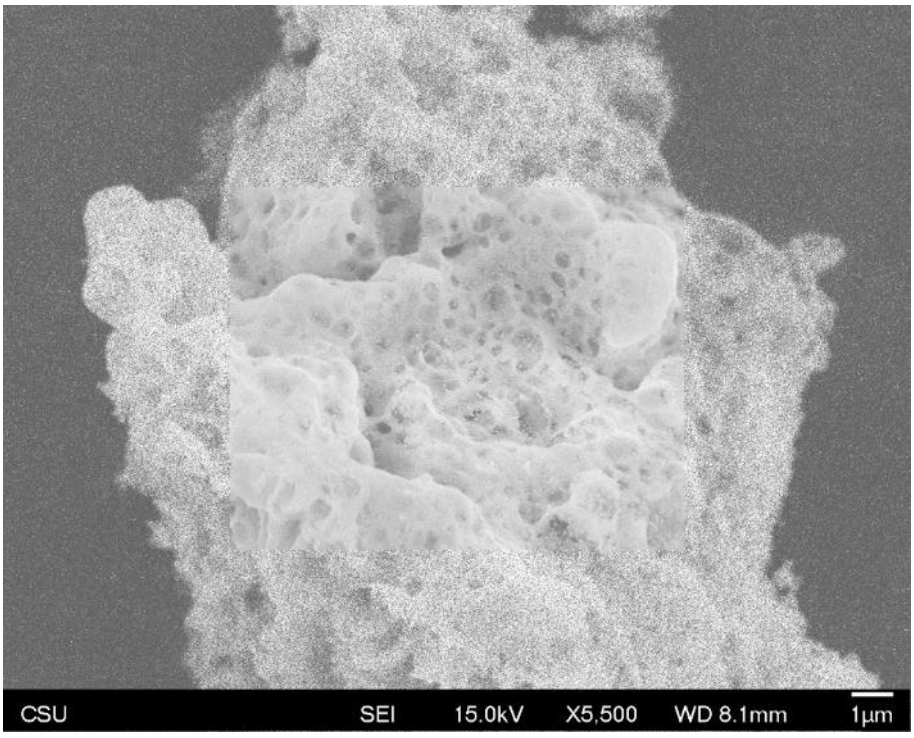

Figure S12: SEM micrograph of gold-thiomalate post-sintering.

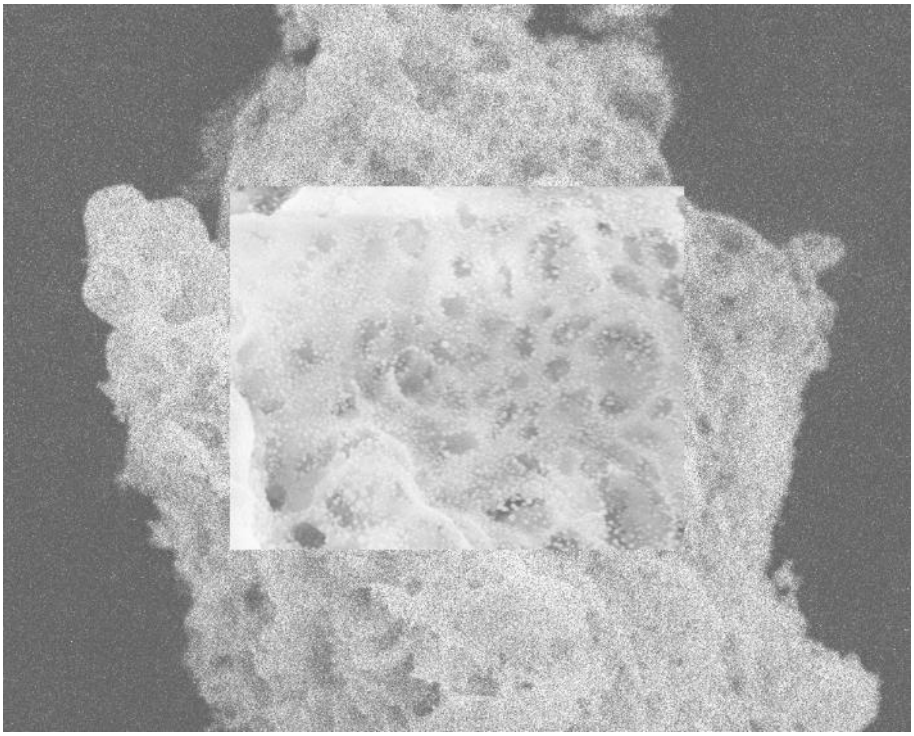

Figure S13: SEM micrograph of gold-thiomalate post-sintering.

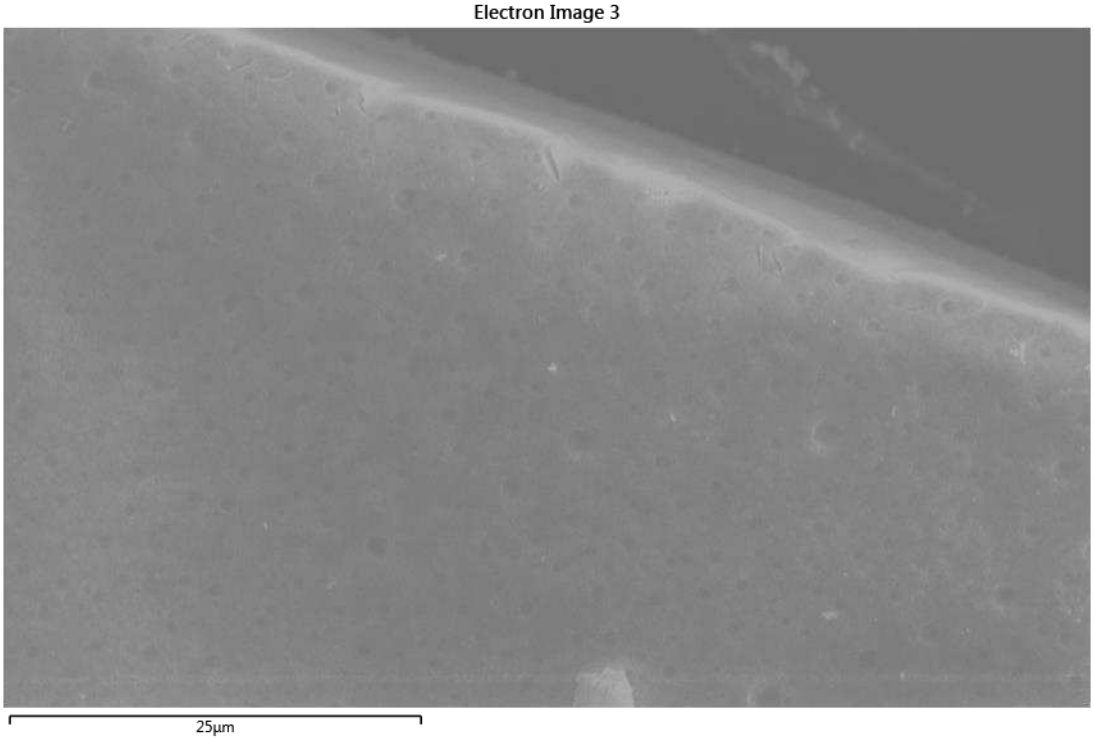

Figure S14: SEM micrograph of sintered gold foam

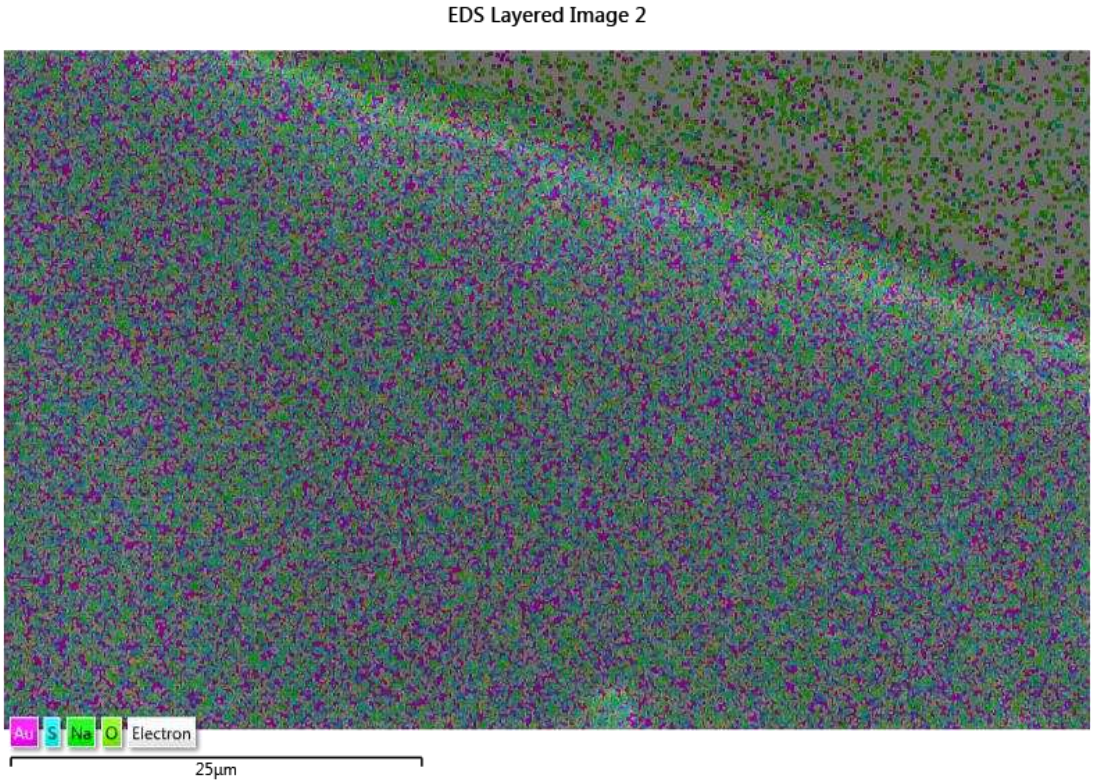

Figure S15: EDS layered image of elements in sintered gold foam

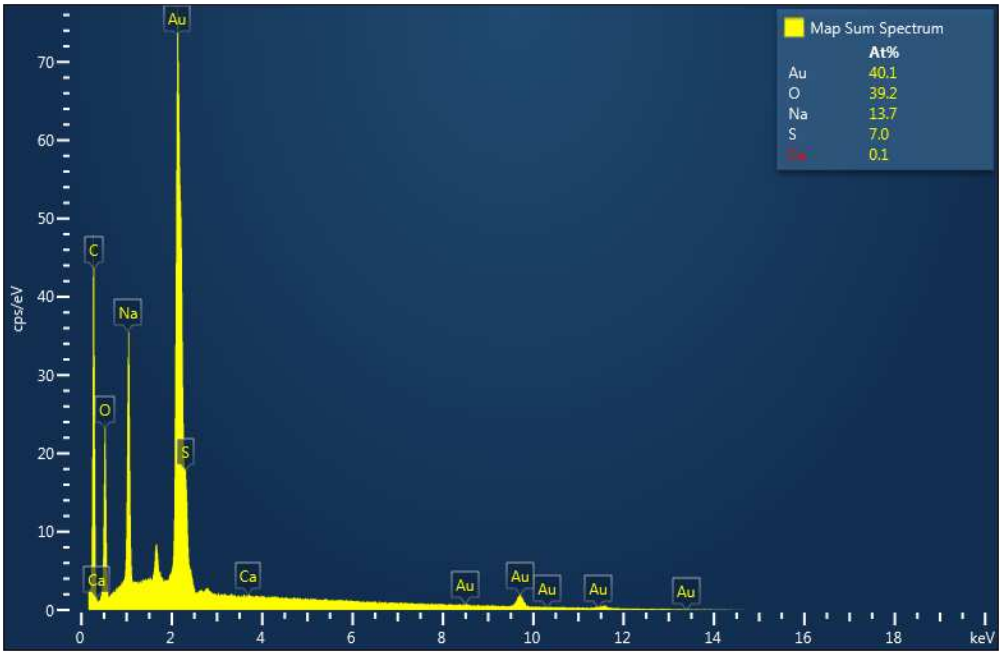

Figure S16: EDS spectrum of sintered gold foam.

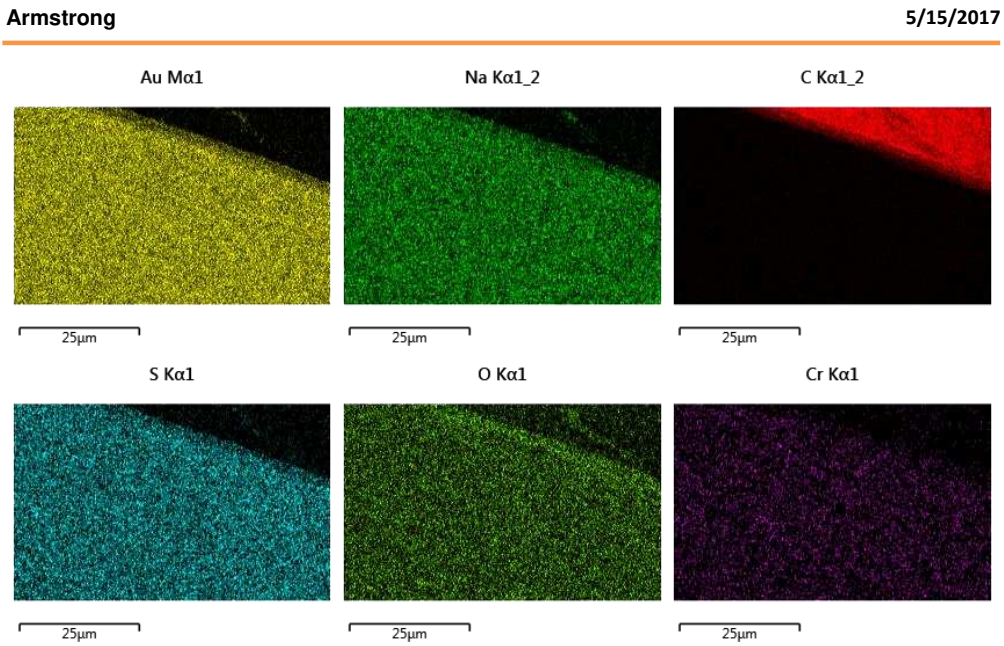

Figure S17: SEM micrographs overlayed with individual element mapping from EDS.

Table S6: Colony counts for surface treatment studies.

Day	CFU/mL(X*10^6)
1	13
2	8
3	0
4	4
8	4
28	40

Table S7: Absorption data for HeLa cell growth mixed with metallogels

	2	3	4	5	6	7	8	9	10
A									
B	0.174	1.218	1.289	1.285	1.268	0.454	0.423	0.631	10000 cells
C	0.176	1.33	1.364	1.516	1.16	0.509	0.581	0.624	10000 cells
D	0.178	1.477	1.464	1.326	1.24	0.448	0.389	0.591	10000 cells
E	0.18	0.848	0.914	0.762	0.792	0.665	0.571	0.595	5000 cells
F	0.159	0.867	0.882	0.769	0.8	0.434	0.588	0.614	5000 cells
G	0.188	0.95	0.944	0.869	0.855	0.495	0.542	0.653	5000 cells
H	Media +MTT	Cells +MTT	1mg/ml	2mg/ml	3g/ml	1mg/ml no cells	2mg/mL no cells	3mg/mL no cells	